NUCLEAR REACTION STUDIES OF STABLE AND UNSTABLE NUCLEI

A Thesis presented for the award of the degree of

2012

Doctor of Philosophy
in
Physics

RABINARAYAN PANDA
Regd. No: 01/2008/Physics Ph. D

School of Physics
Sambalpur University
Sambalpur, India

Guide: Dr. T. R. Routray
Professor
Sambalpur University

Co-Guide: Dr. S. K. Patra
Associate Professor
Institute of Physics

Dedicated To
My Family
And
My Teachers

Certificate

This is to certify that the thesis entitled "**NUCLEAR REACTION STUDIES OF STABLE AND UNSTABLE NUCLEI**" which is being submitted by **Rabinarayan Panda** for award of the degree of Doctor of Philosophy in Physics of Sambalpur University, Sambalpur is a record of his own research work carried out by him. He has carried out this investigations for the last six years on the subject matter of the thesis under our guidance at Sambalpur University, Sambalpur and Institute of Physics, Bhubaneswar. To the best of our knowledge, the matter embodied in the thesis has not been submitted for the award of any other degree by him or by anybody else.

5/11/2012

6/11/2012

Guide: Dr. T. R. Routray
Professor
Sambalpur University

Professor
P.G. Deptt. of Physics
Sambalpur University
Jyoti Vihar, Burla

Co-Guide: Dr. S. K. Patra
Associate Professor
Institute of Physics

Dr. S.K. Patra
Associate Professor
Institute of Physics
Bhubaneswar-751005

Declaration

I, Rabinarayan Panda declare that the thesis entitled **"NUCLEAR REACTION STUDIES OF STABLE AND UNSTABLE NUCLEI"** which is being submitted by me for award of the degree of Doctor of Philosophy in Physics of Sambalpur University, Sambalpur is a record of my own research work carried out by me. I have carried out these investigations for the last six years on the subject matter of the thesis under the guidance of Dr. T. R. Routray and Dr. S. K. Patra at Sambalpur University, Sambalpur and Institute of Physics, Bhubaneswar respectively. The matter embodied in the thesis has not been submitted to any other University/Institution for the award of any other degree.

Rabinarayan Panda

Rabinarayan Panda

Doctoral Scholar

Sambalpur University

Sambalpur

Acknowledgements

I express my deep sense of gratitude to Dr. S. K. Patra, Associate Professor, Institute of Physics, Bhubaneswar and Prof.(Dr.) T. R. Routray, School of physics, Sambalpur University, Sambalpur for introducing to the subject. Their continuous support, perceptive suggestions and invaluable guidance in due course of this work was very exciting and encouraging. Their accountability during the whole period has been a source of inspiration for me and will be in future. Every discussion during the past six years of this work have been very fruitful and has added a new chapter of knowledge.

I gratefully acknowledge the president of Siksha O. Anusandhan University for his encouragement during this work. I express my thanks to all the staff and HOD, Department of Physics, ITER, SOA University for providing me the support during the past three years in the Department. Special thanks to Prof. P. C. Dash and Mr. N. K. Sharma. I wish to express my thanks to all the staff and HOD, School of Physics, Sambalpur University. I deeply acknowledge the Director, Institute of Physics, Bhubaneswar, for providing me all the facilities of Library, Computation. Thanks to the staff of Library and computer section, Institute of Physics, for their co-operation. I express my thanks to M. Bhuyan, Ph.D Scholar, for his support during the completion of this work. I also wish to express my thanks to Prof. Raj. K. Gupta, Prof. L. Satapathy, Prof. C. R. Praharaj, Prof. B. Behera, Madam S. Subhasmita, Dr. P. Arumugam, Dr. B. B. Sahoo, Dr. M. S. Meheta, Dr. B. Singh, B. K. Sahu, S. Mahapatro, Mahesh, Subrat, Manoj, Ashis and all my friends.

Special thanks to my wife for her patience to endure the circumstances for the past three years that led to the completion of this thesis. I also like to take excuse from my little son Gugul for not giving him enough time during this period. I also express my deep sense of gratitude to my parents, uncle, aunt, Mamu, Mami, sisters and parents-in-law for their constant encouragement and support during the years.

List of Publications

I In Journals:

1. Isomeric States in ^{53}Co : A mean field analysis, S. K. Patra, F. H. Bhat, **R. N. Panda**, P. Arumugam, and Raj. K. Gupta, *Phys. Rev. C* **79**, 044303 (2009).

2. Nuclear reaction cross sections of exotic nuclei in the Glauber model for relativistic mean field densities, S. K. Patra, **R. N. Panda**, P. Arumugam, and Raj. K. Gupta, *Phys. Rev. C* **80**, 064602 (2009).

3. Elastic scattering of p+^{16}O at 300 MeV in relativistic Impulse approximation, M. Bhuyan, **R. N. Panda**, and S. K. Patra, *Orissa Journal of Physics*, Vol. **17**, pp. 1-17 (2010).

4. Formation of Neutron-Rich and Superheavy Elements in Astrophysical Objects, **R. N. Panda** and S. K. Patra, *J. Mod. Phys.*, Vol. **1**, 312 (2010).

5. Application of relativistic mean field and effective field theory densities to scattering observables for Ca isotopes, M. Bhuyan, **R. N. Panda**, T. R. Routray, and S. K. Patra, *Phy. Rev. C* **82**, 064602 (2010).

6. Structure effect on one neutron removal reaction using relativistic mean field densities in Glauber model, **R. N. Panda**, and S. K. Patra, *Int. J. Mod. Phys. E*, Vol. **20**, No. 12, 2505 (2011).

7. Multifragmentation Fission in Neutron-rich U and Th Isotopes, **R. N. Panda**, M. Bhuyan and S. K. Patra, *Nuclear Physics and Atomic Energy* (2012) accepted.

8. Energy Production from Neutron-rich Uranium and Thorium Isotopes, **R. N. Panda**, M. Bhuyan and S. K. Patra, *IEEE conference proceedings* (2012) accepted.

9. Nuclear Structure and Reaction Properties of Neon Isotopes with Relativistic Mean Field Densities, **R. N. Panda**, and S. K. Patra (communicated).

II In symposium and conferences:

1. Cross sections using exotic nuclei in Glauber Model for relativistic mean field densities , **R. N. Panda**, S. K. Patra, P. Arumugam, Raj K. Gupta, DAE Symp. on Nucl. Phys., Vol. 53, (2008) 327, IIT, Roorkee, India.

2. Isomeric states in ^{53}Co and ^{53}Fe: A mean field analysis, S. K. Patra, Raj K. Gupta, F. H. Bhat, and **R. N. Panda**, DAE Symp. on Nucl. Phys., Vol. 53 (2008) 237, IIT, Roorkee, India.

3. Nuclear Reaction Cross-sections for Neutron-rich Nuclei, **R. N. Panda**, and S. K. Patra, National Seminar on Research and Development (2008) 57, REC, Bhubaneswar, India.

4. One neutron removal reaction using relativistic mean field densities in Glauber model, **R. N. Panda** and S. K. Patra, DAE Int. Symp. on Nucl. Phys., Vol. 54 (2009) 258, BARC, Mumbai, India.

5. Formation of superheavy elements in astrophysical objects, **R. N. Panda**, and S.K. Patra, DAE Symp. on Nucl. Phys., Vol. 55 (2010) 434 , BITS, Pilani, Rajasthan, India.

6. The elastic scattering of $^{40,42,44,48}Ca$ at 1.0 GeV in the framework of relativistic impulse approximation, M. Bhuyan, **R. N. Panda**, T. R. Routray and S. K. Patra, DAE Symposium on Nucl. Phys. Vol. 55, (2010) 284, BITS, Pilani, Rajasthan, India.

7. Fission Energy from Neutron-rich Uranium and Thorium Isotopes, **R. N. Panda**, M. Bhuyan and S. K. Patra, DAE Symp. on Nucl. Phys., Vol. 56 (2011) 504 , Andhra University, Visakhapatnam, India.

8. Energy Production from Neutron-rich Uranium and Thorium Isotopes, **R. N. Panda**, M. Bhuyan and S. K. Patra, IEEE International conference on Engineering Education: Innovative Practices and Future Trends (AICERA 2012), Amal Jyothi College of Engineering, Kanjirappally, Kerala, India.

9. Reaction Cross sections of Ne Isotopes, **R. N. Panda**, B. K. Sahu and S. K. Patra, DAE Symp. on Nucl. Phys., Vol. 57 (2012), Delhi University, Delhi, India.

10. Total reaction cross section study for Ne, Mg, and Si isotopes with RMF densities, **R. N. Panda** and S. K. Patra, Indian Science Congress-2013, Calcutta University, Kolkata, India (accepted).

Table of Contents

Chapter 1

Introduction

Before the discovery of nucleus, Nuclear Physics or the structure of atomic nucleus was a mystery of nature. Many models of atom were proposed and among the significant was the Thomson's Plum Pudding model. In 1911, the epoch-making Rutherford α-particle experiment [1] was done which saw the dawn of Nuclear Physics, the discovery of Nucleus and the Rutherford's model of atom was proposed. In this way the Nuclear Physics got a shape, when the neutron was discovered in 1932 by Chadwick [2] and it gave the complete model of Nucleus. Soon after, several models and experiments were performed to know the mysterious nature of nuclear force and its propagation. The pioneering work of Yukawa [3] for the meson theory and soon after the nuclear shell models are some of the milestone in Nuclear Physics to study the nature of nuclear force. The Nuclear modeling and the reaction experiments are the methods to understand the nature of nuclear force. The Nuclear Structure Models and Nuclear Reaction Formalisms go neck to neck to explain it.

In nature about 300 nuclei are found. However, due to the present day relativistic ion beam (RIB) facility about 3000 nuclei are synthesized and another 5000 more nuclei are predicted to be synthesized by various mass models [4, 5, 6, 7]. Now, 118 elements have been identified, and placed in the periodic table. The naturally available nuclei are well studied, however, the artificial nuclei are short lived and their

properties are found to be extremely abnormal known as exotic nuclei whose position in the periodic chart is away from the valley of β-stability, which will be discussed in the subsequent sections. In the present thesis we will study the properties of such exotic nuclei using both the structure and reaction studies. Before going to the formulation we outline some of the important features of nuclear reaction and the study of nuclear structure by various models.

1.1 Nuclear reaction

When a particle strikes a nucleus, the resulting interaction is called as a "Nuclear Reaction". In this process atom's nucleus changes by gaining or releasing particles or energy. A nuclear reaction can release protons, electrons, as well as gamma rays. In nuclear reactions, a small change in mass results in a very large change in energy. Nuclear reactions and nuclear scattering are used to measure the properties of nuclei [8]. Reactions can exchange energy or nucleons and that can be used to measure the binding or excitation energies, quantum numbers of energy levels, and transition rates between levels. These reactions takes place when electrons, protons, alpha particles or heavy ions strike a target nucleus. Nuclear reactions can also be produced in nature by high velocity particles from cosmic rays. Beams of photons, mesons, muons and neutrinos can also produce nuclear reactions.

Nuclear reaction to occur, the nucleons in the incident particle, or projectile, must interact with the nucleons in the target. A high amount of energy is required to overcome the natural electromagnetic repulsion between the protons. This energy barrier is called as 'Coulomb barrier'. If a collision occurs between the projectile and a target nucleus, either the beam of particle scatter elastically leaving the target nucleus in its ground state or the target nucleus is internally excited and emit radiation or nucleons. A nuclear reaction is described by identifying the incident particle, target nucleus and reaction products. The incoming particle can produce different types

of reactions depending on its energy. In **scattering** reaction the outgoing particle identical with incident particle and the target nucleus doesn't break up. This may be elastic or inelastic scattering. In **elastic** case, the projectile and target remain in their ground state and the colliding particles only change direction of motion, possibly spin orientation. In **inelastic** case, the projectile and/or target are in an excited state after the collision and also the momenta of the particles change magnitude. In **breakup** reaction, one or more particles are emitted from target nucleus and incident particle is not necessarily present in the final state. In **photo disintegration**, breakup of a nucleus is induced by an incident photon.

Usual notation for a reaction: $a + A = b + B$.

Table 1.1: Types of Nuclear Reactions and Observation about Nuclei and Nuclear Energy [8].

Reaction	Observation
Nucleon-nucleon Scattering	Fundamental Nuclear Force
Elastic Scattering	Nuclear Size and Interaction Potential
Inelastic Scattering	Energy Level Location and Quantum Numbers
Transfer and Knockout Reactions	Details of the Shell Model
Fusion Reactions	Astrophysical Processes
Fission Reactions	Properties of Liquid-drop Model
Compound Nucleus Formation	Statistical Properties of the Nucleus
Multifragmentation	Phases of Nuclear Matter, Collective Model
Pion Reactions	Investigation of the nuclear Glue
Electron Scattering	Quark Structure of Nuclei

A specific reaction is studied by measuring the angles and kinetic energies of the reaction products i.e the kinetic variables. The most important quantity for a specific set of kinematic variables is the cross section. Probability of a projectile to hit a target nucleus may be described by cross section. It is not the actual, physical cross sectional area of the nucleus. Cross sections depend on a variety of reaction variables. Different processes possible for a given particle incident on a nucleus have different cross sections.

Consider a beam of particles incident on a thin sheet of material having **n** nuclei per unit volume, thickness **t** and area **A**. If the particle gets close enough to a nucleus then there is a probability of some certain reaction. Let σ be the effective area of the nucleus for this particular reaction then total number of nuclei in the area **A** is **ntA**, effective area available for this reaction is $(\mathbf{ntA})\sigma$ and probability that this reaction will take place is $\mathbf{nt}\sigma$.

Various type of cross sections are total nuclear reaction cross section σ_r, differential scattering cross section $\frac{d\sigma}{d\Omega}$, nucleon removal cross section σ_{1N} etc. σ_r detect reaction products and it is one of the most fundamental quantities characterising nuclear reactions. It has been studied extensively both theoretically and experimentally. There are two kinds of formulations of σ_r which are basically different. One is the low energy theory such as Bass model [9], which is based on the one dimensional interaction potential between two spherical nuclei and second kind is the high energy microscopic Glauber model [10], which is based on the individual nucleon-nucleon collisions. $\frac{d\sigma}{d\Omega}$, detect only reaction products emitted at θ angle within a solid angle $d\omega$. Cross section measurement is the meeting ground between theory and experiment. Nuclear theory, using quantum mechanics predict the probability that a particular nuclear process will occur under certain conditions. The quantitative measure of this prediction is the cross section of the process.

1.1.1 Direct Reaction

Direct reaction includes variety of nuclear processes like inelastic or elastic nuclear collisions, stripping or pick-up reaction. This reaction proceeds without the formation of a compound nucleus. Both incident projectile and the target nucleus have a life of the order of 10^{-22} sec and interaction-potential depth in MeV where as the compound nucleus has a life time of the order of 10^{-14} sec with energy width in fraction of an

electron volt. Thus interaction time between the incident and target nucleus is very much shorter than the life of a corresponding compound nucleus. This was first recognised by [11] in analysing the low-energy (d,p) reactions. Experimentally it is observed that direct (d,p) reaction is more frequent than (d,n) reactions. However it is just opposite if the reaction occurs through compound nucleus process. Because of the absence of the Coulomb barrier, there would be a weight preponderance of the (d,n) reaction over the (d,p) reactions. The study of neutron pick-up reactions such as (d,p) reactions provide information for the understanding of the synthesis of stable isotopes in stellar burning processes. Theories based upon the distorted-wave Born approximation (DWBA) have been developed to describe the direct reactions.

Inelastic Scattering

Inelastic scattering is a fundamental scattering process in which the kinetic energy of an incident projectile is not conserved and the probability of inelastic scattering depends on the energy of the incident particle. In inelastic scattering, the incident particle is absorbed by the target nucleus, forming a compound nucleus. The compound nucleus will then emit a particle of lower kinetic energy which leaves the original nucleus in an excited state. The nucleus will emit this excess energy by γ emissions to reach its ground state. The investigation of inelastic scattering for both stable and exotic nuclei [12] to low lying collective states provide information on their collective strength, deformation parameters and also transition densities.

Elastic Scattering

Elastic scattering of particles by nuclei can occur in two ways. If the total kinetic energy is conserved and the nucleus returns to its ground state then this is known as compound elastic scattering. The second method, is called as potential elastic scattering which takes place with incident particles having energy about 1 MeV. In

potential scattering, the particle does not actually touch the nucleus and scattered by the short range nuclear forces when it comes close enough to the nucleus. The investigation of elastic scattering on both stable and exotic nuclei enables us to collect information on nuclear potentials and also on nuclear matter densities. Matter of interest, the p-p scattering on both stable and neutron rich nuclei at high energies was successfully investigated by G. D. Alkhazov et al [13, 14].

1.1.2 Spallation or Fission reaction

Nuclear fission is a nuclear reaction in which a nucleus breaks up, producing two or more smaller nuclei, subatomic particles, and energy. This phenomenon was first identified by Hahn and Strassmann in 1938. Heavy nuclei tend to be unstable because of the repulsive forces between their many protons. To increase their stability, atoms with heavy nuclei may split into atoms with lighter nuclei. This process is accompanied by a very large release of energy. Fission is the source of energy for all nuclear power generation used today. When some nuclei undergo fission, they release subatomic particles that trigger more fission reactions. This ongoing process in which one reaction initiates the next reaction is called a chain reaction. The cause of such nuclear breakdown is the large amount of charge. Bohr and Wheeler were able to explain the energy release in fission with the help of liquid-drop model and the compound nucleus reaction. They developed semi-empirical equation which could predict the amount of energy release during fission. The mechanism of fission is based on liquid-drop model and concerns about nuclear binding energies. As ^{235}U has an odd number of neutrons, the thermal neutron is strongly bound to the core nucleus, producing 6.4 MeV of energy. This energy is directly used in the excitation of ^{236}U. Since the fission barrier for ^{236}U is only 5.3 MeV thus the probability of fission occurring is high when ^{235}U absorbs a neutron. Similar calculations can be made for other nuclei which can undergo fission with how much energy will be released [15].

1.1.3 Multifragmentation Fission reaction

This is an exotic decay mode of thermal neutron fission where a number of prompt scission neutrons are released simultaneously with the two heavy fission fragments. These scission neutrons are the additional neutrons apart from the normal multiplicity of neutrons emitted from the fragments. The chain of thorium and uranium isotopes with neutron number N = 154-172 possess thermally fissile behaviour [16, 17] on the basis of fission barrier B_f and neutron separation energy S_n. All these nuclei are stable against alpha-decay and some of them have beta-decay half-life of several seconds [16, 17]. The fission decay mode of ^{250}U shows that it has a low fission barrier and large barrier width due to which it is more stable against spontaneous fission, but highly vulnerable to fission. It undergoes exotic mode of fission decay where surplus number of neutrons are released. It is worth mentioning that in multifragmentation fission along with the usual two big fragments [which we are used to] a few (about 3 neutrons in case of ^{250}U) neutrons come out from the fission process [16, 17]. In case of ^{250}U on an average of 5.5 neutrons will evolve. That is 3 multifragmentation neutrons and 2.5 prompt neutrons will come out per fission process. For more clarity, in case of ^{235}U, we get only 2.5 prompt neutrons and no multifragmentation neutrons. Now it is obvious that 5.5 prompt neutrons participate in the chain reaction in case of ^{250}U compared to the 2.5 neutrons of ^{235}U. As a result, neutron-rich thermally fissile nuclei reaches to the critical stage much faster than the normal thermally fissile material like ^{233,235}U and ^{239}Pu.

1.1.4 Fusion reaction

Fusion is defined as a reaction in which small nuclei combine together to form a composite system. It is the reverse process of fission. The power that fuels the sun and the stars is nuclear fusion. The stellar energy is produced by thermonuclear

reactions in which ^4He is formed by four protons. In a hydrogen bomb, two isotopes of hydrogen, deuterium and tritium are fused to form a nucleus of helium and a neutron. This fusion releases 17.6 MeV of energy. Unlike nuclear fission, there is no limit on the amount of the fusion that can occur. This reaction process is governed by quantum tunneling over the Coulomb barrier. Both theoretical and experimental studies have shown that fusion reactions at energies near and below the Coulomb barrier are strongly influenced by couplings of the relative motion of the colliding nuclei to several nuclear intrinsic motions [18]. With the present advancements in nuclear experimentation techniques, it has become possible to measure fusion cross sections with high accuracy in small energy intervals.

1.2 Nuclear Models

To study the observed properties of the nucleus of an atom it is necessary to have a sufficient knowledge about the nature of inter-nucleon interaction. The exact mathematical form of this interaction is still unknown. Yukawa's theory which is based on the exchange of a pion between two nucleons provides some idea of it but could not explain for more than one pion exchange. Even if the exact nature of the inter-nucleon interaction were known but it would have been difficult to develop a well established theory of the nuclear structure which consists of a large number of neutrons and protons as it is impossible to solve the Schrodinger equation exactly for such a many body system. Again it is quite different if we consider the theory of the atomic structure. Different models have been proposed for the nucleus in order to overcome the difficulties in developing a satisfactory theory of nuclear structure. Various models which have been proposed for the nucleus are liquid drop model, Shell model, collective model, Nilsson model etc.

Liquid Drop Model

The first and the simplest description of nuclei was provided by the liquid drop model. This model at macroscopic level examines the global properties of nuclei like density of the nuclear matter, binding energy per nucleon and nucleon distributions. The basic assumption of this model is that the nucleus is a charged non polar liquid drop held together by the nuclear force. This model was first proposed by N. Bohr and F. Kalckar in 1937 [19] and later on C. F. Von Weizsacker and H. A. Bethe construct a semi-empirical formula for the binding energy of the nucleus considering the above liquid drop. According to this theory, each individual molecule in a liquid drop exerts an attractive force upon immediate neighboring molecules. This force of interaction does not extend to all the molecules within the drop which is known as saturation of the force. To calculate the potential of the interaction, it is required to know the number of interacting pairs of molecules inside the liquid drop. As the inter-nucleon force within the nucleus has a saturation value, so each nucleon can interact only with a limited number of nucleons in its close vicinity. In this connection, based on liquid drop model, Bethe-Weizsacker formula gives a connection between the theory and experimental information of nuclear matter. If an element X of atomic number Z, neutron number N, mass number A = N + Z and M(A, Z) be the atomic mass then

$$M(A,Z) = ZM_H + NM_n - E_B. \tag{1.1}$$

The binding energy E_B can be expressed as the sum of a number of terms containing volume energy $E_V = a_1$A, surface energy E_S = - $a_2A^{2/3}$, Coulomb energy E_C = - $a_3\frac{z^2}{A^{1/3}}$, asymmetry energy E_a = - $a_4\frac{(A-Z)^2}{A}$, pairing energy $\delta = a_5A^{-3/4}$.

$$E_B(A,Z) = E_V + E_S - E_C - Ea + \delta \tag{1.2}$$

$$= a_1 A - a_2 \frac{Z^2}{A^{1/3}} - a_4 \frac{(A-2Z)^2}{A} + \delta. \tag{1.3}$$

Here δ is added for even-even nuclei and is subtracted for odd-odd Nuclei. For odd A nuclei, we take $\delta = 0$. This is the Bethe-Weizsacker formula for the nuclear binding energy. Thus this liquid drop model can explain the observed variation of the nuclear binding energy with the mass number and the fission of the heavy nuclei. It also provides the understanding of a large class of nuclear reactions.

Shell Model

According to this model each nucleon moves independently in a potential well created by rest of the nucleons. The potential well has constant depth in the interior of the nucleus and rapidly come to zero at the nuclear surface. Thus shell model is based on the existence of a spherically symmetric potential in the nucleus and a spin-orbit coupling term. Different types of coupling of the angular momenta gives different forms of shell model. This model was proposed by M. G. Mayer and J. H. D. Jensen in 1949 [20]. To know how the nucleons fill various quantum states of the nucleus, it is required to specify the mean potential. Experimental evidence supports that when a nucleus contains 2, 8, 20, 50, 82 or 126 protons or neutrons - the so called magic numbers - a shell closure occurs. In this regard attempts are made to understand this shell-closure property. Then electromagnetic and nuclear ground state properties of the nucleus are predicted in terms of the uncorrelated motion of single particles. The shape of the above potential well is in between the square well and the harmonic oscillator i.e Woods Saxon potential [21]. This potential is obtained by fitting data on nucleon -nucleus scattering. Woods Saxon potential is given by

$$V(r) = -\frac{V_0}{[1 + \ exp\mu(r-R)]}. \tag{1.4}$$

Where μ and R are constants in centimetre unit. A is the mass number of the nucleus and V_0 is in MeV. The shell model has been successfully applied to explain many features of the nucleus in the ground as well as in excited states.

Nilsson Model

The Nilsson model represents the self consistent potential by an axially symmetric oscillator potential with spin-orbit coupling. The single particle wave functions are obtained by solving the Schrodinger equation with this potential. To obtain the detailed characteristics of heavy, strongly deformed nuclei, the Hamiltonian of an anisotropic oscillator contains a spin-orbit term which is proportional to $\vec{l}.\vec{s}$ and another term proportional to l^2 [22]. The $\vec{l}.\vec{s}$ term provides the strong spin-orbit coupling of the nucleons where as the l^2 term favors large l value. The interaction of one nucleon with the nuclear field is represented by

$$H = H_0 + c\vec{l}.\vec{s} + Dl^2. \tag{1.5}$$

Where

$$H_0 = -\frac{\hbar}{2M}\nabla^2 + \frac{M}{2}\left[w_x^2 x'^2 + w_y^2 y'^2 + w_z^2 z'^2\right], \tag{1.6}$$

with x', y', z' are the co-ordinates of a particle in a co-ordinate system.

Nilsson introduced a single parameter of deformation and writes $w_x^2 = w_0^2(1 + \frac{2}{3}\delta) = w_y^2$, $w_z^2 = w_0^2$ (1-$\frac{4}{3}\delta$) with $w_x w_y w_z$ = constant. This is the condition of the constant volume of the nucleus.

Collective Model

The collective model is a simpler model in which the nucleus consists of a core and extra particles with the core being teated as a liquid drop. This was first suggested

by Rainwater and was then developed by Bohr and Mottelson [23] in detail. This model is useful to explain electric quadrupole moments for a number of nuclide. J-J coupling did not explain large values of quadrupole moment. If the nuclei are deformed, the many protons can give large values of the electric quadrupole moments. The deformation of the nucleus can occur due to polarising action of one or more loosely bound nucleons on the remaining nucleus.

The model is more useful if we consider the excitations of the even-even nuclei. Over the last several years data in this regard indicates that nuclei have ground-state spin and parity 0^+ and 2^+ in the first excited state. Emission of γ-rays from the first excited state to the ground state in even-even nuclei show that the transitions are of the electric quadrupole type. Some properties of both the shell model and the liquid drop model are explained by this model. However the principal assumption of this model, that is a number of nearly loose particles move in a slowly varying potential which arises from nuclear deformation is different from the independent particle model. The collective properties are evident if the lowest single particle state is coupled to the core excitation. Kissilinger and Sorensen [24] have done detail calculation for investigating the low energy states of spherical nuclei. In spherical nuclei, the coupling between the collective motion of the nucleons in the core and motion of the loose nucleons outside the core is weak. On other hand, for strong coupling the potential is not spherically symmetric. These particles maintains the deformed nuclear shape. Then the total energy is sum of the rotational, vibrational and nucleonic energies of the nucleus.

$$E_{total} = E_{rot} + E_{vib} + E_{nuc}. \tag{1.7}$$

Rotational and vibrational term is due to the collective motion of the nuclear core where as the nucleonic energy term is due to the motion of the loose nucleons. The calculations based on the collective model are more complex and some times difficult to differentiate among the various approaches. However, a large number of these

calculations nicely explain various nuclear properties such as transition probabilities, level energies, reaction rates and moments.

Methodology

To explain Nuclear Reaction and Nuclear Structure, one has to workout either in Non-relativistic or Relativistic frame work. Study of nuclear structure by Non-relativistic formalism is well established [5, 25, 26, 27]. For example, the solution of Schrödinger equation with Skyrme (zero range force) interaction as well as Gogny interaction (finite range force) are some of the successful methods in Nuclear Structure studies. The detail formalism of the Skyrme interaction for finite nuclei to evaluate binding energy, different radii, quadrupole deformation, single-particle energy and other properties will be discussed in Chapter 2. Similarly the recent successful model to study the nuclear properties in the relativistic mean field formalism [28, 29, 30] which is highlighted in Chapter 2. In nuclear reaction study, we take density as input which are obtained from various relativistic (RMF and E-RMF) and non-relativistic (SHF) models. Glaubr model calculates the reaction cross section taking these RMF or SHF densities as input. The detail of the Glauber model can be found in Chapter 2.

1.3 Non relativistic theory

It is known that the nuclear force can behave as if it was effectively just between pairs of nucleons. Using this assumption, we can practically calculate the observed properties of nuclei, consisting of several hundred interacting nucleons, with suitable chosen effective interactions. One of the basic problems in nuclear physics is to understand the nature of this strong interaction and to measure the properties of nuclei. The mean field concept provides the most basic and useful first step towards this end. The nuclear mean field is supposed to be generated by the interaction

of a nucleon with all the remaining nucleons. The most successful non-relativistic description for the ground-state nuclear properties had been in terms of Hartree-Fock (HF) [25, 26] and Hartee-Fock-Bogoliubov (HFB) formalism [5] using Skyrme type interaction. The parameters of Skyrme interaction are obtained through the least square fit to the nuclear matter and the ground state properties of a few spherical nuclei. However, this parameterization is not unique and as a result several parameter sets like SkI, SkII-SKIII [25, 26], SkM [27], SkM* [31] etc. exist and are still in use for the nuclear structure calculations.

1.4 Relativistic theory

Although non-relativistic, self-consistent mean field models have been successful in describing many nuclear properties but this approach is failed to predict correct binding energy and saturation density, which is well known as "Coester band" problem [32, 33]. In 1970's another significant approach in mean field models started, introducing the relativistic concept to the nuclei on the basis of earlier idea of Teller and Dürr [34, 35]. Walecka [36], Brockmann [37, 38] made the real calculations and put the foundation of the relativistic approach. The models based on the relativistic mean field approximation provide microscopically a consistent, simple and economical treatment of the nuclear many-body problem. By adjusting model parameters, coupling constants and effective masses to the global properties of nuclei on the stability line, the properties of the whole periodic table from light nuclei to super-heavy elements can be described. These models do not require any further fitting of the parameters for the nuclei away from stability line. Such models are proved to be very promising to describe the properties of nuclei not only on stability line, but also away from the stability line and the super-heavy nuclei. The study of nuclei far from the stability line have also strong astrophysical implications, especially in the context

of the r-process mechanism [39, 40]. The Relativistic Mean Field Theory (RMF) [28, 29, 30, 41], is not only able to reproduce the densities and binding energies for the finite nuclear matter but also yield spin-orbit interaction automatically in nuclei. Although, the results of the non-relativistic DDHF calculations using Skyrme forces are equally good but the RMF results are found to have a slight edge over their non-relativistic counterparts [41].

The general properties of nucleon-nucleon (NN) interaction have long been known. The first observed property of NN interaction was the saturation of nuclear forces. This can be seen by noting that, the binding energy per nucleon in a nucleus rapidly reaches roughly a constant value with increasing number of particles and there is a limit to the size of stable nucleus. This led Wigner [42] to infer, that the strong force among nucleons must be of short range and deduced that short range from the systematics of nuclear binding energy.

Yukawa realized that the range of nuclear force could be identified with the mass of the particle exchanged by a pair of interacting nucleons. Through the uncertainty principle, if two interacting particles exchange a meson of mass m, maximum range of the force associated with that particle will be of the order of 1/m (in natural system of units $\hbar$=c=1). Thus, the mass of the exchanged meson could be inferred from the known range of the NN force. The subsequent discovery of π-meson and its role in NN interaction led eventually to one-boson-exchange potential (OBEP). The role of different mesons contributing to the nuclear binding energy according to their masses can be found in Ref. [43]. The exchange of heavy mass ω-meson gives rise to the hard core potential and the virtual σ-meson is responsible for the intermediate range attractive force. Another iso-scalar meson δ(m_δ=983 MeV) has large mass and small coupling constant which provides only a small contribution [44]. The effect of δ-meson can be achieved by adjusting the parameters of other mesons. So, it is neglected in

the present model of relativistic mean field theory. The long tail part of the potential energy is due to the exchange of the light mass π-meson. All other mesons having mass similar or heavier than nucleon can be ignored. As we have mentioned earlier that the hadrons are observed in experiments, so, a theory at the hadron level may be more easily related to physical observable.

The RMF model used here, [29, 30, 41] is quite successful in describing the nuclear matter and finite nuclei. The details of the formalism are presented in Chapter 2. This theory has been used successfully, in the past decade by a number of authors [45, 46] and the references there in. In the RMF model usually positive energy baryonic states are considered, while studying the ground state properties of nuclei. The negative energy state (the anti-particles) are neglected which is called 'no sea-approximation'. We have used this approximation in the present work. The RMF has an advantage that, with the proper relativistic kinematics, the mesons and their properties already known or fixed from a few closed shell nuclei [41, 47, 48, 49, 50]. This method gives excellent results for binding energies, root mean square (rms) radii, quadrupole and hexadecupole deformations and the other nuclear properties, not only of spherical but also, of deformed nuclei. As we have mentioned earlier that one of the major attractive features of the RMF is spin-orbit interaction and associated nuclear shell structure which arise automatically from meson-nucleon interactions [51]. The main advantages of Relativistic Mean Field over Non-Relativistic Mean Field theories are [51]: (i) the proper relativistic propagation of nucleons and retarded interaction are included automatically, (ii) the meson degrees of freedom are incorporated explicitly through self-consistency, (iii) spin-orbit interaction, which is a relativistic correction, comes out automatically, (iv) Coester-Band Problem (Nuclear Saturation and Binding Energy Problem) is solved in relativistic mean field [52], (v) the mean velocity of nucleons in nuclei is about 2/3 of the speed of light indicates that a relativistic

approach can be applied to investigate the nuclear properties [53], (vi) the binding energy arises as a cancellation of two large contributions, the Lorentz scalar and vector terms [36], (vii) relativistic models have a slight edge over non-relativistic models in Nuclei or Nuclear Matter under extreme conditions, i.e. high density and high temperature. The experimental simulations of these conditions take place at relativistic energies in heavy ion collisions. A theoretical explanation of properties of high density matter therefore requires a relativistic approach from the out set [53].

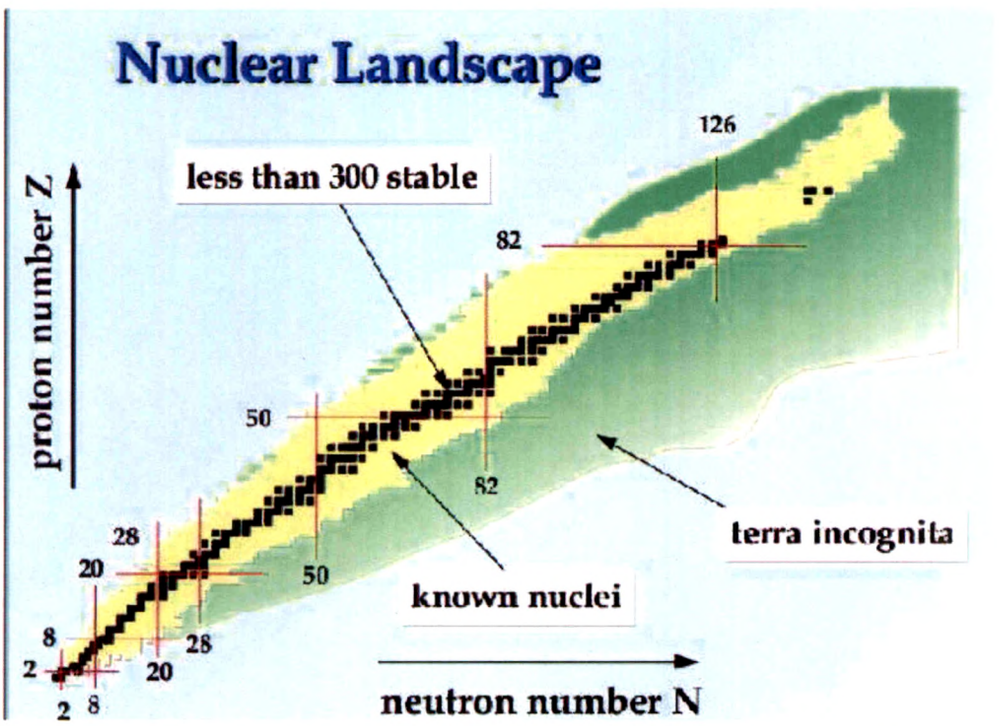

Figure 1.1: The nuclear chart showing stability, drip-line and super-heavy regions.

1.5 Drip-Line Nuclei

The drip-line region, neutron drip-line in particular is the least investigated area till date and has attracted much attention. Theoretically, more than 6000 nuclei might be bound by strong nuclear force. According to current estimate [54], between

5000 and 7000 bound nuclei should exist in the nuclear chart, but only $\approx$ 2000 of them have been observed to date. The nuclei can be formed up to certain number of nucleons beyond which the nucleus becomes unbound and the neutron (proton) separation energy $S_n(S_p)$ becomes zero. This point at which $S_n(S_p)= 0$ is called the drip-line. Thus, the drip-line is the last boundary far away from the stability line on the nuclear landscape beyond which addition of neutrons or protons is not possible. The drip-lines (neutron and proton) and the stability regions are shown in Fig. 1.1.

The dependence of effective nucleon-nucleon interaction on isospin is largely unknown [55] and the structure of single-particle states, collective modes and the behaviour, global nuclear properties are very uncertain in nuclei with extreme N/Z ratios. At the two-neutron drip-line, one can see a very interesting effect of negative two-neutron separation energies for particle-bound (negative Fermi energy) nuclei. This is the result of a sudden change in configuration when approaching the drip-line, that is caused by the fact that the ground-state configuration may become particle-unbound earlier than the excited one [56]. A similar effect occurs also in the heavy proton drip-line nuclei, where sequences of oblate ground states are obtained. Another effect at the proton drip line is related to long sequences of proton-magic (e. g., Z=50 and 82) isotopes intruding in the territory of unbound nuclei. This is the result of the vanishing pairing correlations, for which the proton Fermi energy coincides with the last occupied level, while in the neighboring nuclei it is located higher. So, the nuclei at proton drip-line are produced but large number of nuclei at neutron drip-line are yet to be discovered.

Recently, the properties of nuclei near the proton and neutron-drip lines have attracted much experimental and theoretical attention. We know that magic numbers are the back-bone of nuclear structure physics. For exotic nuclei near the drip-lines, recently, the question of appearance of new magic numbers and/or disappearance of

known magic numbers has been of much interest empirically, theoretically as well as experimentally. Theoretical calculations have predicted very different magic numbers for neutron-rich nuclei at the drip-line than the known ones for nuclei near the β-stability line [57, 58, 59, 60, 61, 62]. Most of these calculations are based on the mean-field models, namely the Skyrme-Hartree-Fock, Skyrme-Hartree-Fock-Bogoliubov interaction or the relativistic mean-field approximation. Experimentally, the vanishing of the $N = 20$ magic shell due to the observed large deformation of ^{32}Mg was shown in the early $\beta-$decay and Coulomb excitation studies [63, 64]. Similarly, the existence of $N = 28$ as a magic number was first questioned theoretically for ^{40}Mg, ^{42}Si and ^{44}S nuclei [58, 60, 62] and then a large quadrupole deformation was measured experimentally [65]. Very recently, some new magic numbers have also been predicted for the exotic neutron- and proton-rich nuclei near the drip-lines. Empirically, the analyses of measured binding energy data by Ozawa et al. [66] and the potential energy surfaces calculated from the Cluster-Core Model by Gupta et al. [67] suggest N =6 and 16 as the new magic numbers, for the proton- and neutron-rich drip-line regions respectively. However, as yet, there are no experimental signatures for the appearance of new magic numbers for nuclei near the neutron or proton drip-line, though, as stated above, the disappearance of magic numbers is already shown experimentally.

1.5.1 Exotic Nuclei

The exotic nuclei are having extraordinary neutron and proton ratio. They are highly unstable and decay to the stable nuclei. The halo in exotic nucleus was studied by Tanihata et al. [68, 69] as ^{11}Li. This nucleus although, has 11 nucleons only, but the size is almost equal to that of ^{208}Pb nucleus. They [68, 69, 70] analyzed systematically such interaction cross section data and used Glauber theory to extract the nuclear root mean square radii. The sudden increase in the interaction cross

section was then attributed to the relatively large rms radius as compared to the expected from the conventional $1.2A^{\frac{1}{3}}$ law. This was called the neutron halo. With the advancement of the technology several such nuclei with exotic properties have been found. Many of the traditional nuclear physics concepts are not able to explain this phenomena. More than 150 years elapsed between the discovery of uranium (Z=92) in 1789 and neptunium (Np, Z=93), the first transuranium element, in 1940. At present we know 26 man-made transuranium elements, out of which 9-elements are transactinide starting from Z=104. Among 3000 known nuclei only 287 have survived in nature after the nucleosynthesis. Now, 118 elements have been identified, named and placed in the periodic table and few neutron deficient isotopes Z=111-118 have been synthesized in the laboratory. The detailed understanding of structure of exotic nuclei is intimately connected to astrophysics [71], since the nucleosynthesis which usually happens inside massive stars is taking place in the region of extreme neutron to proton ratios.

1.5.2 Halo Nuclei

The term halo refers to the weakly bound nucleons forming a cloud of low density around a core of normal density. Halo nuclei that have been observed so far include a variety of configurations. The most basic one is the one-neutron halo. This is a two-body system consisting of the core and one neutron. A halo case also consists of more than one nucleon, as in the case for two-neutron halo. So far a four-neutron halo nuclei has been observed which is called as a neutron skin [72]. There is also evidence of proton halos. The halo nuclei observed so far are presented in Fig. 1.2

Halo structures can also be observed in excited states, where separation energy becomes small enough, e. g ^{17}F [73]. It is also possible that core of a halo system is in an excited state. The variety of characteristics makes clear that there is no simple definition for a halo nucleus. With the present advancements in nuclear experimer-

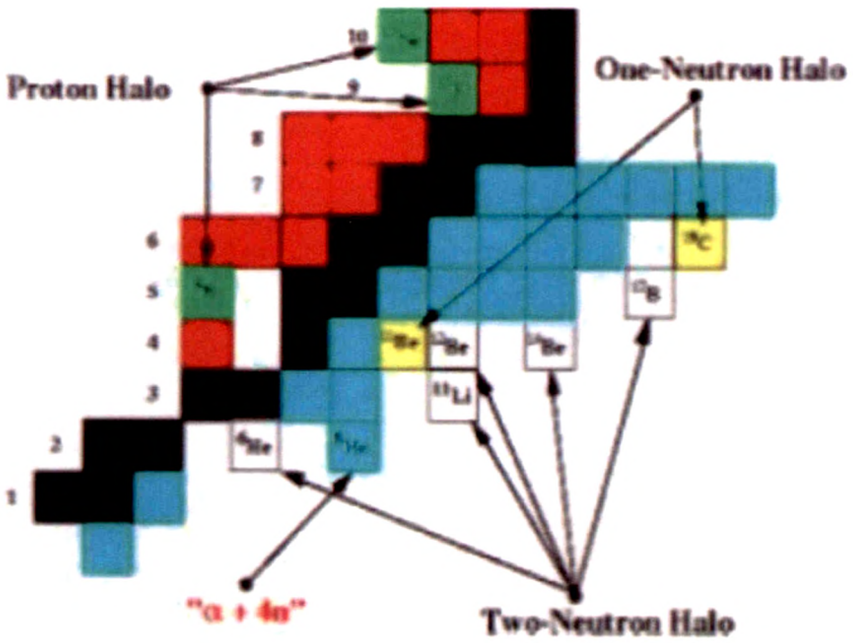

Figure 1.2: Chart of ground state halo nuclei.

tation technique, it has become possible to explore nuclei chart towards the driplines. The detailed information on these exotic nuclei far from the valley of stability can be collected with the modern technologies of heavy ion accelerators and radioactive ion beam (RIB) facilities. This information is essential for the discovery of the novel structures of halo nuclei.

The nucleus ^{8}B, the ground state proton halo, has an important influence on the proton capture cross section. The large spatial expansion of the proton wave function in ^{7}Be yield β^{+} decay of ^{8}B, a high energy neutrino is emitted, which is required for testing the standard solar model. Unstable nuclei particularly some halo nuclei, play an important role in the nucleosynthesis. This process is responsible for the existence of us and the universe around us.

1.6 Super-heavy Nuclei

The super-heavy region of nuclear chart has been a topic of interest since 1960's with the prediction of stable island of super-heavy nuclei in theoretical calculations based on macroscopic-microscopic model [74], but it was very difficult to test it experimentally at that time. The stability of the nuclei in super-heavy region is attributed to the shell effects. The strong shell stabilization was realized with the invention of shell correction method in super-heavy nuclei [75, 76, 77, 78]. The center of island of stability was predicted to be around Z=114, N=184 [75, 76, 77, 78, 79]. As the number of neutrons increases the fission barrier becomes thicker as a result of which the nuclei become more stable against fission.

The properties and structure of super-heavy nuclei have been investigated extensively using various approaches during the last four decades. These approaches consist of microscopic nature such as non-relativistic density-dependent Skyrme-Hartree-Fock (SHF) theory and Relativistic Mean Field (RMF) theory or macroscopic-microscopic (mic-mac) type calculations. In the mac-mic category the total binding energy of nuclei is obtained as sum of smooth energy based on liquid-drop type on which shell correction is imposed using the method of Strutinsky [74]. The most notable in this direction with shell correction energy calculation is Finite Range Droplet Model (FRDM) [80, 81], used in order to identify major magic numbers in the region of super-heavy nuclei.. One of the basic task in the present day structure physics in super-heavy nuclei is the neutron and proton magic numbers next to Z=82 and N=126. A number of calculations have been made earlier in this region for the next magic number. The FRDM predicts the proton magic number at Z=114 as the next to known magic Z=82 [75, 76, 77, 78]. The experimental data gives support to this number [82, 83]. Also, Z=114 and N=164 double sub-shell closure is reported in a systematic study of Z=114 nucleus [84]. On the other hand the self-consistent mean field models which

are proved to be very promising tools in the description of the nuclear properties for the last two decades, predict Z=120, N=172 or 184 as the next shell closure instead of Z=114 and N=184 [85, 86]. While the first mean field model, Hartree-Fock with Skyrme interaction [87, 88] in the non-relativistic mean field regime predicts Z=126, N=184 as the next shell closure for the calculations of tranceactinide and the synthesis of nuclear properties of actinide. Thus the study of super-heavy nuclei seems to hold more new surprises and motivations for the investigation. We are interested in the extended regions of stability not only in the directions of both the drip-lines (neutron- and proton-rich side) but also in the heavier mass region. Also the region of super-heavy elements itself is extended to the drip-lines.

Relativistic mean field concept has attracted much attention in the last two decades, the models are Relativistic-Hartree-Bogoliubov (RHB) and RMF (Hartree approximation). The binding energy is the only quantity, which is so far measured experimentally for the super-heavy nuclei. Therefore, detailed study of properties will give the insight of the nuclei in the ground state and will be helpful for the prediction of unknown shapes in this region. By comparing the calculated binding energy with the experiments, the other quantities, such as the root mean square matter (rms) radii, charge radii, quadrupole deformations, shell gaps and the excited state energies can be predicted, which will help the experiments to measure these quantities. The earlier investigations by the authors of Refs. [45, 89, 90] have predicted that the magic numbers near the proton drip-line do not follow the conventional magic number sequence of the nuclei near stability line. Therefore, it is worthwhile to make investigation to see the sequence of neutron/proton magic numbers and the next magic proton and neutron numbers on the drip-lines and the extended mass region of the super-heavy nuclei.

1.7 r-process

The r-process nucleosynthesis is believed to be responsible for the production of a half of heavy elements in the Universe and is one of the most important issues in nuclear astrophysics. To clarify about the r-process, nuclear physics plays crucial roles through the nature of unstable nuclei, while astrophysics and astronomy provide significant information on the history of nucleosynthesis in the Universe [91]. The r-process is the rapid neutron capture process by successive neutron captures to create heavy elements up to uranium region [92]. Starting from some light elements, the r-process goes through the neutron-rich region of the nuclear landscape in extremely neutron-rich, astrophysical environments. When the neutron flux ceases, neutron-rich and unstable heavy-elements decay back to the stability line to produce the stable heavy-elements. Due to r-process, there are abundant elements around the magic numbers by forming peaks around A=130 and A=195, at the stability line. It is necessary to study the r-process since both theories and experiments have been revealing the properties of unstable nuclei in the neutron-rich region. The important question is where and how the r-process occurs in the Universe. The most plausible site is the supernova explosion of massive stars in the mass range of 10-30 MB. However, we do not know which mass range of stars contributes to the r-process. To clarify about the r-process by the latest nuclear data of unstable nuclei, we have to connect nuclear physics with astrophysics.

1.8 Plan of thesis

The thesis is organised as follows:

In **Chapter 2.** we present both non-relativistic and relativistic models in detail. The Skyrme Hartee-Fock (SHF), Relativistic mean field model (RMF), Relativistic effective field theory approach (E-RMF), Glauber Model and Coupled Channel

Formalism with a brief historical development of the models are discussed. The parameter sets, used in the calculations, are also presented. The numerical procedure is also given in brief.

In **Chapter 3.** we present nuclear shell structure both for ground and intrinsic excited (or isomeric) states in the frame work SHF, RMF and E-RMF formalisms. First of all, we study the total density ρ, proton density ρ_p and neutron density ρ_n distribution for various light, medium and heavy nuclei with SKI4, SLy6, NL3, NL3*, NLSH and G2 parameter sets. In ground states we study the bulk properties, such as binding energy (BE), root mean square charge radius r_{ch}, matter radius r_m and quadrupole deformation parameter β_2 in three different regions. The calculated results are compared with the experimental data wherever available. In this connection we have also studied the relative isotopic proton and neutron density differences $\Delta\rho_p(r)$ and $\Delta\rho_n(r)$ for Ca isotopes.

We also employ the axially deformed RMF and non-relativistic mean field techniques to investigate the bulk properties for intrinsic excited state. The calculated results are compared with the widely acceptable finite range droplet model (FRDM) and with the experimental data wherever available. Here we study the ground and the first excited intrinsic states of ^{53}Co, and its mirror nucleus ^{53}Fe, within the frameworks of the SHF and RMF formalisms. The single-particle energy spectra of these nuclei is analysed with the well trusted parameter sets NL3 and NL-SH. We also investigate the potential energy surfaces (PES) for both the nuclei within the RMF and SHF techniques.

In **Chapter 4.** we apply above RMF and E-RMF formalisms to calculate the total nuclear reaction and differential elastic scattering cross sections of exotic nuclei in the framework of Glauber model. The nuclear densities from the RMF and E-RMF models for the projectile and target nuclei, which are the main ingredients of the calculation of total nuclear reaction cross sections, have been fitted to a sum

of two Gaussians, and the coefficients c_1, c_2 and ranges a_1, a_2 are calculated. This fitting procedure simplifies the numerical calculations considerably and makes it possible to obtain analytic expressions for the transparency functions. In other words, using these coefficients, we got the equivalent density for calculating the transparency functions, which are further used to estimate total nuclear reaction and differential elastic scattering cross sections. Both light and heavy nuclei are taken as the representative targets and light neutron-rich nuclei as projectiles. In order to see the effect of the neutron-richness of the projectile in the exotic mass region, we repeated the calculations with various projectile masses without changing the target nucleus. The differential elastic scattering cross section is evaluated for some selected systems at various incident energies. The dependence of differential elastic scattering cross section for the recently discussed superheavy element with atomic number Z=122 or 124 is also presented. The application of the model to this superheavy element is interesting because of the possibility of the formation of highly neutron-rich superheavy element in earth crust.

The **Chapter 5.** is devoted to calculate the one nucleon removal reaction cross sections (σ_{-1n} and σ_{-1p}) for few stable and neutron-rich halo nuclei with^{12}C as target, using RMF densities, in the frame work of Glauber model. The results are compared with the experimental data. Study of the stable nuclei with the deformed densities have shown a good agreement with the data, however, it differs significantly for the halo nuclei. We observe that while estimating the σ_{-1n}value from the difference of reaction cross section of two neighboring nuclei with mass number A and that of A-1 in an isotopic chain, we get good agreement with the known experimental data for the halo cases.

In **Chapter 6.** we extend the idea of the preceding chapter and discuss the possibility of existence of superheavy nuclei. Here we emphasize on the reaction and the fusion cross sections of neutron-rich heavy nuclei taking light exotic isotopes

as projectiles. Results of neutron-rich Pb and U isotopes are demonstrated as the representative targets and He, B as the projectiles. The Gluaber Model and the Coupled Channel Formalism are used to evaluate the reaction and the fusion cross sections for the cases considered. Based on the analysis of these cross sections, we predict the formation of heavy, superheavy and super-superheavy elements through rapid neutron/light nuclei capture r-process of the nucleosynthesis in astrophysical objects.

We also studied the structural properties of the recently predicted thermally fissile neutron-rich Uranium and Thorium isotopes using the RMF formalism. The investigation of the new phenomena of multifragmentation fission is analysed. The anatomy of the fission process is discussed with the help of the neck configurations. In addition to the fission properties, the total reaction cross section of these nuclei are evaluated taking ^{6,11}Li and ^{16,24}O as projectiles. The possible use of nuclear fuel in an accelerator based reactor is discussed which may be the substitution of ^{233,235}U and ^{239}Pu for nuclear fuel in near future.

Finally, in **Chapter 7.** we summarize our results and some future prospects are mentioned briefly.

Chapter 2

Formalism

2.1 Introduction

The development of a general nuclear reaction formalism has been the subject over many years. Many different aspects of the nucleon-nucleus interaction show themselves in a variety of nuclear reaction and scattering phenomena ranging from compound nucleus formation to direct reactions. Since these processes are all connected with the basic properties of the nuclear many-body system that manifest themselves in different ways under different experimental conditions, one can expect a variety of reaction formalisms that are each designed to bring out a particular aspect of the reaction mechanism. Now a general theory of reactions should contain elements characterizing all possible reaction processes that can take place in a given nuclear reaction and also provide a means for connecting the occurrence of such processes with the more fundamental properties of the many-body system.

The theoretical description of complex many-body system, the nucleus requires the solution of many-body problem, which till to date is not available. Therefore, approximate schemes have been developed for this purpose. The mean field concept provides the most basic and useful first step towards this end. The mean field models have made a considerable progress in the past three decades [93]. The self-consistent mean-field models are intermediate between the microscopic many-body theories like

the Brückner-Hartree-Fock (BHF) [93] and the semi-classical models like macroscopic-microscopic method [94], although the precision is still limited. The self-consistent mean field models are one step towards a fully microscopic description of nuclei. They produce appropriate single particle potential corresponding to actual density distribution for a given nucleus, although they cannot be handled as an *ab initio* treatment, because the nuclear interaction induces huge short-range correlations. The self-consistent mean field models deal with effective energy functionals.

To study the nuclear reaction mechanism, one need the structural information like density, nucleon-nucleon interaction etc. To get these inputs some reliable models are required. If the inputs are trust worthy enough, our prediction will be authentic accordingly. So we have considered both non-relativistic and relativistic mean field models for the required inputs. The nuclear mean field is supposed to be generated by the interaction of a nucleon with all the remaining nucleons. The most successful non-relativistic description for the ground-state nuclear properties has been in terms of Hartree-Fock (HF) [25, 26] and Hartree-Fock-Bogoliubov (HFB) formalisms [5], using Skyrme type interaction. The parameters of Skyrme interaction are obtained through the least squares fit to the nuclear matter and the ground state properties of a few spherical nuclei. However, these parameterizations are not unique; as a result several parameter sets like SkI, SkII-SKIII, SkM, SkM* etc. exist which are in use for the nuclear structure and reaction properties calculations.

2.2 Skyrme Hartree-Fock (SHF) Theory

There are many known parameterizations of Skyrme interaction which reproduce the experimental data for ground-state properties of finite nuclei and for the observables of infinite nuclear matter at saturation densities, giving more or less comparable agreements with the experimental or expected empirical data. The general form of

the Skyrme effective interaction, used in the mean-field models, can be expressed as an energy density functional $\mathcal{H}$ [95, 96], given as a function of some empirical parameters, as

$$\mathcal{H} = \mathcal{K} + \mathcal{H}_0 + \mathcal{H}_3 + \mathcal{H}_{eff} + \cdots \tag{2.1}$$

where $\mathcal{K}$ is the kinetic energy term, $\mathcal{H}_0$ the zero range, $\mathcal{H}_3$ the density dependent and $\mathcal{H}_{eff}$ the effective-mass dependent terms, which are relevant for calculating the properties of nuclear matter. These are functions of 9 parameters t_i, x_i $(i = 0, 1, 2, 3)$ and η, and are given as

$$\mathcal{H}_0 = \frac{1}{4}t_0\left[(2+x_0)\rho^2 - (2x_0+1)(\rho_p^2+\rho_n^2)\right], \tag{2.2}$$

$$\mathcal{H}_3 = \frac{1}{24}t_3\rho^\eta\left[(2+x_3)\rho^2 - (2x_3+1)(\rho_p^2+\rho_n^2)\right], \tag{2.3}$$

$$\begin{aligned}\mathcal{H}_{eff} &= \frac{1}{8}\left[t_1(2+x_1)+t_2(2+x_2)\right]\tau\rho \\ &\quad + \frac{1}{8}\left[t_2(2x_2+1)-t_1(2x_1+1)\right](\tau_p\rho_p+\tau_n\rho_n).\end{aligned} \tag{2.4}$$

The kinetic energy $\mathcal{K} = \frac{\hbar^2}{2m}\tau$, a form used in the Fermi gas model for non-interacting fermions. The other terms, representing the surface contributions of a finite nucleus with b_4 and b_4' as additional parameters, are

$$\begin{aligned}\mathcal{H}_{S\rho} &= \frac{1}{16}\left[3t_1(1+\frac{1}{2}x_1) - t_2(1+\frac{1}{2}x_2)\right](\vec{\nabla}\rho)^2 \\ &\quad -\frac{1}{16}\left[3t_1(x_1+\frac{1}{2}) + t_2(x_2+\frac{1}{2})\right] \\ &\quad \times\left[(\vec{\nabla}\rho_n)^2 + (\vec{\nabla}\rho_p)^2\right],\end{aligned} \tag{2.5}$$

$$\mathcal{H}_{S\vec{J}} = -\frac{1}{2}\left[b_4\rho\vec{\nabla}\cdot\vec{J} + b_4'(\rho_n\vec{\nabla}\cdot\vec{J}_n + \rho_p\vec{\nabla}\cdot\vec{J}_p)\right]. \tag{2.6}$$

Here, the total nucleon number density $\rho = \rho_n + \rho_p$, the kinetic energy density $\tau = \tau_n + \tau_p$, and the spin-orbit density $\vec{J} = \vec{J}_n + \vec{J}_p$. The subscripts n and p refer to neutron and proton, respectively, and m is the nucleon mass. The $\vec{J}_q = 0$, $q = n$ or p, for spin-saturated nuclei, i.e., for nuclei with major oscillator shells completely filled. The total binding energy (BE) of a nucleus is the integral of the energy density functional $\mathcal{H}$. At least eighty-seven parameterizations of the Skyrme interaction are published since 1972 (see, e.g., [97]). In most of the Skyrme parameter sets, the coefficients of the spin-orbit potential are $b_4 = b'_4 = W_0$ [98], but we have used here the Skyrme SkI4 set as given in Table 2.1 with $b_4 \neq b'_4$ [99]. This parameter set is designed for considerations of proper spin-orbit interaction in finite nuclei, related to the isotope shifts in Pb region. Several more recent Skyrme parameters such as SLy1-10, SkX, SkI5 and SkI6 are obtained by fitting the Hartree-Fock (HF) results with experimental data for nuclei starting from stability to neutron and proton drip-lines [95, 99, 100, 101].

Table 2.1: Different parameter sets used in the non-relativistic formalism.

parameter	SKO	SKI2	SKI4	SLy4	SLy6
t_0	-2103.7	-1915.4	-1855.8	-2488.9	-2479.5
t_1	303.4	438.4	473.8	486.8	462.2
t_2	791.7	305.4	1006.9	-546.4	-448.6
t_3	13553	10548	9703	13777	13673
x_0	-0.21	-0.21	0.41	0.83	0.82
x_1	-2.81	-1.74	-2.89	-0.34	-0.47
x_2	-1.46	-1.53	-1.33	-1.00	-1.00
x_3	-0.43	-0.18	1.15	1.35	1.36
α	0.25	0.25	0.25	0.17	0.17
Nuclear	Matter	Properties			
$M*_s/M$	0.90	0.68	0.65	0.69	0.69
a_{sym} (MeV)	32.01	33.42	29.54	32.04	32.00
K (MeV)	223.7	241.3	248.4	230.4	230.3
ρ_0(fm$^-$3)	0.161	0.158	0.160	0.160	0.159
BE/A (MeV)	15.83	15.77	15.94	15.97	15.92

2.3 Relativistic Mean Field (RMF) Theory

The early idea of Schiff [102], Teller and Dürr [34, 35], forgotten for nearly twenty years till 1970's, was picked up by Green and Miller [28] and later on by Walecka [29] who pointed out the power, the simplicity and the elegance of the phenomenological relativistic description of the nuclear system. Walecka and collaborators [36] proposed a linear model which included only a very few degrees of freedom. Finite nuclei, determined to a large extent by the surface properties, can not be described in this simple Walecka model. The break through came with the inclusion of an effective density dependence in the model, by Boguta and Bodmer [30], in the form of non-linear coupling terms among the mesons that was development further by many other authors [103, 104]. This non-linear model is known today as Relativistic Mean Field (RMF) theory. Since then it has gained considerable recognition not only for the description of scattering at intermediate energies but also for the properties of nuclei at low energies. This method starts from a relativistic Lagrangian which contains mesonic and nucleonic degrees of freedom a relativistic analogue of the concepts of density dependent Hartree-Fock calculations with Skyrme forces. However, the mesonic degrees of freedom are not eliminated here like in the non-relativistic case. The theory is, therefore, relativistic quantum field theory from the beginning. This model is developed within the framework of quantum hydrodynamics (QHD) where the appropriate degrees of freedom are baryons and mesons. Because of its proper treatment of spin-orbit splitting, this model is expected to be more reliable, than the non-relativistic models, in predicting yet unknown properties of nuclei far from stability line, which are important in astrophysical situations. Also in some respects this method is simpler than Skyrme type calculations, since RMF method involves local quantities such as local densities and fields.

In recent years, the microscopic description of ground state properties of finite

nuclei has been attempted by using the relativistic field theory for the nuclear many-body problem. RMF theory, which starts from an effective Lagrangian containing the nucleonic and mesonic degrees of freedom, is a phenomenological theory of the nuclear many-body problem. It incorporates four basic assumptions: (i) the nucleons are treated as point-like particles, (ii) these particles obey strictly the rules of relativity and causality, (iii) the theory is fully Lorentz invariant, and (iv) the particles move independently in mean fields which originate from nucleon-nucleon interaction. The conditions of causality and Lorentz invariance impose that the interaction is mediated by the exchange of point-like effective mesons, which couple to the nucleons at local vertices. Under these assumptions, the nucleons are treated as Dirac particles described by Dirac spinor ψ. The point-like particles are called mesons ϕ_j, where j stands for σ, ω, ρ and photon fields. They are characterized by their quantum numbers, masses (m_j) and coupling constants (g's). The number of mesons, their masses, coupling constants and quantum numbers such as spin (J), parity (P) and isospin (I) are determined in such a way as to reproduce the experimental data. The mesons are treated as the classical fields. Their dynamics is determined through a Lagrangian density $\mathcal{L}(\phi, \partial_\mu \phi, t)$ and the variational principle:

$$\delta \int dt L = \delta \int d^4x \mathcal{L}(\phi, \partial_\mu \phi, t) = 0, \tag{2.7}$$

which on the classical level gives the Euler-Lagrange equations of motion:

$$\partial_\mu \left(\frac{\partial \mathcal{L}}{\partial(\partial_\mu \phi_j)}\right) - \frac{\partial \mathcal{L}}{\partial \phi_j} = 0. \tag{2.8}$$

The energy momentum tensor [36] is given by

$$T^{\mu\nu} = -g^{\mu\nu}\mathcal{L} + \frac{\partial \mathcal{L}}{\partial(\partial_\mu \phi_j)} \partial^\nu \phi_j. \tag{2.9}$$

The Euler-Lagrange equation ensures that this quality is conserved. The continuity equation is

$$\partial_\mu T^{\mu\nu} = 0. \tag{2.10}$$

If $\mathcal{L}$ has no explicit space dependence then the four-momentum, defined by

$$P^\nu = \int d^3r T^{0\nu}, \tag{2.11}$$

is conserved. The energy is the zeroth component of the four-momentum

$$P^0 = E = \int d^3r \mathcal{H}(r). \tag{2.12}$$

The Hamiltonian density is:

$$\mathcal{H}(r) = T^{00} = \frac{\partial \mathcal{L}}{\partial q_j}\phi_j - \mathcal{L}. \tag{2.13}$$

Thus, the total binding energy E of the nucleus is given by

$$E = \int d^3r \mathcal{H}(r) = \int T^{00} d^3r. \tag{2.14}$$

In principle, there are many possible mesons which are characterized by the quantum numbers J, P and I. The well known π-meson carries the quantum numbers J=0, I=1 and P=-1. Since π-meson carries the negative parity, the corresponding mean field breaks on Hartree level and its contribution is zero. This is certainly not the case in real nuclei where the mean field is parity conserving to a very high degree of accuracy i.e. assumed to be of well defined parity. Therefore, the effects of $\pi-$mesons average essentially to zero in the description of bulk properties of nuclei [36, 105]. Also, the ground state has well defined charge and thus the expectation values for charged $\rho-$field operators vanish as well. To include the π-meson, we have to go

beyond mean field. Two or any even number of pions, however, contribute to the positive parity fields; therefore one includes the phenomenological σ-meson. The charge independent and spin dependent character of nuclear force is described by the different mesons. The exchange of σ-meson which is a resonance state of 2π (s-wave) leads to attractive nuclear force among the nucleons and the corresponding field is scalar field σ(r). The repulsive nuclear force comes into play due to the exchange of vector mesons. The most important one is ω-meson. The experimentally known vector meson (3π-resonance state) generates ω^{μ}(r) field whose time-like component is responsible for repulsive force. The isospin dependence of nuclear force is taken care by the exchange of ρ-mesons. In fact, pion would carry the isospin, but as contribution of pion on Hartree level is zero, therefore, the ρ-field (2π-resonance, p-state) takes care of this aspect phenomenologically. The electromagnetic field of photon is described by vector potential A^{μ}(r) and its time-like component represents Coulomb repulsion. A more detailed specification about the degrees of freedom is shown in the table 2.2. The ρ-mesons have the same quark composition as that of π, but the mass is about five and one half times the π-mesons; therefore, ρ-mesons are considered to be the excited state of π-mesons.

Table 2.2: The degree (deg.) of freedom, the quantum numbers and the nature of interactions of different mesons are shown.

Deg. of freedom	Mass (MeV)	Spin J^P	Isospin (I, I_z)	Charge	Type of force
n (nucleon)	939.0	1/2	1/2; −1/2	0	free
p (nucleon)	939.0	1/2	1/2; +1/2	1	free
σ (scalar)	520.0	0^+	0, 0	0	attractive and spin-orbit
ω (vector)	783.0	1^-	0, 0	0	repulsive, tensor and spin-orbit
ρ (vector)	770.0	1^-	1	0	tensor
γ (photon)	0	1	0, 0	0	Coulomb repulsive and tensor
π	139.0	0^-	1; ± 1, 0	± 1, 0	not included

In principle, there are other mesons also which play the role in quantitative description of bare nucleon-nucleon interaction by meson exchange [105]. For example, δ-meson leads to scalar nuclear potential, slightly different for protons and neutrons. The contribution of this meson is small, and the effect of which can be achieved by a suitable adjustment of the parameters in Lagrangian for other mesons. Therefore, neglecting the other mesons, only σ(r), ω^{μ}(r), $\vec{\rho}^{\mu}$(r) and the photon A^{μ} fields are considered. The masses of other mesons are more than the mass of nucleons, and hence contribution of heavy mass mesons can be neglected to a good approximation.

2.4 Lagrangian Density

Here we outline the non-linear RMF Lagrangian of Walecka, extended by the addition of self-coupling of σ-meson by Boguta and Bodmer [30]. This Lagrangian, later is used by many authors [41, 45, 46, 106, 107] to investigate the ground state properties of nuclei in the nuclear chart. The Lagrangian describing the contribution of all mesons and nucleons is

$$\mathcal{L} = \mathcal{L}_B + \mathcal{L}_{\mathcal{M}} + \mathcal{L}_{\mathcal{M}B}. \tag{2.15}$$

This equation contains free nucleons described by the Lagrangian density

$$\mathcal{L}_B = \overline{\psi_i}\{i\gamma^{\mu}\partial_{\mu} - M\}\psi_i, \tag{2.16}$$

where M is the nucleon mass and ψ_i is Dirac spinor. The Lagrangian densities ($\mathcal{L}_{\mathcal{M}}$=$\mathcal{L}_{\sigma}$+$\mathcal{L}_{\omega}$ +$\mathcal{L}_{\rho}$) for free mesons contain the following contributions:

$$\mathcal{L}_{\sigma} = \frac{1}{2}\partial^{\mu}\sigma\partial_{\mu}\sigma - U(\sigma), \tag{2.17}$$

$$\mathcal{L}_{\omega} = -\frac{1}{4}\Omega^{\mu\nu}\Omega_{\mu\nu} + \frac{1}{2}m_{\omega}^{2}V^{\mu}V_{\mu} + \frac{1}{4}c_3(V_{\mu}V^{\mu})^2, \tag{2.18}$$

$$\mathcal{L}_{\rho} = \frac{1}{2}m_{\rho}^{2}\vec{R}^{\mu}.\vec{R}_{\mu} - \frac{1}{4}F^{\mu\nu}F_{\mu\nu} - \frac{1}{4}\vec{B}^{\mu\nu}.\vec{B}_{\mu\nu}, \tag{2.19}$$

where $U(\sigma)$ is the non-linear potential for the σ-mesons. It takes into account the density dependence in a phenomenological way and it has the form [30]:

$$U(\sigma) = \frac{1}{2}m_\sigma^2\sigma^2 - \frac{1}{3}g_2\sigma^3 - \frac{1}{4}g_3\sigma^4 \tag{2.20}$$

The interaction among nucleons and mesons are given by the following part of Lagrangian density:

$$\mathcal{L}_{MB} = -g_s\overline{\psi}_i\psi_i\sigma - g_w\overline{\psi}_i\gamma^\mu\psi_i V_\mu - g_\rho\overline{\psi}_i\gamma^\mu\vec{\tau}\psi_i - e\overline{\psi}_i\gamma^\mu\frac{(1+\tau_3)}{2}\psi_i A_\mu, \tag{2.21}$$

where the coupling constants in the above equations (2.20 and 2.21), g_σ, g_ω, g_ρ and $\frac{e}{4\pi} = \frac{1}{137}$ are for $\sigma-$, $\omega-$, $\rho-$mesons and photon, respectively. $\vec{\tau}$ ($\vec{\tau}_3$) is Pauli isospin matrix (third component of τ) for the nucleon spinor (τ_3=-1 for neutron and +1 for proton). c_3 is the coupling constant of non-linear terms for $\omega-$mesons. The field tensors $\Omega^{\mu\nu}$, $R^{\mu\nu}$ corresponding to the ω- and ρ-mesons and $F^{\mu\nu}$ corresponding to the electromagnetic field appearing in the Lagrangian are given by:

$$\begin{aligned}
\Omega^{\mu\nu} &= \partial^\mu\omega^\nu - \partial^\nu\omega^\mu \\
R^{\mu\nu} &= \partial^\mu\vec{\rho}^\nu - \partial^\nu\vec{\rho}^\mu - g_\rho(\vec{R}^\mu \times \vec{R}^\nu) \\
F^{\mu\nu} &= \partial^\mu A^\nu - \partial^\nu A^\mu
\end{aligned} \tag{2.22}$$

The quantities with overhead arrows are iso-vector. The $R^{\mu\nu}$ has a non-Abelian vector field. However, for simplicity we approximate $R^{\mu\nu} \approx \partial^\mu\vec{\rho}^\nu - \partial^\nu\vec{\rho}^\mu$.

2.5 Relativistic Mean Field Equations

The relativistic mean field (RMF) energy density for finite nuclei containing tensor couplings and meson interactions is given by [108]

$$
\begin{aligned}
\mathcal{E}(\mathbf{r}) \;=\; & \sum_{\alpha}\varphi_{\alpha}^{\dagger}\Big\{ -i\boldsymbol{\alpha}\cdot\boldsymbol{\nabla}+\beta(M-\Phi)+W+\frac{1}{2}\tau_3 R+\frac{1+\tau_3}{2}A \\
& -\frac{i}{2M}\beta\boldsymbol{\alpha}\cdot\Big(f_v\boldsymbol{\nabla}W+\frac{1}{2}f_\rho\tau_3\boldsymbol{\nabla}R+\lambda\boldsymbol{\nabla}A\Big)+\frac{1}{2M^2}\left(\beta_s+\beta_v\tau_3\right)\Delta A\Big\}\varphi_{\alpha} \\
& +\left(\frac{1}{2}+\frac{\kappa_3}{3!}\frac{\Phi}{M}+\frac{\kappa_4}{4!}\frac{\Phi^2}{M^2}\right)\frac{m_s^2}{g_s^2}\Phi^2-\frac{\zeta_0}{4!}\frac{1}{g_v^2}W^4+\frac{1}{2g_s^2}\left(1+\alpha_1\frac{\Phi}{M}\right)(\boldsymbol{\nabla}\Phi)^2 \\
& -\frac{1}{2g_v^2}\left(1+\alpha_2\frac{\Phi}{M}\right)(\boldsymbol{\nabla}W)^2-\frac{1}{2}\left(1+\eta_1\frac{\Phi}{M}+\frac{\eta_2}{2}\frac{\Phi^2}{M^2}\right)\frac{{m_v}^2}{{g_v}^2}W^2-\frac{1}{2g_\rho^2}(\boldsymbol{\nabla}R)^2 \\
& -\frac{1}{2}\left(1+\eta_\rho\frac{\Phi}{M}\right)\frac{m_\rho^2}{g_\rho^2}R^2-\frac{1}{2e^2}(\boldsymbol{\nabla}A)^2+\frac{1}{3g_\gamma g_v}A\Delta W+\frac{1}{g_\gamma g_\rho}A\Delta R. \qquad (2.23)
\end{aligned}
$$

The Dirac Hamiltonian for finite nuclei can be written as [109]

$$
\begin{aligned}
\mathcal{H}(\mathbf{r}) &= -\mathbf{i}\boldsymbol{\alpha}\cdot\boldsymbol{\nabla}+\mathbf{W}(\mathbf{r})+\frac{\mathbf{1}}{\mathbf{2}}\boldsymbol{\tau_3}\mathbf{R}+\beta(\mathbf{M}-\boldsymbol{\Phi}(\mathbf{r})) \\
&+\frac{1+\tau_3}{2}A(r)-\frac{i}{2M}\beta\boldsymbol{\alpha}\cdot\Big(f_v\boldsymbol{\nabla}W+\frac{1}{2}f_\rho\tau_3\boldsymbol{\nabla}R+\Big) \\
&+\frac{1}{2M^2}\left(\beta_s+\beta_v\tau_3\right)\Delta A-\frac{i}{2M}\lambda\beta\boldsymbol{\alpha}\cdot\nabla A, \qquad (2.24)
\end{aligned}
$$

where $W(r)\equiv g_v V_0(\mathbf{r})$, $\Phi(r)\equiv g_s\phi_0(\mathbf{r})$, $R\equiv g_\rho b_0(\mathbf{r})$ and $A\equiv eA_0(\mathbf{r})$ are the scalar mean fields with couplings [110]. $\beta=\gamma_0$ and $\alpha=\gamma_0\,\gamma$ are the Dirac matrices. The terms with g_γ, λ, β_s and β_v take care of the effects related with the electromagnetic structure of the pion and the nucleon (see Ref. [108]). Specifically, the constant g_γ concerns the coupling of the photon to the pions and the nucleons through the exchange of neutral vector mesons. The experimental value is $g_\gamma^2/4\pi=2.0$. The constant λ is needed to reproduce the magnetic moments of the nucleons, defined by

$$
\lambda=\frac{1}{2}\lambda_p(1+\tau_3)+\frac{1}{2}\lambda_n(1-\tau_3), \qquad (2.25)
$$

with $\lambda_p = 1.793$ and $\lambda_n = -1.913$, the anomalous magnetic moments of the proton and the neutron, respectively. The terms with β_s and β_v contribute to the charge radii of the nucleon [108]. The Dirac equation with single particle Hamiltonian h_α, the eigenvalues E_α and eigen functions $\psi_\alpha(r)$ is [36, 111]

$$h_\alpha \psi_\alpha(r) = E_\alpha \psi_\alpha(r), \tag{2.26}$$

with the normalisation condition,

$$\int d^3r \psi_\alpha^\dagger(r)\psi_\alpha(r) = 1. \tag{2.27}$$

The eigen functions for spherically symmetric nuclei is given by

$$\psi_\alpha(r) = \psi_{nkmt} = \begin{pmatrix} \frac{i}{r}G_a(r)\phi_{km} \\ -\frac{1}{r}F_a(r)\phi_{-km} \end{pmatrix}, \tag{2.28}$$

where G and F are the upper and lower component of the wave function $\psi_\alpha(r)$ respectively. Moreover, ϕ_{km} is a spin harmonic term, t = 1/2 for protons and t = -1/2 for neutrons. The radial equations for G and F become,

$$(\frac{d}{dr} + \frac{k}{r})G_a(r) - [E_a - U_1(r) + U_2(r)]F_a(r) - U_3 G_(r) = 0, \tag{2.29}$$

$$(\frac{d}{dr} - \frac{k}{r})F_a(r) + [E_a - U_1(r) - U_2(r)]G_a(r) + U_3 F_a(r) = 0, \tag{2.30}$$

where $U_1(r)$, $U_2(r)$, $U_3(r)$, are the single particle potentials and they defined as

$$U_1(r) = W(r) + t_a R(r) + (t_a + \frac{1}{2})A(r) + \frac{1}{2M^2}(\beta_s + 2t_a\beta_v)\nabla^2 A(r), \tag{2.31}$$

$$U_2(r) = M - \phi(r), \tag{2.32}$$

$$U_3(r) = \frac{1}{2M}\left\{ f_v W'(r) + t_a f_\rho R'(r) + A'(r)[(\lambda_p + \lambda_n)/2 + t_a(\lambda_p - \lambda_n)] \right\}, \tag{2.33}$$

here the prime denotes a radial derivative.

The mean field equations for ϕ, W, R and A are given by

$$-\nabla^2\phi + m_s^2\phi = g_s^2\rho_s(r) - \left(\frac{\kappa_3}{2} + \frac{\kappa_4}{3!}\frac{\Phi}{M}\right)\frac{m_s^2\Phi^2}{M} + \frac{\eta_\rho}{2M}\frac{g_s^2}{g_\rho^2}m_\rho^2 R^2 + \frac{\alpha_2}{2M}\frac{g_s^2}{g_v^2}(\nabla W)^2$$
$$+ \frac{g_s^2}{2M}\left(\eta_1 + \eta_2\frac{\phi}{M}\right)\frac{m_v^2}{g_v^2}W^2 + \frac{\alpha_1}{2M}[(\nabla\phi)^2 + 2\phi\nabla^2\phi] \tag{2.34}$$

$$-\nabla^2 W + m_v^2 W = g_v^2\left(\rho_s(r) + \frac{f_v}{2}\rho_T(r)\right) - \frac{\phi}{M}m_v^2 W\left(\eta_1 + \frac{\eta_2}{2}\frac{\phi}{M}\right)$$
$$-\frac{1}{3!}\zeta_0 W^3 + \frac{\alpha_2}{M}\left(\nabla\phi\cdot\nabla W + \phi\nabla^2 W\right), \tag{2.35}$$

$$-\nabla^2 R + m_\rho^2 R = \frac{1}{2}g_\rho^2\left(\rho_3(r) + \frac{f_\rho}{2}\rho_{T,3}(r)\right) - \eta_\rho\frac{\phi}{M}m_\rho^2 R, \tag{2.36}$$

$$-\nabla^2 A = e^2\rho_p(r). \tag{2.37}$$

The baryon, scalar, isovector, proton and tensor densities are

$$\rho(r) \;=\; \sum_\alpha \varphi_\alpha^\dagger(r)\varphi_\alpha(r)\,, \tag{2.38}$$

$$\rho_s(r) = \sum_\alpha \varphi_\alpha^\dagger(r)\beta\varphi_\alpha(r)\,, \tag{2.39}$$

$$\rho_3(r) = \sum_\alpha \varphi_\alpha^\dagger(r)\tau_3\varphi_\alpha(r)\,, \tag{2.40}$$

$$\rho_{\rm p}(r) = \sum_\alpha \varphi_\alpha^\dagger(r)\left(\frac{1+\tau_3}{2}\right)\varphi_\alpha(r)\,, \tag{2.41}$$

$$\rho_{\rm T}(r) = \sum_\alpha \frac{i}{M}\boldsymbol{\nabla}\cdot\left[\varphi_\alpha^\dagger(r)\beta\boldsymbol{\alpha}\varphi_\alpha(r)\right]\,, \tag{2.42}$$

$$\rho_{\rm T,3}(r) = \sum_\alpha \frac{i}{M}\boldsymbol{\nabla}\cdot\left[\varphi_\alpha^\dagger(r)\beta\boldsymbol{\alpha}\tau_3\varphi_\alpha(r)\right]\,. \tag{2.43}$$

These densities are obtained from the RMF and E-RMF formalisms with NL3 [112] and G2 [108, 113, 114, 115] parameterizations.

The energy density contains tensor couplings, and scalar-vector and vector-vector meson interactions, in addition to the standard scalar self interactions κ_3 and κ_4. Thus, the E-RMF formalism can be interpreted as a covariant formulation of density functional theory as it contains all the higher order terms in the Lagrangian, obtained by expanding it in powers of the meson fields. The terms in the Lagrangian are kept finite by adjusting the parameters. Further insight into the concepts of the E-RMF model can be obtained from Ref. [108]. It may be noted that the standard RMF Lagrangian is obtained from that of the E-RMF by ignoring the vector-vector and scalar-vector cross interactions, and hence does not need a separate discussion.

2.6 Pairing and Blocking Approximation

Pairing correlations have an important effect in low-energy nuclear phenomena. These correlations are essential for the correct description of nuclear structure effects in both the open-shell and deformed nuclei. It is shown experimentally [116] that pairing is

essential for stability of drip-line nuclei. The mean-field formalism only incorporate long-range pairing correlations of the nucleon-nucleon interaction. The BCS-pairing approach is reasonably valid for nuclei in the valley of stability-line. However, near the proton or neutron drip-line, the coupling to the continuum becomes important. It is also known that the BCS-pairing prescription breaks down when coupling between the bound and the continuum states takes place [5]. Furthermore, the effects of pairing are known to be considerably small [117] for odd-even (even-odd) or odd-odd systems, which is the case for the present investigation.

(i) Pairing by constant force

The pairing interaction is an attractive force that occurs between identical nucleons in one state j to $J^\pi = 0^+$ and also in different states j and j'. The effect of pairing distributes the nucleons to another orbit. Far below the Fermi surface, Pauli principle forbids such distribution (breaking of pairs) to take place. This is how it is possible to consider independent particle motion in the nucleus. However, near the Fermi surface where there is some probability that orbits are not occupied, this distribution can take place, which causes the smearing of Fermi surface. The smearing of surface leads to the concept of quasi-particle state which can be taken as the linear combination of hole and particle wave functions.

It is evident that RMF model includes no pairing correlations in the Lagrangian (2.21) which contains only the single-particle field operators in terms of $\psi^\dagger\psi$. The pairing correlations can only be described in a generalized single-particle theory by field operators $\psi^\dagger\psi^\dagger$ or $\psi\psi$ and two-body interaction of the type $\psi^\dagger\psi^\dagger\psi\psi$ on the classical level, with a violation of particle number. Such terms are not there in the Lagrangian. The pairing correlations are, therefore, often included in a phenomenological way within the simple BCS [41] approximation. For known nuclei, close to or not too far from the stability line, the BCS approach provides a reasonably good

description of the pairing properties. However, in going to nuclei in the vicinity of the drip-lines or to the super-heavy region, the coupling to the continuum becomes important. It has been shown that the self-consistent treatment of the BCS approximation does not provide the correct description of the coupling between bound and continuum states in dripline nuclei because of Fermi level falls near the particle continuum [5]. However, the pairing correlation will be considered in the BCS approach [118, 119] for a broad range of nuclei by assuming that the pairing interaction has non zero matrix elements only between pair of nucleons invariant under time reversal:

$$< \alpha_2\alpha_2|v_{pair}|\alpha_1\alpha_1 >= -G, \tag{2.44}$$

where $|\alpha_1 > = |nljm >$ and $|\alpha_2 > = |nlj - m >$ and G is the pairing strength.

The contribution of the pairing interaction to the total energy for each kind of nucleon is

$$E_{pair} = \sum_q -G_q \left\{ \sum_{\alpha_q>0} [\eta_{\alpha_q}(1-\eta_{\alpha_q})]^{1/2} \right\}^2 - G_q \sum_{\alpha_q>0} \eta^2_{\alpha_q}, \tag{2.45}$$

where η_{α_q} is the occupation probability of a state with quantum numbers $\alpha_q = (nljm)_q$ and q stands for each kind of nucleon.

$$\eta_{\alpha_q} = \frac{1}{2}\left[1 - \frac{\epsilon_{\alpha_q} - \mu_q}{\sqrt{(\epsilon_{\alpha_q} - \mu_q)^2 + \Delta_q^2}}\right]. \tag{2.46}$$

Pairing gap Δ_q is defined by

$$\Delta_q = G_q \sum_{\alpha_q} \left[\eta_{\alpha_q}(1-\eta_{\alpha_q})\right]^{1/2}. \tag{2.47}$$

Assuming constant pairing matrix elements in the vicinity of the Fermi level we can express Δ_q in terms of number of neutrons or protons involved in the pairing correlation A_q. The pairing energy for each kind of nucleon is written as

$$E_{pair} = \sum_q \frac{\Delta_q^2}{G_q}. \tag{2.48}$$

This approach is not suitable in case of nuclei far from stability line, which can be solved by taking into account continuum effects by means of the so-called quasi bound states [120, 121]. In this case, we consider a constant pairing matrix element G_q for each kind of nucleon and stimulate the zero range of the pairing force. These quasi-bound states mock up the effect of the continuum in the pairing calculation. To avoid the unrealistic pairing of highly excited states and to express the region of influence of the pairing potential to the vicinity of the Fermi level, the available space of α_q states to one harmonic oscillator shell above and below of the Fermi level. The solutions of the pairing equations are useful to find average pairing gap Δ_q for each kind of nucleon [122].

The wave functions of the quasi-bound levels are localised in the classically allowed region and decrease exponentially outside it. This eliminates nucleon gas from the surrounding of the nucleus if continuum levels are included. This method is able to predict the behaviour of the neutron and charge radii far from stability line [123].

(ii) Pairing by constant gap

We have chosen the BCS-formalism with a constant pairing strength [124]: $\Delta_p = RB_s e^{sI-tI^2}/Z^{1/3}$ and $\Delta_n = RB_s e^{-sI-tI^2}/A^{1/3}$ with R=5.72, s=0.118, t= 8.12, B_s=1, and $I = (N-Z)/(N+Z)$. This type of prescription for pairing effects, both in RMF and SHF, has already been used by us and many other authors [125, 126]. For this pairing approach, it is shown [125, 126, 127] that the results for binding energies and quadruple deformations are almost identical with the predictions of relativistic Hartree-Bogoliubov (RHB) approach.

(iii) Blocking

It is a tough task to compute the binding energy and quadrupole moment of odd-n or odd-p or both odd-p and odd-n (odd-even, even-odd or odd-odd) nuclei, both in RMF and SHF models in an axially deformed basis. To do this, one needs to include the additional time-odd term, as is done in the SHF Hamiltonian [96], or has to include empirically the pairing force in order to take care the effect of odd-n or odd-p [128]. In an odd-even or odd-odd nucleus, the time reversal symmetry gets violated in the mean field models. In our RMF calculations, the space component of the vector fields, which are odd under time reversal and parity, are neglected. These are important in the determination of magnetic moments [129], but have a very small effect on bulk properties like binding energies or quadrupole deformations, and can be neglected [130] in the present context. Here, for the odd-A calculations, we employ the blocking approximation, which restores the time-reversal symmetry. In this approach one pair of conjugate states, $\pm m$, is taken out from the pairing scheme. The odd particle stays in one of these states and its corresponding conjugate state remains empty. In principle, one has to block in turn different states around the Fermi level to find the one which gives the lowest energy configuration of the odd nucleus. For odd-odd nuclei, one needed to block both the odd neutron and odd proton. Similar procedure is carried for odd-A calculations in the SHF formalism. For details we refer the readers to see Ref. [125].

2.7 Numerical Method

To find solutions of the RMF equations, we use the finite basis expansion method [41] in which an axially deformed harmonic oscillator basis is used. The upper and lower components of the Dirac spinor and boson fields are expanded separately in this appropriate basis with an initial deformation. In the practical calculations we

truncate the basis after a finite value of oscillator quantum number N_{max} (N_F and N_B, F stands for Fermion and B stands for Boson), which is the quantum number of the major oscillator shell. In axial symmetry, the densities are invariant with respect to rotation around the symmetry axis (z-axis) but the rotational symmetry is broken; therefore, j is no longer a good quantum number. It is thus useful to use cylindrical co-ordinates:

$$x = r_{xy}cos\phi, \quad y = r_{xy}sin\phi \quad and \quad z. \tag{2.49}$$

The spinor ψ_i is characterized by the quantum numbers:

$$\Omega_i, \quad P_i, \quad t_i, \tag{2.50}$$

where $\Omega_i = m_{t_i} + m_{si}$ is the eigen value of symmetry operator J_P; P_i is parity and t_i is isospin. The spinor can be written in the form given by

$$\psi_i(r,t) = \begin{pmatrix} f_i(r) \\ ig_i(r) \end{pmatrix} = \frac{1}{\sqrt{2\pi}} \begin{pmatrix} f_i^+(z,r)\exp i(\Omega_i - 1/2)\phi(r) \\ f_i^-(z,r)\exp i(\Omega_i + 1/2)\phi(r) \\ ig_i^+(z,r)\exp i(\Omega_i - 1/2)\phi(r) \\ ig_i^-(z,r)\exp i(\Omega_i + 1/2)\phi(r) \end{pmatrix}. \tag{2.51}$$

We expand spinors $f_i^{\pm}$ and $g_i^{\pm}$ in the above equation in terms of the eigen functions of a deformed axially symmetric oscillator potential:

$$V_{osc}(z, r_\perp) = \frac{1}{2}M\omega_z^2 z^2 + \frac{1}{2}M\omega_\perp^2 r_\perp^2. \tag{2.52}$$

Taking the volume conservation into account, the two oscillator frequencies $\hbar\omega_\perp$ and $\hbar\omega_z$ can be expressed in terms of a deformation parameter β_0:

$$\hbar\omega_z = \hbar\omega_0 \exp(-\sqrt{\frac{5}{4\pi}}\beta_0) \tag{2.53}$$

$$\hbar\omega_\perp = \hbar\omega_0 \exp(+\frac{1}{2}\sqrt{\frac{5}{4\pi}}\beta_0). \tag{2.54}$$

The corresponding oscillator length parameters are:

$$b_z = \sqrt{\frac{\hbar}{M\omega_z}} \quad and \quad b_\perp = \sqrt{\frac{\hbar}{M\omega_\perp}}. \tag{2.55}$$

For the volume conservation, we have $b_\perp^2 b_z = b_0^3$. The four components $f^\pm(r,z)$ and $g^\pm(r,z)$ obey Dirac equation:

$$(M^* + V)f_i^+ + \partial_i g_z^+ + \Big(\partial_r + \tfrac{\Omega+\frac{1}{2}}{r}) \Big) g_i^- = \epsilon f_i^+ \tag{2.56}$$

$$(M^* + V)f_i^- - \partial_i g_z^+ + \Big(\partial_r - \tfrac{\Omega+\frac{1}{2}}{r}) \Big) g_i^- = \epsilon f_i^- \tag{2.57}$$

$$(M^* + V)g_i^+ + \partial_i g_z^+ + \Big(\partial_r + \tfrac{\Omega-\frac{1}{2}}{r}) \Big) g_i^- = -\epsilon f_i^+ \tag{2.58}$$

$$(M^* + V)g_i^- + \partial_i g_z^+ + \Big(\partial_r - \tfrac{\Omega+\frac{1}{2}}{r}) \Big) g_i^- = -\epsilon g_i^-. \tag{2.59}$$

The densities now become:

$$\rho_{s,v} = 2\sum_{i>0} v_i^2 \{(|f_i^+|^2 + |f_i^-|^2) \mp (|g_i^+|^2 + |g_i^-|^2)\} \tag{2.60}$$

$$\rho_{3,c} = 2\sum_{i>0} v_i^2 \{(|f_i^+|^2 + |f_i^-|^2) + (|g_i^+|^2 + |g_i^-|^2)\}. \tag{2.61}$$

These densities serve as sources for the fields ϕ=σ, ω, ρ and photon, which are determined by meson equations in cylindrical co-ordinates:

$$(-\frac{1}{r_\perp}\partial r_\perp r_\perp \partial r_\perp - \partial_z^2 + m_\phi^2)\phi(z, r_\perp) = s_\phi(z, r_\perp), \tag{2.62}$$

with the inhomogeneous part s_ϕ

$$s_\phi = \begin{cases} -g_\sigma \rho_s(z, r_\perp) - g_2\sigma^2(z, r_\perp) - g_3\sigma^3(z, r_\perp) \\ g_\omega \rho_v(z, r_\perp) - C_3 V^3(z, r_\perp) \\ g_\rho \rho_3(z, r_\perp) \\ e\rho_p(z, r_\perp) \end{cases} \tag{2.63}$$

The iteration procedure to solve RMF equations is as follows: (i) In the beginning we assume the values of meson fields V and S, (ii) using these fields we can solve the Dirac equation for spinors ψ_i, then various densities (2.60) and (2.61) are calculated using the spinors (2.51) which in turn give the source terms (2.63) in the meson equations, (iii) the solution of meson equations used to calculate the potentials and effective mass M*. These new potentials and M* are further used in the Dirac equation for the next iteration. This process continues till the convergence is achieved to the desired accuracy. Thus, the self-consistent solution of RMF equations yields the nucleon spinors (ψ_i), meson and electromagnetic fields (σ, ω, ρ, A), total binding energy (E), single-particle energies, point-neutron and proton densities. The different energy expressions in equation (2.67) are given below:

$$\begin{aligned} E_{part} &= \sum_{i=1}^{A} v_i^2 \int d^3r \psi_i^\dagger \{-i\vec{\alpha}.\vec{\nabla} + \beta M^* + V\}\psi_i \\ &= \sum_{i}^{A} v_i^2 \epsilon_i \end{aligned} \tag{2.64}$$

$$\begin{aligned} E_\sigma &= \int d^3r \{\frac{1}{2}(\nabla\sigma)^2 + U\sigma\} \\ E_\omega &= -\int d^3r \frac{1}{2}\{(\nabla V_0)^2 + m_\omega^2 V_0^2\} \\ E_\rho &= -\int d^3r \frac{1}{2}\{(\nabla \rho_0)^2 + m_\rho^2 \rho_0^2\} \\ E_c &= -\int d^3r \frac{1}{2}(\nabla A_0)^2 \end{aligned} \tag{2.65}$$

$$\begin{aligned} E_{CM} &= -\frac{3}{4}\hbar\omega_0 = -\frac{3}{4}41A^{-\frac{1}{3}} \\ E_{pair} &= -G(\sum_{i=1}^{A} u_i v_i)^2. \end{aligned} \tag{2.66}$$

Finally, the total binding energy (-E_{total}) is calculated by summing the contribution of energy, mesons and photon energies,

$$E_{tot} = E_{part} + E_{\sigma} + E_{\omega} + E_{\rho} + E_{pair} + E_{C.M} + E_c \tag{2.67}$$

From these quantities we can calculate point-neutron/proton radii ($r_{n/p}$), charge radii r_c, charge densities ρ_c, nucleon separation energies, quadrupole moments and deformation parameter (β_2), etc. The radii $r_{n/p}$ are calculated using the expression:

$$\langle r^2_{n/p} \rangle = \sum_{i=1}^{N(Z)} n_i \overline{\psi}_i(r) r^2 \psi_i(r). \tag{2.68}$$

The root mean square radius is given by

$$r_{rms} = \left(\frac{N r_n^2 + Z r_p^2}{N + Z} \right). \tag{2.69}$$

The charge radius is given by

$$r_c = \sqrt{r_p^2 + 0.64}, \tag{2.70}$$

where the size of proton is taken to be 0.8 fm.

The charge densities are obtained by folding the calculated point proton densities with proton charge distribution. The proton charge distribution is taken to be a Gaussian. The folded densities are:

$$\rho_c(r) = \int d^3r\prime \frac{1}{\sqrt{(2\pi\sigma)^3}} exp(-\frac{(r - r\prime)^2}{2\sigma^2}) \rho_p(r\prime). \tag{2.71}$$

The quadrupole (hexadecupole) moments $Q_{n/p}$ ($H_{n/p}$) for neutrons/protons are calculated by using the following operator expressions:

$$Q_{n/p} = \langle 2r^2 P_2(cos\theta) \rangle = \langle 2z^2 - x^2 - y^2 \rangle_{n/p}. \tag{2.72}$$

$$H_{n/p} = \langle r^4 Y_{40}(\theta) \rangle = \sqrt{\frac{9}{64\pi}} \langle 8z^4 - 24z^2(x^2+y^2) + 3(x^2+y^2)^2 \rangle_{n/p}. \quad (2.73)$$

The deformation parameter β_2 is calculated from the quadrupole moment for neutron/proton using the relation:

$$Q = Q_n + Q_p = \sqrt{\frac{16\pi}{5}} \frac{3}{4\pi} A R_0^2 \beta_2. \quad (2.74)$$

The neutron (S_n, S_{2n}) and proton (S_p, S_{2p}) separation energies are calculated by using the expression:

$$S_n = BE(N,Z) - BE(N-1,Z) \qquad S_p = BE(N,Z) - BE(N,Z-1) \quad (2.75)$$

$$S_{2n} = BE(N,Z) - BE(N-2,Z) \qquad S_{2p} = BE(N,Z) - BE(N,Z-2) \quad (2.76)$$

The RMF force parameters and their matter properties are given in Table 2.3.

Table 2.3: Different parameter sets used in the relativistic formalism. Emp. represents the empirical values. The nuclear matter properties are shown in the lower panel of table.

parameter	NL3	NL3*	NL-SH	G2	Emp. Value
M(MeV)	939.0	939.0	939.0	939.0	938.0
m_σ(MeV)	508.194	502.574	526.059	520.300	
m_ω(MeV)	782.501	782.600	783.000	782.0	783±5
m_ρ(MeV)	763.000	763.000	763.000	770.0	773 ± 77
g_σ	10.217	10.094	10.444	10.824	
g_ω	12.868	12.807	12.945	12.963	
g_ρ	4.474	4.575	4.383	3.848	
g_2 (fm$^-$1)	-10.431	-10.809	-6.910	-7.157	
g_3	-28.885	-30.149	-15.834	-3.73	
Nuclear	Matter	Properties			
M*/M	0.60	0.594	0.60	0.634	0.65
a_{sym} (MeV)	37.4	38.6	36.1	36.9	36.1
K (MeV)	271.76	258.28	355.36	281	210± 30
ρ_0(fm$^-$3)	0.148	0.150	0.146	0.145	0.17
BE/A (MeV)	16.30	16.31	16.35	16.3	15.68

2.8 Glauber Model

The Glauber model was developed to address the quantum theory of collisions of composite particles. In 1950's, this was of great interest to physicists. This model provides systematic calculations considering the many-body nuclear system either as a projectile or target to study heavy-ion elastic scattering and reaction cross sections. The idea of this model is to express the nucleus as uncorrelated nucleons with measured density distributions. The main feature of the original Glauber calculations is the optical limit for any analytic and numerical calculations [131]. In this approach, geometric parameters calculation requires some experimental data like nuclear charge densities, inelastic nucleon-nucleon cross section as inputs. According to this model the collision of two nuclei can be expressed by individual interactions of the constituent nucleons. The sum over all possible two nucleon phase shift is the overall phase shift of the incoming wave in the optical limit. This model assumes that at high energies, nucleons carry sufficient momentum and remain undeflected as the nuclei pass through each other. This model views independent movement of nucleons in the nucleus and large nuclear size as compared to the depth of the nucleon-nucleon force. Simple analytic and numerical calculations for the nucleus-nucleus and nucleon-nucleon interaction cross sections are possible due to the hypothesis of independent trajectories of the constituent nucleons. In low energy range this model has been modified considering the deviation due to Coulomb field effect in the straight line trajectory of the colliding nuclei which is called Coulomb modified Glauber model [132].

2.8.1 Total nuclear reaction cross section

The theoretical formalism to calculate the total nuclear reaction cross section σ_r using Glauber approach has been given by R. J. Glauber [10]. It is a semi-classical

model picturing the nuclei moving in a straight path along the collision direction and is based on the independent, individual nucleon-nucleon (NN) collisions along the eikonal [133]. It has been used extensively to explain the observed total nuclear reaction cross sections for various systems at high energies.

The nuclear densities, obtained from the RMF or E-RMF models, are fitted to a sum of two Gaussian functions, with appropriate co-efficients c_i and ranges a_i chosen for the respective nuclei, as

$$\rho(r) = \sum_{i=1}^{N} c_i exp[-a_i r^2]. \tag{2.77}$$

Then, the Glauber model is used to calculate the total nuclear reaction cross section for both stable and unstable nuclei.

The standard Glauber form for the total nuclear reaction cross sections at high energies is expressed as [10, 134]:

$$\sigma_r = 2\pi \int_0^\infty b[1 - T(b)]db\,, \tag{2.78}$$

where $T(b)$ is the transparency function, the probability of the projectile to traverse the nucleus without interactions at centre of mass impact parameter b. The function $T(b)$ is calculated in the overlap region between the projectile and the target assuming that the interaction is formed from a single NN collision. It is given by

$$T(b) = \exp\left[-\sum_{i,j} \overline{\sigma}_{ij} \int d\vec{s}\,\overline{\rho}_{ti}(s)\,\overline{\rho}_{pj}\left(\left|\vec{b} - \vec{s}\right| s\right)\right]. \tag{2.79}$$

The summation indices i and j run over proton and nucleon and subscript p and t refers to projectile and target, respectively. The experimental nucleon-nucleon reaction cross section $\overline{\sigma}_{ij}$ varies with energy.

The z-integrated densities $\overline{\rho}(\omega)$ are defined by

$$\overline{\rho}(\omega) = \int_{-\infty}^{\infty} \rho\left(\sqrt{\omega^2 + z^2}\right) dz \,, \tag{2.80}$$

with $\omega^2 = x^2 + y^2$. The argument of $T(b)$ in Eq. (2.79) is $\left|\vec{b} - \vec{s}\right|$, which stands for the impact parameter between the i^{th} and j^{th} nucleons.

The original Glauber model was designed for high energy approximation. However, it was found to work reasonably well for both the nucleus-nucleus reaction and the differential elastic scattering cross sections over a broad energy range [135, 136]. To include the low energy effects of NN interaction, the Glauber model is modified to take care of the finite range effects in the profile function and Coulomb modified trajectories [133, 137]. The modified $T(b)$ is given by [133, 138],

$$T(b) = \exp\left[-\int_p \int_t \sum_{i,j} \left[\Gamma_{ij}\left(\vec{b} - \vec{s} + \vec{t}\right)\right] \overline{\rho}_{pi}\left(\vec{t}\right) \overline{\rho}_{tj}\left(\vec{s}\right) d\vec{s} d\vec{t}\right] . \tag{2.81}$$

The profile function $\Gamma_{ij}(b_{eff})$ is defined as [133, 137, 138]

$$\Gamma_{ij}(b_{eff}) = \frac{1 - i\alpha_{NN}}{2\pi\beta_{NN}^2} \sigma_{ij} \exp\left(-\frac{b_{eff}^2}{2\beta_{NN}^2}\right) , \tag{2.82}$$

with $b_{eff} = \left|\vec{b} - \vec{s} + \vec{t}\right|$, $\vec{b}$ is the impact parameter, $\vec{s}$ and $\vec{t}$ are the dummy variables for integration over the z-integrated target and projectile densities. The parameters σ_{NN}, α_{NN}, and β_{NN} are usually case-dependent (proton-proton, neutron-neutron or proton-neutron), but we have used the appropriate average values from Refs. [134, 139, 140, 141, 142]. It is worth mentioning that the result in Glauber model is sensitive to the in-medium NN cross section with proper treatment of the input densities [143] and also depends on the accuracy of the profile function.

b_c = Distance of closest approach is related to the impact parameter b as

$$b_c = \frac{1}{k}\left(\eta + \sqrt{\eta^2 + k^2 b^2}\right) \tag{2.83}$$

$$\eta = \frac{Z_P Z_T e^2}{\hbar v}, \tag{2.84}$$

k and η are the projectile wave number and the Sommerfeld parameter, respectively. The relative velocity of the two nuclei is v. The range parameter β_{NN} is given by

$$\beta_{NN} = 0.996 exp\left[\frac{-E}{106.679}\right] + 0.089, \tag{2.85}$$

where E is the projectile energy.

2.8.2 Differential elastic scattering cross section

The differential elastic scattering cross section, in terms of the Rutherford cross section is given by,

$$\frac{d\sigma}{d\Omega} = \frac{|F(\mathbf{q})|^2}{|F_{coul}(\mathbf{q})|^2}\,. \tag{2.86}$$

$F(q)$ and $F_{coul}(\mathbf{q})$ are the elastic and Coulomb (elastic) scattering amplitudes, respectively.

The elastic scattering amplitude $F(\mathbf{q})$ is written as

$$F(\mathbf{q}) = e^{i\chi_s}\left\{F_{coul}(\mathbf{q}) + \frac{iK}{2\pi}\int dbe^{-iq.b+2i\eta\ ln(Kb)}T(b)\right\}, \tag{2.87}$$

with the Coulomb elastic scattering amplitude $F_{coul}(\mathbf{q})$ given as

$$F_{coul}(\mathbf{q}) = \frac{-2\eta K}{q^2}\exp\left\{-2i\eta\ ln\left(\frac{q}{2K}\right) + 2i\arg\Gamma\left(1+i\eta\right)\right\}\,. \tag{2.88}$$

Here η=$Z_P Z_T e^2/\hbar v$ is the Sommerfeld parameter, v the incident velocity, and $\chi_s = -2\eta \ln(2Ka)$ with a being the screening radius [10]. The differential elastic cross section does not depend on the screening radius a.

2.8.3 One nucleon removal cross section

The expression for one nucleon removal reaction cross section $\sigma_{-1n}(I)$ is given by [133]

$$\sigma_{-1n}(I) = \sum_c \int d\vec{k}\, \sigma_{a=(k,g=0),c}, \tag{2.89}$$

where $\sigma_{a=(k,g=0),c}$ are the possible final states ac. In the present formalism, it is considered that the projectile nucleus breaks up into a core and the removed nucleon. The core c has an internal wave function ϕ_g and the one-nucleon, i.e., the departed nucleon has an asymptotic momentum $\hbar\mathbf{k}$ in the continuum state with respect to the core. The core is considered to be in the ground state ($g = 0$) at the time of the collision. The total $\sigma_{-1n}(I)$ can be separated to an elastic (σ^{el}_{-1n}) with $c = 0$ and inelastic (σ^{iel}_{-1n}) part having c as non-zero. The σ^{el}_{-1n} and σ^{iel}_{-1n} are expressed as [133]

$$\begin{aligned}\sigma^{el}_{-1n}(I) &= \int d\mathbf{b}\{< \phi_0 \mid e^{-2Im\chi_{Ct}(b_C)-2Im\chi_{-1nt}(b_C+s)} \mid \phi_0 > \\ &\quad - |< \phi_0 \mid e^{-i\chi_{Ct}(b_C)+i\chi_{-1nt}(b_C+s)} \mid \phi_0 >|^2\}\end{aligned} \tag{2.90}$$

$$\begin{aligned}\sigma^{iel}_{-1n}(I) &= \int d\mathbf{b}\{< \phi_0 \mid e^{-2Im\chi_{Ct}(b_C)} \\ &\quad - e^{-2Im\chi_{Ct}(b_C)-2Im\chi_{-1nt}(b_C+s)} \mid \phi_0 >\},\end{aligned} \tag{2.91}$$

here χ_{pt} is the phase shift function and ϕ_0 is the valence wave function (the wave function of the removed nucleon). The notation and the numerical procedure of calculation of one-nucleon removal reaction cross section are followed from Ref. [133].

2.9 Coupled Channel Formalism

To compute the fusion cross section σ_f we follow the coupled-channel calculations including all orders of coupling. This is done in a non-relativistic framework. The computer code CCFULL as developed in Ref. [144] is used. The program CCFUL includes the couplings to full order and there is no expansion of coupling potential. In this program the dimension of the coupled-channel equations is too large and hence the program is developed with no-Coriolis approximation or isocentral approximation [145]. This approximation work well for heavy ion fusion reactions. The Coupled-channel equations with Coriolis approximation is read as

$$\left[\frac{h^2}{2\phi}\frac{d^2}{dr^2} + \frac{J(J+1)h^2}{2\phi^2} + V_N^{(0)}(r) + \frac{Z_p Z_T e^2}{r} + \epsilon_n - E\right]\psi_n(r) + \sum_m V_{nm}(r)\psi_m(r) = 0 \quad (2.92)$$

where r is the radial component of the coordinate of the relative motion, μ is the reduced mass, E is the bombarding energy in the centre of mass frame and ϵ_n is the excitation energy. V_{nm} are the matrix elements of the coupling Hamiltonian and $V_N^{(0)}$ is the nuclear potential in the entrance channel.

The Wood-Saxon parametrization used in the program for the nuclear potential $V_N^{(0)}$ is

$$V_N^{(0)}(r) = \frac{V_0}{1 + exp((r - R_0)/a)}, R_0 = r_0(A_P^{1/3} + A_T^{1/3}). \quad (2.93)$$

The coupled-channel equations are solved by imposing the boundary conditions and considering only incoming waves at r = r_{min} , only outgoing waves at infinity for all channels except the entrance channel (n=0). This boundary conditions are referred as the incoming wave boundary conditions (IWBC) [146], which is valid only for heavy-ion reactions. The program adopts the minimum position of the Coulomb pocket inside the barrier for r_{min}. The boundary conditions are expressed as

$$\psi_n(r) \longrightarrow T_n exp\left(-i\int k_n(r')dr'\right), r = r_{min}, \tag{2.94}$$

$$\psi_n(r) \longrightarrow H_J^{(-)}(K_n(r))\partial_{n,0} + R_n H_J^{(+)}(k_n r), r = r_{max}. \tag{2.95}$$

Where

$$k_n(r) = \sqrt{\frac{2\mu}{h^2}\left(E - \epsilon_n - \frac{J(J+1)h^2}{2\mu r^2} - V_N(r) - \frac{Z_p Z_T e^2}{r} - V_{nm}(r)\right)} \tag{2.96}$$

is the local wave number for the nth channel. $H_J^{(-)}$ and $H_J^{(+)}$ are the incoming and the outgoing Coulomb functions, respectively.

To ensure that there are only incoming waves at r$\longrightarrow r_{min}$, coupled channel equations are solved first outwards from r_{min} by setting

$$\psi_n(r_{min}) = 1, \psi_m(r_{min}) = 0(m = n) \tag{2.97}$$

$$\frac{d}{dr}\psi_n(r_{min}) = -ik_n(r_{min}), \frac{d}{dr}\psi_m(r_{min}) = 0(m = n) \tag{2.98}$$

The solution of the coupled channel equations with the boundary conditions (2.94) and (2.95) is represented by a linear combination of χ_{nm} as

$$\psi_m(r) = \sum_n T_n \chi_{nm}(r). \tag{2.99}$$

$$\psi_m(r_{max}) = \sum_n T_n \chi_{nm}(r_{max}) = \sum_n T_n \left(C_{nm} H_J^{(-)}(k_m r_{max}) + D_{nm} H_J^{(+)}(k_m r_{max})\right) \tag{2.100}$$

Comparing Eqs. (2.95) and (2.100)

$$\sum_n T_n C_{nm} = \partial_{m,0} \tag{2.101}$$

Finally the transmission coefficients are obtained using

$$T_n = (C^{-1})_{n0}. \tag{2.102}$$

The fusion cross section is given by the formula [144]:

$$\sigma_f(E) = \sum_J \sigma_J(E) = \frac{\pi}{k_0^2} \sum_J (2J+1) P_J(E), \tag{2.103}$$

Where

$$P_J(E) = \sum_n \frac{k_n (r_{min}}{k_0} T_n^2. \tag{2.104}$$

is the inclusive penetrability [144].

Chapter 3

Nuclear structure: Ground States and Intrinsic Excited States

3.1 Introduction

It is a remarkable fact of nuclear structure that, there is a stable combination of protons and neutrons for every value of A from Hydrogen to Bismuth. For example, ^{6}Li is most stable from all the isotopes of Li. Similarly ^{56}Fe is most stable on the periodic table. All nuclei remain in the stable configuration forever unless subjected to strong external force. For any combination of Z and N there exists ground and various possible excited states but nuclei remain in such excited states for short periods and immediately decay to one stable configuration of Z and N [15]. There are another 2000+ isotopes including the recently discovered Z = 118 with unstable Z and N ratios having significant half-lives. These isotopes emit radiation and settle into a different ratio of protons and neutrons on the way toward stability (as shown in Fig. 1.1 of Chapter 1). Thus the significance of nuclear structure theory is that, for any combination of Z and N, there exist on stable configuration. In contrast, majority of excited states decay to the ground-state in a few seconds. However, either the ground state is stable or the transition to a different isotope with a more favorable Z and N ratio occurs quite slowly. In this context, the ground and intrinsic excited states are

important to collect information on nuclear configurations. Significant progress in the secondary radioactive beam technology allow us to study the unexplored regions, particularly the structures and properties of isotopes near and far away from $\beta-$ stability [114, 147, 148, 149]. These new developments extend our understanding of nuclear structure considerably including spin, isospin, momenta, nuclear size, density distribution etc. In this Chapter, we will discuss both ground and first excited intrinsic state for *spherical* nuclei in order to test [150] the validity of model parameters used in, say, the mean field approaches applied to nuclei far away from the valley of β-stability.

(a) Ground States of Finite Nuclei

The microscopic description of the ground state properties of finite nuclei has so far been possible on the phenomenological level. The most successful theories of this type are the conventional Hartree-Fock calculations with effective density dependent interactions (DDHF), which are understood as a phenomenological parameterization of the G-matrix. The forces of the type in Ref. [25] and Gogny forces [151] are the best known examples. The Relativistic Mean Field Theory (RMF) [29, 30, 41] is another approach for the microscopic description of nuclei. One of the success of these theories, is that these are not only able to reproduce the densities and binding energies for the finite nuclear matter but also yield spin-orbit interaction automatically in nuclei. Although, the results of the non-relativistic DDHF calculations using Skyrme forces are equally good but the RMF results are found to have a slight edge over their non-relativistic counterparts [41]. The RMF model used here, [29, 30, 41] is quite successful in describing the nuclear matter and finite nuclei. This model provides the internal structure or sub-structure information of the nuclei through the density distributions, using as an input not only for nuclei near the valley of stability, but also far away from the $\beta-$ stability line [47]. RMF theory has also achieved a great success in providing an unified and excellent description of the binding energies, deformation

parameters etc. of nuclei through out the periodic table including exotic nuclei. On the other hand, the recently developed E-RMF formalism reproduces the properties of finite nuclei as good as RMF model, with an additional success of describing the properties of nuclear matter, including the properties of astrophysical objects like neutron star [114, 123, 147, 149]. In standard RMF, with NL3 parameter set, the nuclear matter compressibility $K_\infty \sim 271.5$ MeV [112], which is slightly more than the empirical value of $K_\infty = 210 \pm 30$ MeV [152]. It is around 215 MeV [114, 147] in E-RMF formalism, which is closer to the data.

(b) Intrinsic Excited States of Finite Nuclei

The nuclei from $Z = N = 20$ to $Z = N = 28$ are well described by the shell model. These nuclei have the shell model configuration $(f_{7/2})^{n-r}(f_{5/2}p_{3/2}p_{1/2})^r$, where $r = 0, 1, 2, \ldots$. However, the energy spacings of these fp–shell nuclei follow some what irregular level spacings at the high spin states [153]. These may be the signatures of a level crossing with back-bending, i.e., the disappearance of collective properties and reappearing of the single-particle nature of these nuclei. Another feature of the semi-magic or double-magic nuclei is the spherical-deformed shape co-existence. The spherical shape is formed by the closed shell configuration, whereas the deformed state evolves by breaking the magic shell. The spherical-deformed shape co-existence has been observed for ^{56}Ni [154] and is also suggested theoretically by Mizusaki *et al.* [155]. In a recent publication [156], it is reported that ^{53}Co has an isomeric $3/2^-$ state, which motivated us to perform the present work of studying the low-lying isomeric state in ^{53}Co, and its mirror nucleus ^{53}Fe, on the basis of the relativistic and non-relativistic mean field formalisms [157].

First of all we study the total density ρ, proton density ρ_p and neutron density ρ_n distributions for some light, medium and heavy nuclei. We discuss the similarities and

differences on density distributions in different nuclei for NL3 and G2 parameter sets. The relative isotopic proton and neutron density differences $\Delta\rho_p(r)$ and $\Delta\rho_n(r)$ for Ca isotopes are also discussed. Then we calculate the bulk properties, such as binding energy (BE), root mean square charge radius r_{ch}, matter radius r_m and quadrupole deformation parameter β_2 for light, medium and heavy nuclei in the ground as well as in intrinsic excited or isomeric state using SHF, RMF and E-RMF formalisms. Potential energy surface (PES) and single particle energy separation in the isomeric states for ^{53}Fe and ^{53}Co are also discussed. We have done extensive calculations for nuclei over a large range of atomic mass and charge. The calculated results are compared with the experimental data wherever available in Tables. It is clear that our results agree remarkably well with the data.

3.2 Results and Discussion

There exist a number of parameter sets for solving the standard SHF Hamiltonians, RMF and E-RMF Lagrangian. In some of our previous work and of other authors [41, 112, 158, 159, 160] the ground state properties, like the binding energies (BE), charge radii (r_c), quadrupole deformation parameters (β_2) and other bulk properties are evaluated by using the various non-relativistic and relativistic parameter sets. It is found that, more or less, most of the recent parameters reproduce well the ground state properties, not only of stable normal nuclei but also of exotic nuclei which are far away from the valley of $\beta-$stability. This means that if one uses a reasonably acceptable parameter set, the predictions of the model will remain nearly force independent. To get structure information we employ three types of density distributions: SHF, RMF and E-RMF theory. Several set of parameters like SKI4, SLy6, NL-SH, NL3, NL3*, G2 are used for this purpose. We have solved a set of coupled equations for nucleons and mesons using these parameter sets.

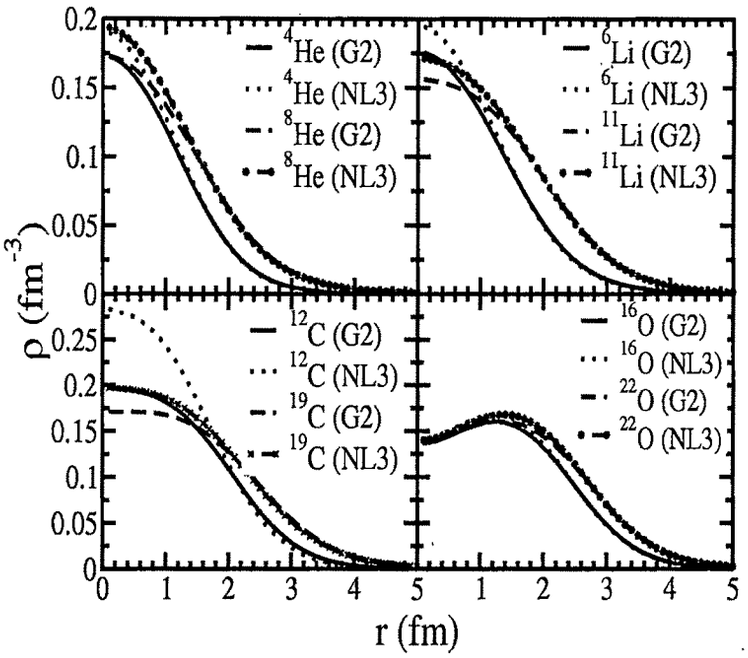

Figure 3.1: The ground state densities for some light nuclei obtained from the RMF(NL3) and E-RMF(G2) formalisms.

3.2.1 Nuclear Density

The ingredient to calculate the nuclear observable is the nuclear density. Hence, it becomes important to select the appropriate density before finding the ground state observable. These are the most crucial and required quantities for our calculations of the bulk properties as well as nuclear cross sections. We have shown spherical nuclear density distribution in Figs. 3.1, 3.2 and 3.3 using both RMF(NL3) and E-RMF(G2) parameter sets. Fig. 3.1 depicts the densities for some representative light nuclei, Figs. 3.2 and 3.3 for medium and heavy nuclei.

We notice from Fig. 3.1, that the nuclear densities for RMF(NL3) and E-RMF(G2) for lighter nuclei are considerably different near the centre of the nucleus. This difference reduces as we go away from the middle of the nuclei towards the surface. As expected, the density distribution is elongated for neutron-rich nuclei, as compared

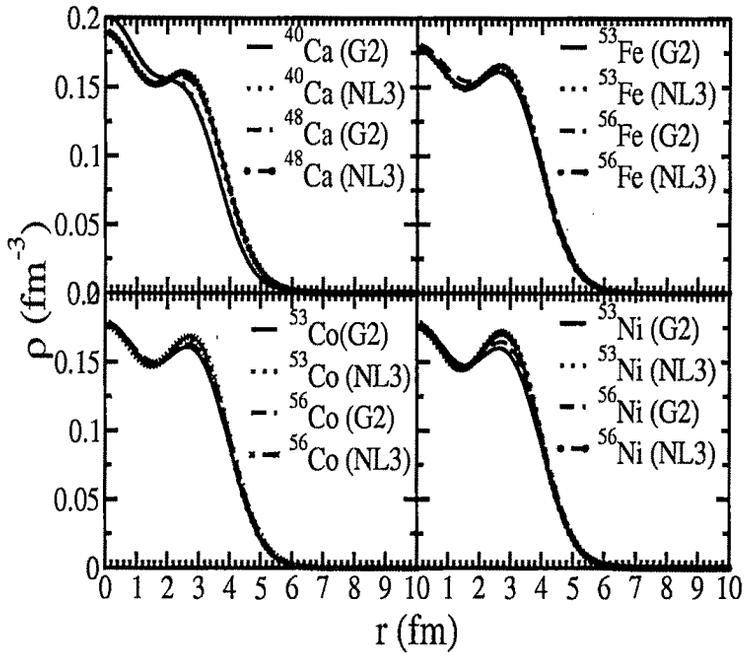

Figure 3.2: Same as Fig. 3.1, but for some nuclei in medium mass region.

to the stable isotopes. All the pairs of nuclei (^{4}He, ^{8}He), (^{6}Li, ^{11}Li), (^{12}C, ^{19}C), and (^{16}O, ^{22}O) shown here present the same features for the light mass region.

Similarly, in Fig. 3.2, we have shown the spherical density distributions for pairs of nuclei (^{40}Ca, ^{48}Ca), (^{53}Co, ^{56}Co), (^{53}Fe, ^{56}Fe), and (^{53}Ni, ^{56}Ni) in medium mass region. In heavy region we have plotted for pairs (^{208}Pb, ^{248}Pb), (^{235}U, ^{250}U), (^{230}Th, ^{260}Th), and the recently, discovered, superheavy $^{298}X_{120}$ and its neutron-rich isotope $^{302}X_{120}$. Unlike the light mass nuclei, densities obtained from RMF(NL3) and E-RMF(G2) in these pairs of medium and heavy nuclei are not much different, even in the central region of the nucleus. Surprisingly, we find a deep minimum at the centre in the density distribution for $^{302}X_{120}$ nucleus, which is quite different from other densities obtained for normal nuclei as shown in Fig. 3.3. In the following, we use these, as well as some other densities, for the prediction of bulk properties.

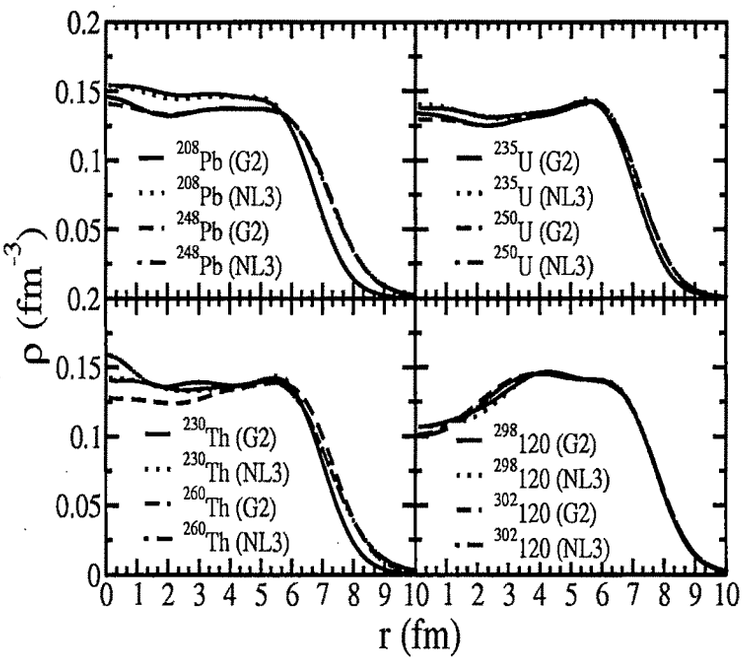

Figure 3.3: Same as Fig. 3.1, but for heavy nuclei.

The Proton and Neutron Densities

We calculate the density distribution of proton and neutron for $^{40,42,44,48}Ca$ isotopes by using RMF(NL3) and E-RMF(G2) parameter sets. From these densities, we estimate the relative isotopic neutron densities difference for both the force parameters. The comparison of $\Delta\rho_n(r)$ with the data [161] indicates the superiority of G2 over NL3.

In Fig. 3.4, we have plotted the proton ρ_p and neutron ρ_n density distribution for $^{40,42,44,48}Ca$ isotopes using NL3 and G2 parameter sets within RMF and E-RMF formalisms. From the figure, it is noticed that, there is a very small difference in densities for NL3 and G2 parameter sets. However, a careful inspection shows a small enhancement in central density (0-1.6 fm) for NL3 set. On the other hand the densities obtained from G2 is elongated to a larger distance towards the tail region and this nominal difference affects significantly in the study of bulk properties of the

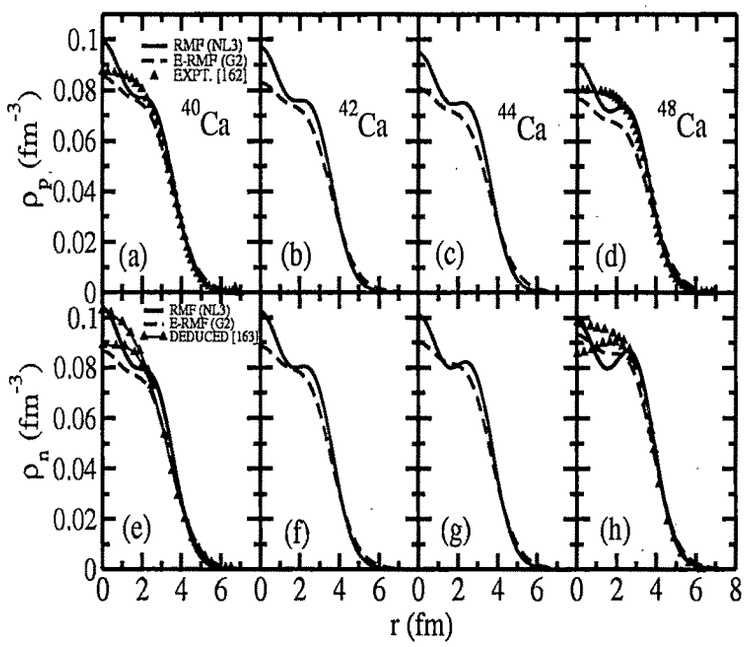

Figure 3.4: The proton ρ_p (upper panel) and neutron ρ_n (lower panel) density distribution for $^{40,42,44,48}Ca$ obtained from RMF (NL3) and E-RMF (G2) parameter sets. The experimental ρ_p and deduced ρ_n for $^{40,48}Ca$ are also compared.

nuclei as well as in the scattering phenomena of relativistic impulse approximation (RIA). Further, the agreement of ρ_p with experiment [162] and ρ_n with deduced data [163] for NL3 set is slightly better than that of G2. Explicitly, it is worthy to mention that the ρ_p (NL3) match with the data even at the central region, whereas the ρ_p of G2 under-estimate through out the whole density plot.

A microscopic investigation of Fig. 3.4 shows a change in $\rho_p(r)$, $\rho_n(r)$, i.e. the area covered by the proton and neutron densities gradually increases with mass number in an isotopic chain. From the $\rho_p(r)$ and $\rho_n(r)$, we estimate the possible relative isotopic density difference $\Delta\rho(r)$ for RMF (NL3) and E-RMF (G2) parameter sets (see Figs. 3.5 and 3.6).The calculated $\Delta\rho_p(r)$ are compared with the experimental data [162] in Fig. 3.5. The measured data of $\Delta\rho_p(r)$ lies in between the prediction of NL3 and G2 values as shown in Fig. 3.5. Comparing $\rho_p(^{42}Ca) - \rho_p(^{40}Ca)$, $\rho_p(^{44}Ca) - \rho_p(^{40}Ca)$, and $\rho_p(^{48}Ca) - \rho_p(^{40}Ca)$ of Fig. 3.5 [(a), (b) and (c)], we notice a better agreement

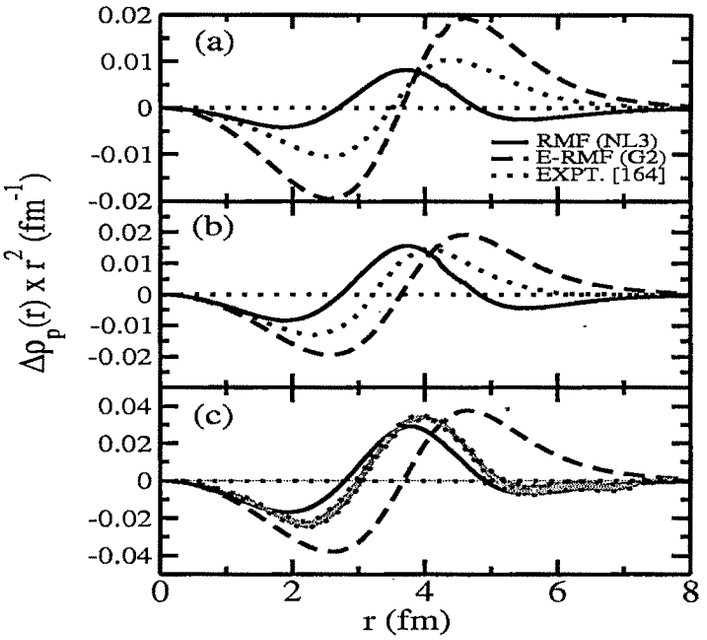

Figure 3.5: The relative isotopic proton density differences $\Delta\rho_p(r)$ for $\rho_p(^{42}Ca) - \rho_p(^{40}Ca)$, $\rho_p(^{44}Ca) - \rho_p(^{40}Ca)$, and $\rho_p(^{48}Ca) - \rho_p(^{40}Ca)$ obtained from RMF(NL3) and E-RMF(G2) are compared with the data [164] in (a), (b) and (c), respectively.

of NL3 value over G2 with respect to experimental measurement in the isotopic chain (see Fig. 3.5). The relative isotopic density difference for neutron $\Delta\rho_n(r)$ is compared in Fig. 3.6 with the deduced neutron density difference data [161] and the density-matrix-expansion prediction [165]. The predicted results with RMF (NL3) are agreed well only for the double closed shell nuclei ^{40}Ca and ^{48}Ca. But in case of E-RMF (G2) we get excellent match with the deduced $\Delta\rho_n(r)$ for the considered isotopic chain. There is a peak appears in $\Delta\rho_n(r)$ at radial range $r \sim 3.4 - 3.8fm$ and this peak slightly shifted towards the centre with increase of neutron number.

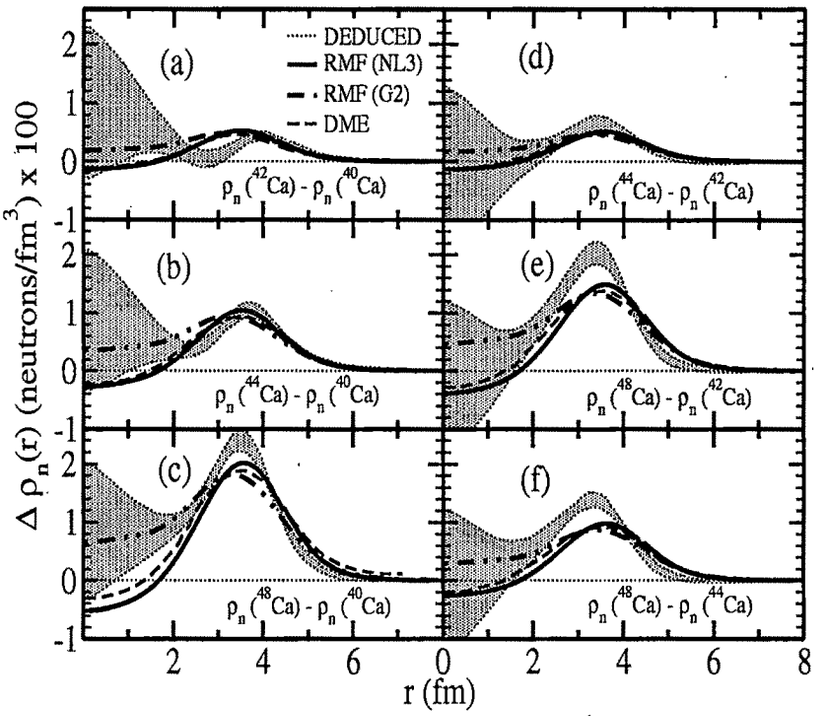

Figure 3.6: The relative isotopic neutron density differences $\Delta\rho_n(r)$ for $\rho_n(^{42}Ca) - \rho_n(^{40}Ca)$, $\rho_n(^{44}Ca) - \rho_n(^{40}Ca)$, $\rho_n(^{48}Ca) - \rho_n(^{40}Ca)$, $\rho_n(^{44}Ca) - \rho_n(^{42}Ca)$, $\rho_n(^{48}Ca) - \rho_n(^{42}Ca)$, and $\rho_n(^{48}Ca) - \rho_n(^{44}Ca)$. The RMF (NL3) and E-RMF (G2) $\Delta\rho_n(r)$ are compared with the density-matrix-expansion (DME) data [165] and the uncertainty deduced neutron difference [161].

3.2.2 Binding Energies

(a) Ground State

We have presented in Tables 3.1, 3.2, 3.3, and 3.4 the calculated binding energies, using RMF and E-RMF formalisms with NL3* and G2 forces, respectively, for some light, medium and heavy nuclei. The experimental data, taken from Ref. [166, 167], are also given for comparisons. It is evident from these Tables that both the calculated binding energies from NL3* and G2 parameter sets are similar and coincide very well with the experimental data. A further inspection of the tables shows that for light nuclei (Table 3.1, 3.2) and Table 3.3 for nuclei in medium mass region, some of the NL3* results are slightly lower than the experimental values. On the other hand,

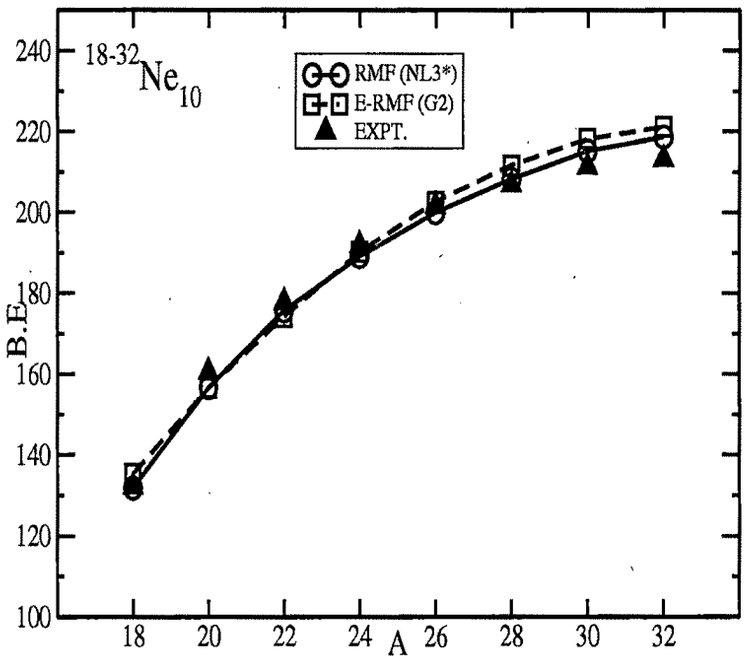

Figure 3.7: Calculated binding energy B.E for $^{18-32}$Ne isotopes using RMF and E-RMF models is compared with the experimental data.

the results predicted by G2 set over estimate the data, and vice versa for the heavier nuclei. The calculated B.E for $^{18-32}$Ne and $^{204-214}$Pb isotopes are presented in Figs. 3.7 and 3.8. Here we observed that our results using NL3* and G2 parameter sets are similar and also agree with the experimental data [167]. We also know from the properties of the mean field formalism that it has some limitation for light mass region of the periodic table, and this small discrepancies with experimental values may be attributed to that. In any case, to get a qualitative estimation of the binding energy, the RMF as well as E-RMF results are trust worthy and can be used for further calculations in this light mass region. Analysis of the binding energies for heavy mass nuclei, shows that, our results are a few MeV lower than the experimental data. Unlike the light mass region, the mean field approximation is extremely suited to the heavier

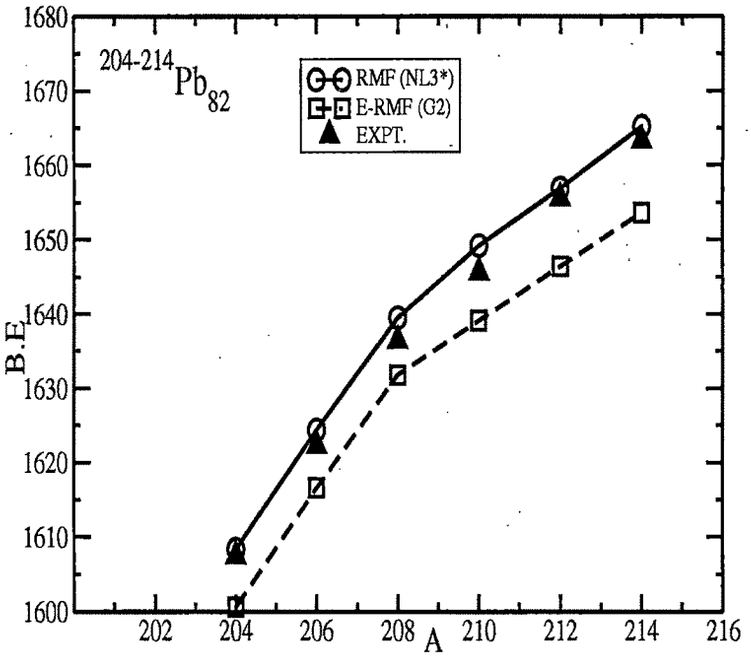

Figure 3.8: Same as Fig. 3.7, but for $^{204-214}$Pb isotopes.

mass region of the periodic table. However, although the mean field approximation is properly applicable for these heavy nuclei, these nuclei are well deformed which we have ignored in our calculations. Hence, due to this approximation, we compromise a few MeV of binding energy in calculated values with experimental data.

(b) Intrinsic Excited State

The results obtained with SkI4, SLy6, NL3 and NL-SH are tabulated in Table 3.5. From these calculations it is understood that although we use two different models, the non-relativistic Skyrme Hartree-Fock and the relativistic mean field formalisms, we get global agreement between the results of the two approaches. To conform this, we repeat the calculations with several other non-relativistic and relativistic sets (non-relativistic SKO, SLy6 and relativistic NL-SH). We find almost similar results,

Table 3.1: Binding energy (BE), charge radius (r_c) and quadrupole deformation parameter β_2 for some light nuclei obtained from RMF(NL3*) and E-RMF(G2) formalism compared with experimental data. The BE is in MeV and charge radius in fm.

Nucleus	BE			r_c			β_2	
	RMF	E-RMF	Expt.	RMF	E-RMF	Expt.	RMF	Expt.
^{4}He	34.45	29.39	28.30	2.063	2.076	1.676(8)	0.0398	
^{5}He	34.64	29.87	27.41	2.054	2.045		0.0993	
^{6}He	35.05	31.37	29.27	2.039	2.003	2.068(11)	0.1163	
^{7}He	36.31	33.86	28.83	2.039	1.958		0.1006	
^{8}He	37.84	37.27	31.41	2.011	1.912	1.929(26)	0.0786	
^{6}Li	35.11	31.85	31.99	2.445	2.508	2.51(6)	0.411	0.0167
^{7}Li	39.59	36.47	39.24	2.373	2.345	2.39(3)	0.4618	0.7114
^{8}Li	44.29	42.17	41.28	2.322	2.256	2.29(8)	0.3739	
^{9}Li	49.92	48.75	45.34	2.282	2.195	2.22(9)	0.2979	
^{10}Li	51.58	51.10	45.32	2.319	2.234		0.1708	
^{11}Li	54.34	54.23	45.64	2.355	2.256	2.217(35)	0.0930	0.178
^{8}B	41.58	44.05	37.74	2.734	2.924		0.6695	
^{9}B	55.79	55.64	56.31	2.65	2.671		0.8014	
^{10}B	66.01	61.42	64.75	2.519	2.533	2.45(12)	0.4870	
^{11}B	76.92	77.08	76.21	2.397	2.573		0.2325	
^{13}B	88.86	89.45	84.45	2.49	2.536		0.0971	
^{15}B	92.52	93.20	88.19	2.959	2.479	2.511	0.5988	
^{17}B	94.67	96.23	89.53	2.524	2.456		0.6264	
^{20}B	94.39	98.13		2.59	2.510		0.2796	
^{9}C	43.39	45.79	39.04	2.776	3.021		0.3805	
^{12}C	91.09	87.22	92.16	2.363	2.497	2.44(2)	0.0609	0.0041
^{14}C	106.97	105.49	105.28	2.516	2.539	2.56(5)	0.0009	0.0019
^{16}C	111.86	108.93	110.75	2.565	2.531		0.4414	
^{18}C	116.82	114.05	115.66	2.601	2.526		0.4663	
^{19}C	117.86	121.98	116.24	2.596	2.543		0.3747	
^{20}C	119.49	123.90	119.18	2.588	2.542		0.2756	
^{22}C	124.26	126.90	120.74	2.578	2.539		0.0081	

Table 3.2: Same as Table 3.1 but for some other light nuclei.

Nucleus	BE			r_c			β_2	
	RMF	E-RMF	Expt.	RMF	E-RMF	Expt.	RMF	Expt.
^{14}O	100.25	98.96	98.73	2.732	2.765		0.0014	
^{16}O	128.80	127.21	127.62	2.725	2.719	2.701	0.0005	0.0040
^{18}O	139.54	141.92	139.81	2.724	2.70	2.775	0.2211	0.0045
^{20}O	151.57	154.09	151.37	2.725	2.686		0.2481	0.0028
^{22}O	163.18	165.59	162.03	2.711	2.685		0.0038	
^{24}O	171.51	173.37	168.95	2.736	2.69		0.0054	
^{16}F	113.64	116.19	111.42	2.885	2.953		0.1808	
^{18}F	138.05	141.40	137.37	2.846	2.869		0.2508	
^{20}F	155.00	158.19	154.40	2.844	2.837		0.3853	
^{22}F	168.78	171.99	167.74	2.817	2.798		0.2682	
^{24}F	180.17	183.60	179.11	2.955	2.797		−0.1268	
^{26}F	187.90	192.00	184.16	2.855	2.821		0.1370	
^{18}Ne	131.84	135.25	132.14	2.963	3.055	2.972	0.238	0.0267
^{20}Ne	156.68	156.57	160.65	2.972	2.986	3.005	0.537	0.034
^{22}Ne	175.65	174.12	177.77	2.94	2.904	2.954	0.502	0.023
^{24}Ne	189.09	190.29	191.84	2.88	2.879	2.903	−0.259	0.014
^{26}Ne	200.00	202.85	201.55	2.926	2.887	2.927	0.277	
^{28}Ne	208.26	211.83	206.88	2.965	2.927	2.963	0.225	
^{30}Ne	215.2	218.43	211.3	2.992	2.967		0.046	
^{31}Ne	216.3	220.3	211.6	3.027	2.977		0.228	
^{32}Ne	218.7	221.48	213.2	3.069	2.986		0.369	
^{18}Na	113.84	119.65	111.64	3.105	3.326		0.3694	
^{20}Na	146.51	149.23	145.97	3.032	3.074	2.972	0.3965	
^{22}Na	172.99	172.00	174.15	3.012	3.012	2.985	0.5043	
^{24}Na	192.36	191.78	193.52	2.964	2.947	2.974	0.3795	
^{26}Na	207.18	208.50	208.11	2.965	2.943	2.993	0.2953	
^{28}Na	219.06	221.82	218.34	3.004	2.972	3.039	0.2722	
^{30}Na	228.20	231.47	225.16	3.031	3.008	3.117	0.1689	
^{22}Mg	166.42	165.63	168.58	3.092	3.142		0.5128	0.032
^{24}Mg	194.31	189.44	198.26	3.043	3.037	3.057	0.4874	0.0432
^{26}Mg	212.54	211.20	216.68	2.978	2.982	3.033	0.2728	0.0305
^{28}Mg	228.76	228.45	231.63	3.048	3.011		0.3447	0.034
^{30}Mg	240.51	241.68	241.64	3.062	3.042		0.2406	
^{32}Mg	250.59	252.69	249.81	3.090	3.076		0.1190	
^{34}Mg	257.39	259.47	256.48	3.150	3.091		0.3432	

Table 3.3: Same as Table 3.1 but for some nuclei in medium mass region.

Nucleus	BE			r_c			β_2	
	RMF	E-RMF	Expt.	RMF	E-RMF	Expt.	RMF	Expt.
^{26}Si	200.86	202.84	206.04	3.118	3.136		−0.2800	0.0352
^{28}Si	232.13	230.54	236.54	3.122	3.065	3.122	−0.3308	0.0326
^{30}Si	250.58	251.55	255.62	3.070	3.09	3.133	0.1481	0.0215
^{32}Si	268.45	269.25	271.41	3.137	3.116		−0.2007	0.028
^{34}Si	284.45	285.05	283.43	3.147	3.152		0.0005	
^{36}Si	291.57	295.59	292.03	3.186	3.166		−0.1616	
^{40}Ca	341.96	341.12	342.02	3.468	3.454	3.476	0.0001	0.0096
^{42}Ca	360.00	361.85	361.90	3.468	3.448	3.506	−0.0690	0.042
^{44}Ca	378.61	381.03	380.96	3.471	3.445	3.516	0.1140	0.047
^{46}Ca	396.97	398.99	398.77	3.471	3.443	3.492	0.0949	0.0181
^{48}Ca	409.19	415.81	416.00	3.526	3.44	3.474	−0.2662	0.0084
^{50}Fe	415.44	413.56	417.71	3.712	3.697	3.515	0.2661	
^{52}Fe	444.67	441.61	447.70	3.692	3.683		0.2275	
^{53}Fe	456.55	454.79	458.39	3.678	3.677		0.1714	
^{54}Fe	468.25	468.23	471.76	3.662	3.672	3.693	−0.0732	0.062
^{56}Fe	488.93	486.55	492.23	3.717	3.689	3.737	0.2280	0.098
^{58}Fe	505.59	503.74	509.95	3.747	3.708	3.775	0.2388	0.120
^{50}Co	399.56	400.49	399.65	3.735	3.74		0.1890	
^{52}Co	431.92	430.60	432.48	3.72	3.721		0.1918	
^{53}Co	447.61	445.42	449.32	3.71	3.734		0.1734	
^{54}Co	460.26	459.99	462.74	3.692	3.708		−0.0717	
^{56}Co	484.14	484.25	486.91	3.708	3.711		−0.0906	
^{58}Co	504.19	503.15	506.86	3.747	3.728		0.1896	
^{50}Ni	383.87	385.13	385.25	3.766	3.779		−0.1194	
^{52}Ni	417.32	417.91	420.68	3.746	3.756		−0.1230	
^{53}Ni	433.56	433.87	435.55	3.734	3.748		−0.1008	
^{54}Ni	449.91	449.57	453.17	3.724	3.741		−0.0756	
^{56}Ni	483.07	480.24	483.99	3.708	3.731		−0.0014	
^{58}Ni	502.61	500.96	506.46	3.749	3.747	3.775	0.1344	0.072
^{60}Ni	521.50	520.54	526.85	3.791	3.767	3.812	−0.1629	0.091
^{62}Ni	540.99	539.14	545.26	3.826	3.79	3.841	−0.1991	0.083
^{64}Ni	557.48	557.17	561.76	3.833	3.815	3.859	−0.1356	0.087

Table 3.4: Same as Table 3.1 but for some heavy nuclei. The values of experimental data [168] are also given for comparison.

Nucleus	BE			r_{ch}			β_2	
	RMF	E-RMF	Expt.	RMF	E-RMF	Expt.	RMF	Expt.
^{204}Pb	1608.44	1600.56	1607.51	5.506	5.48	5.479	−0.0643	
^{206}Pb	1624.42	1616.64	1622.33	5.509	5.488	5.489	−0.0220	
^{208}Pb	1639.52	1631.80	1636.43	5.529	5.499	5.498	−0.0133	
^{210}Pb	1649.22	1639.05	1645.55	5.544	5.515	5.523	−0.0150	
^{212}Pb	1656.92	1646.42	1655.58	5.562	5.531	5.545	−0.0203	
^{214}Pb	1665.22	1653.63	1663.29	5.584	5.548	5.565	−0.0288	
^{230}Th	1751.24	1736.83	1755.13	5.948	5.763	5.692	−0.3892	
^{232}Th	1761.74	1747.20	1766.68	5.963	5.776	5.720	−0.3883	
^{234}Th	1770.71	1757.33	1777.66	5.951	5.788		0.4152	
^{236}Th	1781.44	1767.25	1787.94	5.946	5.799		0.3840	
^{238}Th	1794.92	1776.99	1797.85	5.898	5.811		0.3050	
^{240}Th	1803.97	1786.97		5.902	5.823		0.2977	
^{242}Th	1811.86	1796.38		5.923	5.835		0.3069	
^{235}U	1784.49	1764.62	1783.86	5.863	5.813	5.833	0.2809	
^{238}U	1800.22	1780.74	1801.69	5.889	5.830	5.859	0.2861	
^{240}U	1810.83	1791.27	1812.42	5.915	5.840		0.2849	
^{242}U	1825.48	1802.05	1822.74	5.93	5.852		0.2879	
^{244}U	1829.33	1812.27		5.946	5.864		0.307	
^{246}U	1837.37	1822.33		5.959	5.875		0.298	
^{248}U	1845.58	1832.25		5.970	5.887		0.291	
^{250}U	1853.15	1842.36		5.975	5.899		0.285	
$^{298}X_{120}$	2098.02	2083.87		6.494	6.29		−0.3529	
$^{300}X_{120}$	2110.45	2097.32		6.498	6.297		−0.3444	
$^{302}X_{120}$	2122.98	2110.47		6.512	6.303		−0.3486	

Table 3.5: Ground and intrinsic excited state binding energies (BE), charge radii (r_c), and deformation parameters (β_2) of ^{53}Co and ^{53}Fe nuclei. The experimental binding energies are taken from [166], and the deformation parameters are from finite-range droplet model (FRDM) [80].

N	BE(in MeV)					r_c(in fm)		β_2		
	Set	RMF	Set	SHF	Expt.	RMF	SHF	RMF	SHF	FRDM
^{53}Co	NL3	448.3	SkI4	449.7	449.3	3.75	3.74	0.14	0.20	0.098
		447.2		447.3		3.75	3.73	−0.07	−0.12	
	NL-SH	449.4	SLy6	447.0		3.74	3.74	0.13	0.30	
		448.4		445.0		3.74	3.74	−0.07	−0.11	
^{53}Fe	NL3	457.2	SkI4	457.5	458.4	3.70	3.80	0.14	0.29	0.098
		456.1		455.9		3.71	3.70	−0.07	−0.12	
	NL-SH	458.4	SLy6	455.5		3.71	3.70	0.13	0.30	
		457.5		453.7		3.69	3.66	−0.07	−0.14	

compared to the results for SkI4 and NL3 forces. For example, in SKO force, the ground state BE of ^{53}Co is 448.9 MeV with $\beta_2 = 0.30$ and the oblate BE is 447.1 MeV with $\beta_2 = -0.17$. These values for ^{53}Fe are 457.3 MeV and 455.5 MeV with $\beta_2 = 0.30$ and -0.17, respectively.

In Table 3.5, the free energy solutions for the ground states give the binding energies for ^{53}Co and its mirror nucleus ^{53}Fe, calculated in both the RMF and SHF theories. The experimental data, taken from Ref. [166], are also given for comparisons. It is evident from Table 3.5 that the two calculated binding energies are similar, and agree well with the experimental binding energies. Note that, though the mass number of two nuclei is the same, due to the mirror image of proton and neutron numbers, the total binding energies are much different in the two cases. The difference in ground state binding energies and the intrinsic excited state binding energies between these two nuclei are 8.95 MeV and 8.97 MeV in RMF and 7.78 MeV and 8.567 MeV in SHF, respectively. The experimental mirror energy difference is 9.08 MeV for the ground state of these nuclei (to be compared with 8.95 and 7.78 MeV, respectively, for RMF and SHF). Hence, the quantitative estimation of the binding

energy gives us a confidence that the RMF as well as SHF (more so the RMF) results are trust worthy and can be used for further calculations of other properties. As a point of caution, note that the considered nuclei are very close to the proton drip-line, and that the calculated quantities refer to intrinsic states, not directly related to the experimental values displayed in Table 3.5. However, the calculated binding energy of the ground state even then match pretty well with the experimental data. In general, the agreement is quite good though in some parameter set the discrepancy between the experimental and calculated results is considerable. These facts give us confidence to study some other properties like nuclear charge radius, deformation, potential energy surface, single particle energy spectra in this state which are discussed in subsequent subsections.

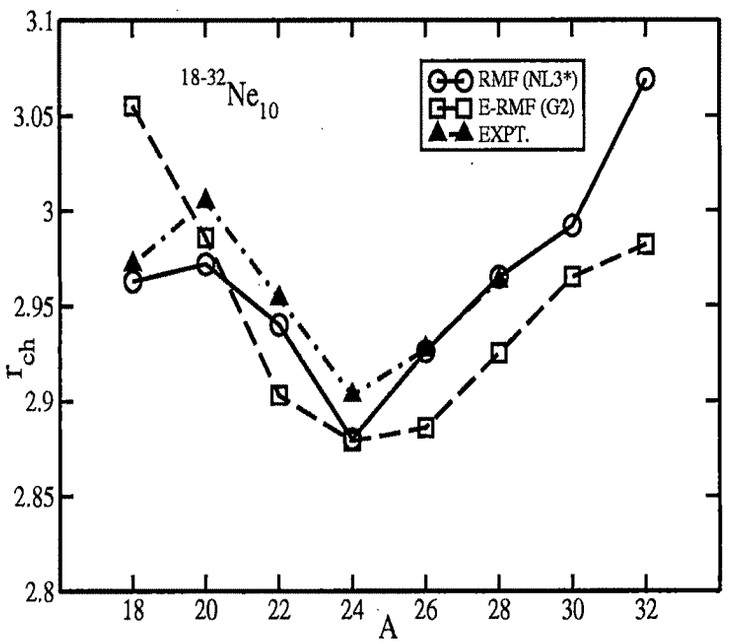

Figure 3.9: Calculated nuclear charge radii r_c for $^{18-32}$Ne isotopes using RMF and E-RMF models in comparison with the experimental data.

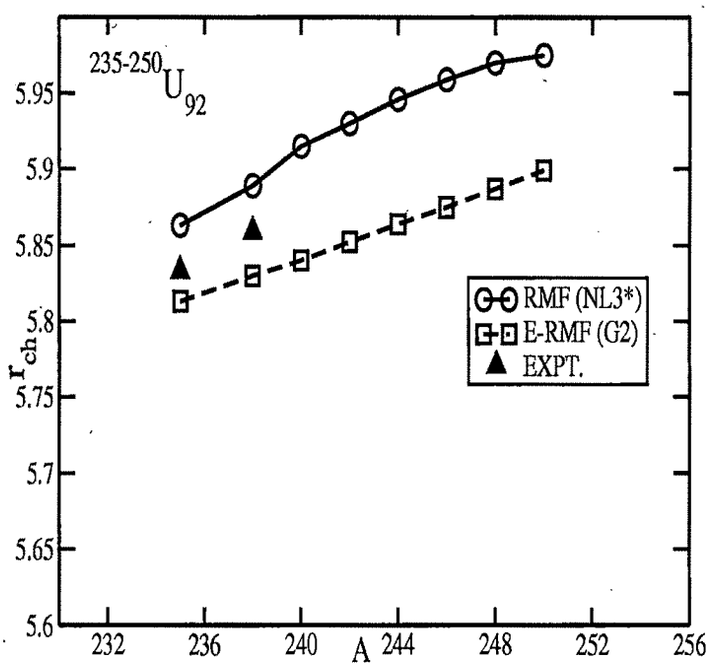

Figure 3.10: Same as Fig. 3.9, but for $^{235-250}$U isotopes.

3.2.3 Nuclear Radii

(a) Ground State

The root mean square (rms) charge radius (r_c) is obtained from the point proton rms radius through the relation [47] $r_c = \sqrt{r_p^2 + 0.64}$, considering the size of proton radius as 0.8 fm. Tables 3.1, 3.2, 3.3 and 3.4 show the calculated nuclear charge radii r_c using RMF and E-RMF models together with the experimental data, wherever available. We notice from these tables that both models (RMF as well as E-RMF) give similar results for the rms charge radii and both account fairly well for the experimentally observed values. In Figs. 3.9 and 3.10 we have plotted nuclear charge radii r_c for $^{18-32}$Ne and $^{235-250}$U isotopes using both RMF(NL3*) and E-RMF(G2) models. Both the results show a good agreement with the experimental data [169].

However, comparison of r_c with the data shows the advantage of NL3* over G2 due to the deformation. Since the charge radius is obtained from the density profile, and our RMF and E-RMF results for r_c match the experimental data rather well, we can reliably use these density profiles in the calculations of cross sections.

(b) Intrinsic Excited State

In Table 3.5, we have presented the calculated nuclear charge radii for ^{53}Co and ^{53}Fe in intrinsic excited state. These results are obtained from the RMF and SHF models using non-relativistic SKI4, SLy6, and relativistic NL3, NL-SH parameter sets. We notice from this Table that both the models give similar results. No experimental data on charge radii are available for these nuclei.

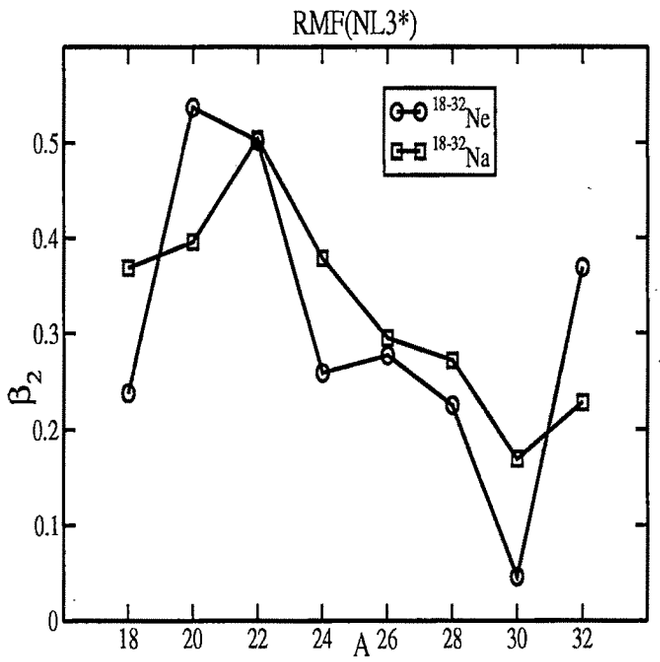

Figure 3.11: Quadrupole Deformation Parameter β_2 for $^{18-32}$Ne and $^{18-32}$Na isotopes using RMF formalism.

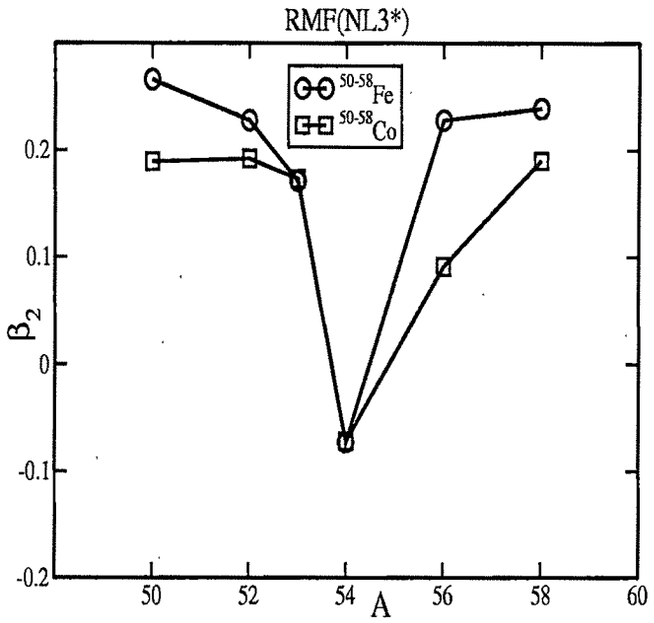

Figure 3.12: Same as Fig. 3.11, but for $^{50-58}$Fe and $^{50-58}$Co isotopes.

3.2.4 Quadrupole Deformation Parameter

(a) Ground State

The Quadrupole Deformation Parameter β_2 is calculated for ground states in all regions using both RMF and E-RMF formalisms. It is observed that our results are in good agreement with available experimental data. Tables 3.1, 3.2, 3.3 and 3.4 contains the calculated β_2 using both RMF and E-RMF models with available experimental data. From the Fig. 3.11, it is clear that the ground state shape of Ne and Na isotopes have prolate shape and there is no change in deformation. It can be further seen in the figure, that the magnitude of the ground state deformation increases from A=18 to 20 then it decreases up to A=30. Fig. 3.12 indicate similar nature of deformation for both Fe and Co isotopes. There is a sign change in β_2 from +ve to -ve at A=53 and there after again +ve. We also found reasonable agreement in general with FRDM calculations for the β_2 values of U isotopes in Fig. 3.13.

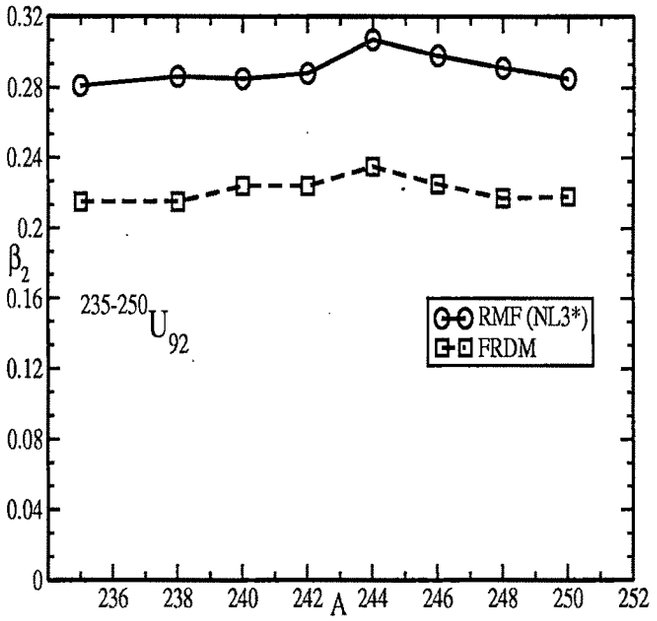

Figure 3.13: Same as Fig. 3.11, but for U isotopes compared with FRDM results.

(b) Intrinsic Excited State

The quadrupole deformation parameter β_2 for both the ground and first excited state is also determined within the two formalisms. In some of the earlier RMF and SHF calculations, it was shown that the quadrupole moment obtained from these theories reproduce the experimental data pretty well [6, 36, 41, 95, 99, 100, 101, 112, 158, 159]. To our knowledge, the experimental data on β_2 for ^{53}Co or ^{53}Fe are unknown. However, the comparison with FRDM results [80, 81] for ground state deformation show that these are closer to the RMF results than to SHF. we get significant differences in the quadrupole deformation parameter β_2 in between non-relativistic Skyrme Hartree-Fock and the relativistic mean field formalisms. This occurs because of the difference in Nilsson orbits of the odd-nucleons near the Fermi level, which can be seen in the subsection Single-particle Energy Spectra.

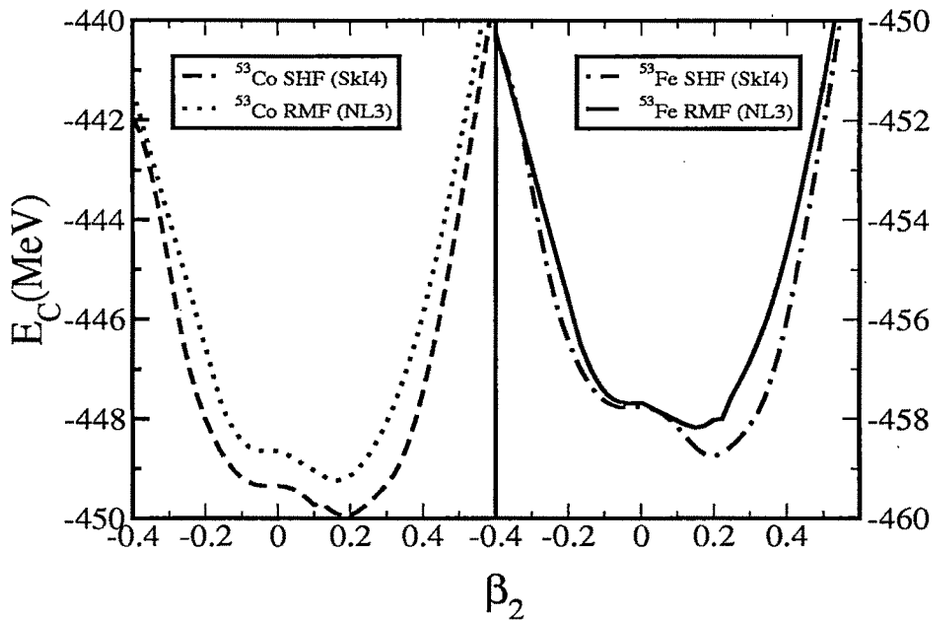

Figure 3.14: Potential energy as a function of the quadrupole deformation parameter β_2 for ^{53}Fe and ^{53}Co, using the RMF and SHF formalisms.

3.2.5 Potential Energy Surface

In this subsection, we first calculate the potential energy surfaces (PES) by using both the RMF and SHF theories in a constrained calculation [170, 171, 172, 173], that is, instead of minimizing the H_0, we minimize $H' = H_0 - \lambda Q_2$, with λ as a Lagrange multiplier and Q_2, the quadrupole moment, i.e., the binding energy corresponding to the solution at a given quadrupole deformation. Here, H_0 is the Dirac mean field Hamiltonian (the notations are standard and its form can be seen in Refs. [41, 171, 173] for the RMF model, and it is a Schrödinger mean field Hamiltonian for the SHF model. In other words, we get the constrained binding energy from $E_c = \sum_{ij} \frac{<\psi_i|H_0-\lambda Q_2|\psi_j>}{<\psi_i|\psi_j>}$ and the free energy from $BE = \sum_{ij} \frac{<\psi_i|H_0|\psi_j>}{<\psi_i|\psi_j>}$. In our calculations, the free energy solution does not depend on the initial guess value of the basis deformation β_0 as long as it is nearer to the minimum in PES. However it converges to some other local

minimum when β_0 is drastically different, and in this way we evaluate a different isomeric state for a given nucleus. Note that the BE value coincides with the constrained solution when the quadrupole moment of the constrained calculation matches with the Q_2 value of the free energy solution.

The potential energy surface PES, i.e., the potential energy as a function of quadrupole deformation parameter β_2, for ^{53}Co is shown in Fig. 3.14 (dotted and dashed lines in left panel). Both the RMF and SHF results are given for comparisons. The calculated PES is shown for a wide range of oblate to prolate deformations. We notice that minima appear at around β_2= -0.07 and 0.14. The energy difference between the ground and the isomeric state is found to be 1.11 MeV in the RMF calculations. It is observed from the PES that the two minima are not really well defined, thereby making questionable this excited isomeric configuration of ^{53}Co. If one examines it minutely, a shallow minimum appears near the spherical-oblate of the PES. On this shallow minimum, because of the flat bottom of the PES (the base of the curve looks almost flat starting from β_2 $\sim$-0.2 to 0.35), the building of an intrinsic resonance state is possible, which we treat here as an oblate intrinsic band. This resonance intrinsic state with respect to the ground state minimum is separated by a small barrier, which we interpret here as a sign of softness between these two states. The calculations are repeated for ^{53}Fe (right panel), the mirror nucleus of ^{53}Co. Here also similar results are obtained. The predicted results of SHF calculations match extremely well with the RMF theory.

We have seen in Fig. 3.14 that the PES has an almost flat bottom. To testify further the existence of isomeric states, we calculate the "free solutions" both in the prolate and oblate deformed configurations of ^{53}Co. We find that in the RMF formalism the prolate solution converge at the deformation β_2=0.14 and oblate solution at β_2=-0.07, with an energy difference ΔE=1.11 MeV. Similarly, the SHF formalism gives two free solutions at β_2=0.20 and -0.12 with an energy difference ΔE=2.41

Table 3.6: Some of the odd neutron and proton single-particle orbits $[Nn_3\Lambda]2\Omega^\pi$, the single-particle energies (s.p.e.) in Mev near the Fermi surface, and the occupation probabilities (o.p.) of proton and neutron orbits in relativistic mean field formalism (RMF) with NL3 parameter set, respectively, for ^{53}Co and ^{53}Fe. The total quadrupole deformation parameter β_2 for these nuclei for the ground and isomeric resonance states are also tabulated.

N	β_2	orbit	s.p. e.	o.p.	N	β_2	orbit	s.p. e.	o.p.
^{53}Co	0.14	$[330]1/2^-$	-7.67	0.95	^{53}Co	−0.07	$[303]7/2^-$	-6.97	0.94
		$[321]3/2^-$	-6.98	0.93			$[312]5/2^-$	-6.15	0.91
		$[312]5/2^-$	-5.70	0.85			$[321]3/2^-$	-5.55	0.87
		$[303]7/2^-$	-3.86	0.50			$[310]1/2^-$	-5.27	0.50
		$[330]1/2^-$	-0.39	0.06			$[301]3/2^-$	0.44	0.05
^{53}Fe	0.14	$[330]1/2^-$	-16.78	0.96	^{53}Fe	−0.07	$[303]7/2^-$	-16.09	0.95
		$[321]3/2^-$	-16.08	0.94			$[312]5/2^-$	-15.24	0.92
		$[312]5/2^-$	-14.77	0.88			$[321]3/2^-$	-14.62	0.89
		$[303]7/2^-$	-12.87	0.50			$[310]1/2^-$	-14.32	0.50
		$[330]1/2^-$	-9.04	0.06			$[301]3/2^-$	-8.06	0.044

MeV. These free energy solutions continue for ^{53}Fe, the mirror nucleus of ^{53}Co. In this case also, we predict the prolate solution as the ground band and the oblate solution as the low-lying intrinsic excited state, similar to the case of ^{53}Co. The free energy solutions for both the nuclei are presented in Table 3.6.

3.2.6 Single-Particle Energy Spectra

In this subsection, the single-particle (s.p.) energy levels for the ^{53}Co and ^{53}Fe nuclei in their ground and first excited intrinsic state (1st e.s.) solutions are plotted in Figs. 3.15 and 3.16. Fig. 3.15 shows the s.p. energy levels for RMF and Fig. 3.16 that of SHF, for a qualitative comparison of two different formalisms. In both figures, levels are shown for all occupied and the first unoccupied states, but the first unoccupied state in case of ^{53}Co for β_2=-0.07 is not shown because this level lies in the positive energy region at ϵ_p=0.438 MeV. In Figs. 3.15 and 3.16, the Nilsson levels are shown with indices $[Nn_3\Lambda]2\Omega^\pi$ and $2\Omega^\pi$, respectively, but in the following discussion we use

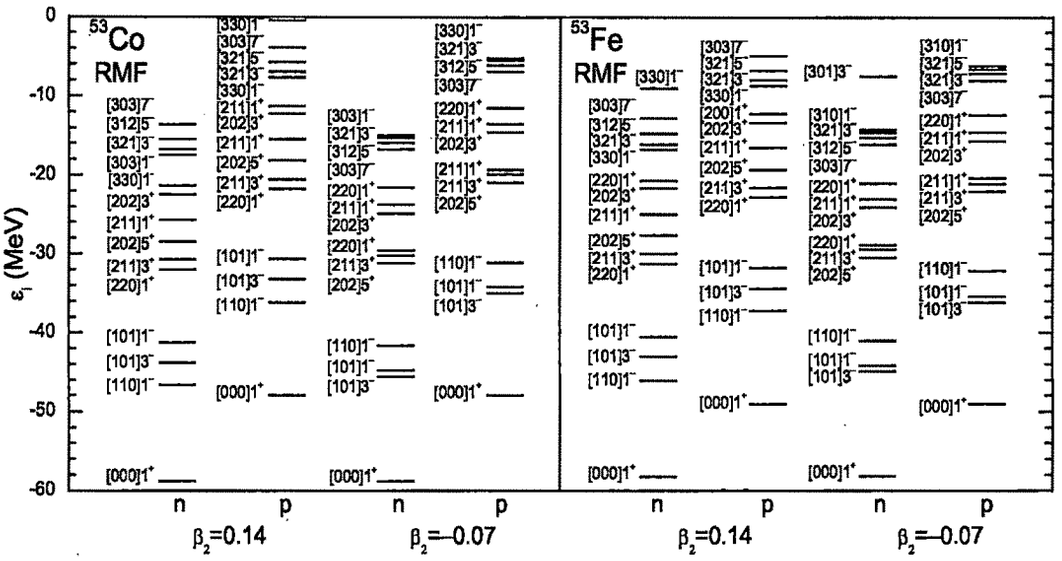

Figure 3.15: The single-particle energy levels for ^{53}Fe and ^{53}Co in the RMF formalism using NL3 parameter set. The levels are labeled by the asymptotic quantum numbers $[Nn_3\Lambda]2\Omega^\pi$.

the regular indices $[Nn_3\Lambda]2\Omega^\pi$. Analysing the s.p. energy levels, we find that the results obtained from these two different formalisms are fairly similar. However, we notice significant differences in single particle levels near the Fermi surface.

There are 27 protons and 26 neutrons in ^{53}Co and, in general, the ground state spin of this nucleus is determined by the last unpaired proton, near the Fermi surface. Analysing the s.p. levels for this configuration, we find that the last occupied proton configuration is $[303]7/2^-$ in both the RMF and SHF formalisms. Hence, the spin of ^{53}Co in its ground state is $7/2^-$. In the intrinsic excited state (e.s.) the configuration is, however, different. This is a low-lying intrinsic configuration with an excitation energy ΔE [$= BE(g.s.) - BE(1^{st}\ e.s.)$] of 1.110 MeV in RMF formalism having a small oblate deformation β_2=-0.07 and ΔE=2.41 MeV with β_2=-0.12 in SHF. Note, however, that, although the energy difference between the prolate ground state and

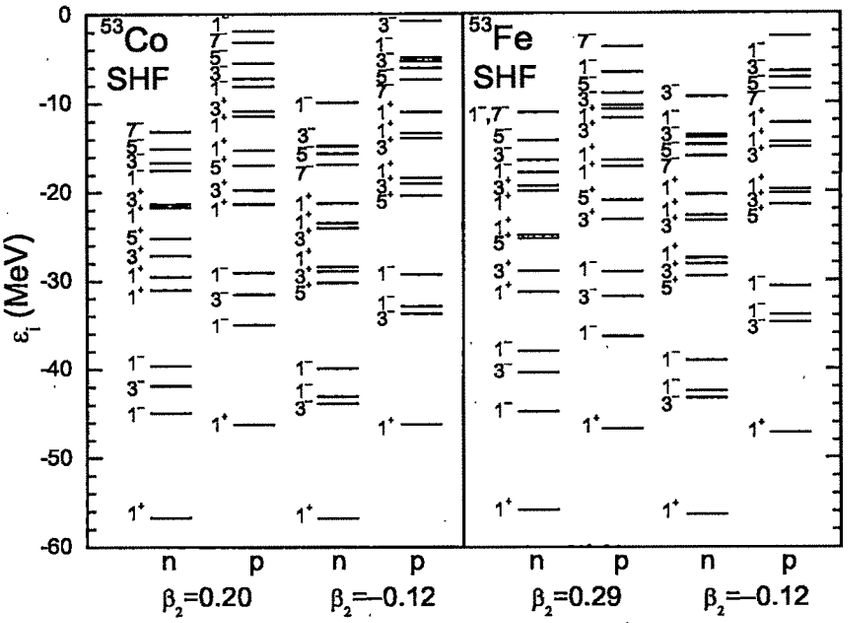

Figure 3.16: The same as for Fig. 3.15, but in the SHF formalism using SkI4 parameter set. For each level, the label denotes the quantum numbers $2\Omega^{\pi}$.

the oblate intrinsic resonance state solutions in RMF and SHF is more than a factor of 2, this prolate-oblate difference comes from a large cancellation of a few hundred MeV, and hence we can say that the ΔE values in the two formalisms agree fairly well with each other.

Table 3.6 shows, for RMF, the single-particle energies (s.p) and occupation probabilities (o.p.) for some of the active orbits near the Fermi surface. The single-particle energies for SHF are given in Table 3.7. Each level has a maximum capacity to occupy 2 particles with occupation probability 1. If the value of o.p. is 0.5, then the level is occupied fully by one nucleon (due to blocking approximation). A large o.p. close to unity (e.g., 0.865, 0.905, etc., in Table 3.6) also means a fully occupied level by two nucleons. The s.p. energy and o.p. for the odd nucleon number are displayed because of their crucial role in determining the spin-parity of the states in a nucleus.

Table 3.7: Same as for Table 3.6, but in the non-relativistic mean field formalism (SHF) with the SkI4 parameter set, and without the occupation probabilities (o.p.) of proton and neutron orbits.

N	β_2	orbit	s.p. e	N	β_2	orbit	s.p. e.
^{53}Co	0.20	[330]1/2$^-$	-8.09	^{53}Co	−0.12	[303]7/2$^-$	-7.33
		[321]3/2$^-$	-7.18			[312]5/2$^-$	-6.05
		[312]5/2$^-$	-5.53			[321]3/2$^-$	-5.26
		[303]7/2$^-$	-3.12			[310]1/2$^-$	-4.96
		[330]1/2$^-$	-1.84			[301]3/2$^-$	-0.78
^{53}Fe	0.29	[330]1/2$^-$	-17.81	^{53}Fe	−0.12	[303]7/2$^-$	-16.03
		[321]3/2$^-$	-16.45			[312]5/2$^-$	-14.76
		[312]5/2$^-$	-14.22			[321]3/2$^-$	-13.96
		[303]7/2$^-$	-11.10			[310]1/2$^-$	-13.67
		[303]7/2$^-$	-11.06			[301]3/2$^-$	-9.33

The configurations of protons near the Fermi level are [310]1/2$^-$, [321]3/2$^-$, [312]5/2$^-$ and [303]7/2$^-$. These group of protons reside very close to each other because of their small differences in s.p. energy. Specially, the two levels [310]1/2$^-$ and [321]3/2$^-$ are almost degenerate (s.p. energy difference $\Delta E_{s.p.} = 0.286$ MeV in RMF) and have a competition between them to be occupied near the Fermi surface. Similarly, we find the value of $\Delta E_{s.p.} = 0.30$ MeV in Table 3.7 for SHF calculations for the single particle states 3/2$^-$ and 1/2$^-$. Thus, the prediction of the spin for the oblate configuration is independent of the RMF or SHF formalism used. The present predictions of spin and parity of the first intrinsic excited oblate state is also in agreement with the shell model calculations of Ref. [156], based on the formalism and interactions of Refs. [174, 175].

Next, for ^{53}Fe, the mirror nucleus of ^{53}Co, the number of protons and neutrons changes, and as a result the spin of the nucleus is determined by the last unpaired neutron. The right-hand-sides of Figs. 3.15 and 3.16 show, respectively, for RMF and SHF the s.p. levels of ^{53}Fe for the ground and first excited states. The calculations give us the ground state spin value of ^{53}Fe as 7/2$^-$ in RMF and 1/2$^-$ in SHF which is

a prolate solution. Further, analysing the s.p. energy of the SHF solution in Table 3.7, we find the very next unoccupied neutron level is $7/2^-$ with $\epsilon_n(7/2^-)$=-11.064 MeV, which is only 0.04 MeV above the last occupied neutron level. This small difference in s.p. energy of the last occupied and first unoccupied neutron level can change the predictions of the ground state spin of ^{53}Fe and hence the difference in g.s. spin-parity of RMF and SHF can not be taken seriously. Similar to the oblate state of ^{53}Co, here also a strong competition appears for the $[310]1/2^-$ and $[321]3/2^-$ states in the oblate configuration of ^{53}Fe. The energies of these single particle states are $\epsilon_p(1/2^-)$=-14.32 MeV and $\epsilon_p(3/2^-)$=-14.614 MeV in RMF and ϵ_p=13.96 MeV and ϵ_p=13.67 MeV in SHF.

As already mentioned earlier, it is important to note that the ground state spin-parity of ^{53}Co is $7/2^-$ and that of the isomeric state is a mixture of $3/2^-$ and $1/2^-$. Note that it is not the difference in spin between these two states, but the change in internal structure in going from ground to excited state, i.e., from prolate to slightly oblate, which makes a finite life-time of the isomeric state.

3.2.7 Conclusions

In summary, we have studied some finite nuclei in light, medium and heavy mass region. It is evident from the results that RMF and E-RMF formalisms determine the total density, protons and neutrons density distributions and the bulk properties, such as binding energy (BE), root mean square charge radius r_{ch}, and quadrupole deformation parameter β_2 for nuclei quite successfully. It is clear that our RMF results agree remarkably well with the data [166, 169]. In conclusion, the ground states of finite nuclei are highly dependent on the input density and the choice of parametrization. We have also calculated the single-particle energy levels of ^{53}Co and ^{53}Fe by using the relativistic and non-relativistic mean field formalism. The

potential energy surfaces are also evaluated within the RMF and SHF techniques, which coincide remarkably well. From the single-particle energy spectra for ^{53}Co, the ground state spin and parity (J^{π}) were found to be $7/2^{-}$ and a highly admixed state of $1/2^{-}$ and $3/2^{-}$ spin-parity states was found to be the first excited state, which agree well with the shell model calculations reported in [156]. Same situation is noticed in case of ^{53}Fe, i.e., the last neutron occupies the level $[303]7/2^{-}$ in the ground state solution and it is a mixture of $[310]1/2^{-}$ and $[321]3/2^{-}$ levels in the oblate excited state. The overall general trend is observed to be the same in both the RMF and SHF formalism. It is worth mentioning here that shell model is quite successful in its traditional low mass region, whereas the mean field formalism are in general more appropriate for heavier nuclei. However, in one of our earlier study [176] based on RMF formalism, it is shown that at least an α−particle is needed to get a reasonable binding energy and mass number should be more than $\sim$9 for the rms radii and other physical properties. The mass number A=53 in the present investigation, is rather large to get a satisfactory result for both the RMF and SHF theories.

Though the barrier in the PES does not suggest a clearly separated excited isomeric state but the "free solutions" and the large plateau at the bottom, explicitly in the oblate region, is the cause for the oblate band which gives a long lived isomeric state in the low-lying excited state of ^{53}Co and ^{53}Fe nuclei. Apparently, the change in internal structure, in going from ground prolate to excited oblate, makes the life-time of the isomeric state finite.

Chapter 4

Total nuclear reaction cross sections and differential elastic cross sections

4.1 Introduction

With the development of radioactive ion beams (RIBs) in various laboratories around the globe it could be possible to study about unstable nuclei. This has opened new channels in the context of both nuclear structure and nuclear astrophysics [177]. Unstable nuclei play an influential, role in many phenomena in the cosmos such as novae, supernovae, X-Ray and Gamma Rays Bursts (GRBs) and other stellar explosions. In a recent paper [178], it is shown that in relativistic jets of GRBs or supernovae jets near the nascent neutron star, the formation of ultra neutron-rich and superheavy nuclei is possible. The sources of the formation of these nuclei are the nuclear reactions and fusion phenomena in the cosmological objects.

The direct study of stellar properties in ground-based laboratories has become more feasible, due to the availability of RIBs; for example, the study of ^{18}Ne induced neutron pick-up reaction could reveal information about the exotic ^{15}O+^{19}Ne reaction, happening in the CNO cycle in stars. Study of the structure and reactions of unstable nuclei is therefore required to improve our understanding of the astrophysical origin

of atomic nuclei, and the evolution of stars and their (sometimes explosive) death. The possible formation of highly neutron-rich nuclei and the recent report on the possible discovery of $^{292}X_{122}$ nucleus [179] in chemical process motivated us to study the nuclear reaction properties of some highly neutron-rich targets as well as the projectiles.

Recent developments in the secondary radioactive beam technology allow to study the various nuclear cross sections, such as, the total nuclear reaction cross sections (σ_r), differential elastic scattering cross sections ($\frac{d\sigma}{d\Omega}$) and Coulomb break-up cross sections. Study of these quantities enables us to know the nuclear structure of unstable nuclei in detail, particularly the halo structure near the drip-lines [113, 114, 147, 148, 149]. This will also help in studying the formation of neutron-rich nuclei that are surrounded by a high pressure or temperature. Thus, the total nuclear reaction cross section both for proton-nucleus and nucleus-nucleus scattering has been a subject of interest for the last few decades [180, 181, 182, 183]. The main objective of the present chapter is to study the total nuclear reaction cross sections of exotic nuclei using the densities obtained from relativistic mean field (RMF) and field theory motivated effective Lagrangian approach (E-RMF) in conjunction with the Glauber model.

4.2 Results and Discussion

4.2.1 Ground state properties of finite nuclei

The standard RMF model have been enormously successful to calculate the ground-state properties of finite nuclei through out the periodic table. This model is successful not only for nuclei near the valley of stability, but also far away from the $\beta-$stability line [47]. On the other hand, the recently developed E-RMF formalism reproduces the properties of finite nuclei as well as with the RMF model, with an additional success of describing the properties of nuclear matter, including the properties of

astrophysical objects like neutron star [113, 114, 123, 125, 149]. In standard RMF, with NL3 parameter set, the nuclear matter compressibility $K_\infty \sim 271.5$ MeV [112], which is slightly more than the empirical value of $K_\infty = 210 \pm 30$ MeV [152]. It is around 215 MeV [113, 114] in E-RMF formalism, with G2 parameter set which is closer to the data.

In the calculation of total nuclear reaction cross section, density is the input in the Glauber model. If we estimate nuclear radii properly, then our predictions for total nuclear cross sections will be accurate. For this reason, first of all we have evaluated the ground-state binding energies, nuclear radii and densities, etc., using the RMF and E-RMF formalisms, which are given in Tables 4.1 and 4.2 and Figures 4.1 and 4.2. In some of our earlier works [184, 185], it was demonstrated that the reaction cross section does not depend much on the deformation of reacting nuclei; therefore, in our present calculations, we will proceed with spherical densities, i.e., without taking the deformation into account. For the choice of parameter set, although there exist a number of parameter sets for solving the standard RMF as well as E-RMF Lagrangians, we have employed here the most successful NL3 set for the former and G2 for the later formalism.

Nuclear Density

The nuclear densities, obtained from Eq. 2.38 of chapter 2, using both RMF(NL3) and E-RMF(G2) are plotted in Figs. 4.1 and 4.2. These are the most crucial and required quantities for our calculations of the total nuclear cross sections using the Glauber model. Fig. 4.1 depicts the densities for some representative light nuclei, to be used as projectiles in our calculations. We notice from Fig. 4.1 that the nuclear densities for RMF(NL3) and E-RMF(G2) for lighter nuclei are considerably different near the centre of the nucleus. This difference reduces as we go away from the middle of the nuclei towards the surface.

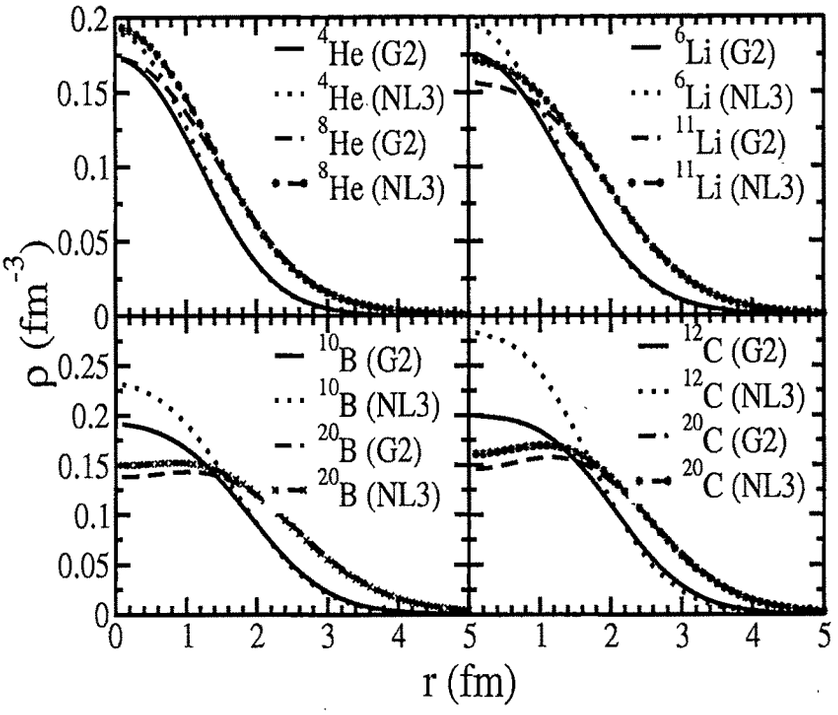

Figure 4.1: Ground state densities for some light nuclei (as projectiles) obtained from the RMF(NL3) and E-RMF(G2) formalisms.

As expected, the density distribution is elongated for neutron-rich nuclei, as compared to the stable isotopes. All the pairs of nuclei (^{4}He, ^{8}He), (^{6}Li, ^{11}Li), (^{10}B, ^{20}B), and (^{12}C, ^{20}C) shown here present the same features for the light mass region. Similarly, in Fig. 4.2, we have shown the density distributions for pairs of nuclei (^{208}Pb, ^{258}Pb), (^{235}U, ^{280}U), (^{230}Th, ^{260}Th), and the recent, possibly discovered, naturally occurring superheavy $^{292}X_{122}$ (Z=122, N=170) [179] and its neutron-rich isotope $^{320}X_{122}$. Unlike the light mass nuclei, densities obtained from RMF(NL3) and E-RMF(G2) in these pairs of heavy nuclei are not much different, even in the central region of the nucleus. Surprisingly, we find a deep minimum at the centre in the density distribution for the $^{320}X_{122}$ nucleus, which is quite different from other heavy nuclei as shown in the Fig. 4.2. Here, we use these and some other densities, for the prediction of σ_r.

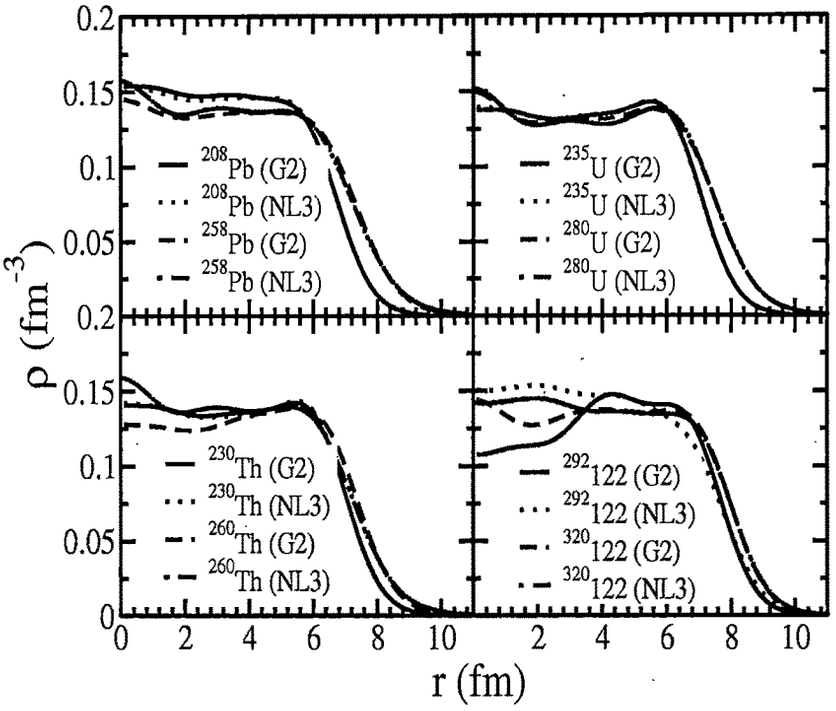

Figure 4.2: Same as for Fig. 4.1, but for heavy nuclei (as targets).

Binding Energies

We have presented in Tables 4.1 and 4.2, the calculated binding energies, using RMF and E-RMF formalisms with NL3 and G2 forces, respectively, for light and heavy nuclei to be used as projectiles and targets in the following calculations of reaction cross sections. The experimental data, taken from Ref. [166], are also given for comparisons. It is evident from Tables 4.1 and 4.2 that both the calculated binding energies from RMF(NL3) and E-RMF(G2) models are similar and coincide very well with the experimental data. A further inspection of the tables shows that for light nuclei (Table 4.1) some of the RMF(NL3) results are slightly lower than the experimental values. On the otherhand, the results predicted by the E-RMF(G2) set overestimate the data, and vice versa for the heavier nuclei. We also know from the properties of the mean field formalism that it has some limitation for the light mass region of the

Table 4.1: Binding energy (BE), root mean square (rms) charge radius (r_c) for light nuclei (used as projectiles) obtained from RMF(NL3) and E-RMF(G2) formalisms compared with experimental data. The BE is in MeV and rms radius in fm.

Nucleus	BE [166]			r_c		
	RMF	E-RMF	Expt.	RMF	E-RMF	Expt. [Ref.]
^{4}He	34.47	29.39	28.30	2.063	2.076	1.676(8) [186]
^{5}He	34.62	29.87	27.41	2.054	2.045	
^{6}He	35.15	31.37	29.27	2.039	2.003	2.068(11) [186]
^{7}He	36.23	33.86	28.83	2.039	1.958	
^{8}He	37.44	37.27	31.41	2.011	1.912	1.929(26) [186]
^{6}Li	29.82	31.85	31.99	2.546	2.508	2.51(6) [187]
^{7}Li	34.04	36.47	39.24	2.375	2.345	2.39(3) [187]
^{8}Li	39.44	42.17	41.28	2.291	2.256	2.29(8) [187]
^{9}Li	45.83	48.75	45.34	2.239	2.195	2.22(9) [187]
^{10}Li	48.23	51.10	45.32	2.283	2.234	
^{11}Li	51.50	54.23	45.64	2.323	2.256	2.217(35) [188]
^{10}B	59.18	61.42	64.75	2.451	2.492	2.45(12) [189]
^{15}B	84.90	88.20	88.19	2.497	2.479	
^{17}B	85.57	90.13	89.52	2.524	2.456	
^{20}B	86.58	92.13		2.58	2.510	
^{12}C	88.21	87.22	92.16	2.363	2.497	2.44(2) [189]
^{14}C	104.32	105.49	105.28	2.506	2.539	2.56(5) [189]
^{16}C	106.50	108.93	110.75	2.525	2.531	
^{18}C	110.40	114.05	115.66	2.545	2.526	
^{20}C	115.93	120.73	119.18	2.566	2.522	

periodic table, and hence the discrepancies of RMF results with experimental data could be attributed to that fact. In any case, to get a qualitative estimation of the binding energy, the RMF as well as E-RMF results are trust worthy and can be used for further calculations in the chosen light mass region.

Our analysis of the binding energies for heavy mass nuclei, which we use here as the targets for nuclear reactions, shows that, except for ^{208}Pb, our results are a few MeV lower than the experimental data. Unlike the light mass region, the mean field approximation is extremely suited to the heavier mass region of the periodic table. However, although the mean field approximation is properly applicable for these

Table 4.2: Same as for Table 4.1, but for heavy nuclei (used as targets).

Nucleus	BE [166]			r_c		
	RMF	E-RMF	Expt.	RMF	E-RMF	Expt. [Ref.]
^{208}Pb	1637.62	1631.80	1636.43	5.523	5.499	5.498(10) [189]
^{210}Pb	1644.22	1638.42		5.426	5.515	
^{218}Pb	1673.84	1667.87		5.623	5.583	
^{228}Pb	1709.10	1704.48		5.693	5.665	
^{238}Pb	1738.53	1735.89		5.754	5.733	
^{248}Pb	1765.68	1764.75		5.812	5.792	
^{258}Pb	1789.11	1790.21		5.868	5.848	
^{260}Pb	1792.76	1794.23		5.879	5.858	
^{230}Th	1732.77	1725.70	1755.13	5.739	5.711	
^{240}Th	1767.75	1763.49		5.800	5.777	
^{250}Th	1800.03	1797.75		5.859	5.838	
^{260}Th	1828.47	1827.94		5.913	5.891	
^{270}Th	1910.40	1906.78		6.007	5.982	
^{235}U	1778.65	1764.62	1783.86	5.833	5.813	
^{238}U	1793.50	1780.74	1801.69	5.851	5.830	5.8434 [189]
^{250}U	1850.67	1842.36		5.923	5.899	
^{260}U	1893.33	1887.37		5.982	5.959	
^{270}U	1930.71	1925.40		6.025	6.001	
^{280}U	1952.73	1947.30		6.087	6.053	
$^{292}X_{122}$	2037.34	2019.90		6.306	6.284	
$^{320}X_{122}$	2213.01	2195.90		6.477	6.453	

heavy nuclei, these nuclei are well deformed which is ignored here in our calculations. Hence, due to this simplification, we compromise a few MeV of binding energy in calculated values with experimental data, which does not affect the nuclear reaction cross sections, as reported in Ref. [184, 185].

Nuclear Radii

The root mean square (rms) charge radius (r_c) is obtained from the point proton rms radius through the relation [47] $r_c = \sqrt{r_p^2 + 0.64}$, where the factor 0.64 accounts for the finite size effects of protons with radius 0.8 fm. Tables 4.1 and 4.2 show the calculated nuclear charge radii r_c using RMF and E-RMF models together with the experimental data, wherever available. We notice from these tables that both models (RMF as well as E-RMF) give similar results for the rms charge radii and both account fairly well for the experimentally observed values. Since the charge radius is obtained from the density profile, and our RMF and E-RMF results for r_c match the experimental data rather well, we can reliably use these density profiles in the calculations of nuclear reaction cross sections, which is one of the main objective of the present study.

4.2.2 Coefficients of Gaussian functions fitted to mimic the density distributions

The nuclear densities obtained above from the RMF and E-RMF models for the projectile and target nuclei, which are the main ingredients of the calculation of total nuclear reaction cross sections, have been fitted to a sum of two Gaussians in Eq. 2.77 of chapter 2, and the calculated coefficients c_1, c_2 and ranges a_1, a_2 are listed in Tables 4.4 and 4.5. This fitting procedure simplifies the numerical calculations considerably [190, 191], and makes it possible to obtain analytic expressions for the transparency functions defined in Eqs. (2.79) and (2.81) of chpter 2. In other words,

Table 4.3: The averaged nucleon-nucleon cross sections $\bar{\sigma}_{NN}$ (in fm^2) and other parameters used for the calculation of profile function at different incident energies (in MeV/nucleon).

Energy	30	49	85	100	120	150	200
$\bar{\sigma}_{NN}$	19.6	10.4	6.1	5.29	4.72	3.845	3.28
α_{NN}	0.87	0.94	1.0	1.435	1.38	1.245	0.93
β_{NN}	0.0	0.0	0.0	1.02	1.07	1.15	1.24
Energy	325	425	500	625	800	1100	2200
$\bar{\sigma}_{NN}$	3.03	3.025	3.62	4.0	4.26	4.32	4.335
α_{NN}	0.305	0.36	0.04	-0.095	-0.07	-0.275	-0.335
β_{NN}	0.62	0.48	0.125	0.16	0.21	0.22	0.26

using these coefficients [in Eq. (2.77) of chapter 2], we get the equivalent density for calculating the transparency functions, which are further used to estimate the total nuclear reaction and differential elastic scattering cross sections, as discussed in Section 4. Some phenomenological parameters, related to the NN cross section, required to evaluate the profile function in Eq. (2.81) of chapter 2 are $\bar{\sigma}_{NN}$, α_{NN}, and β_{NN}, at different incident energies. In our calculation, these values are taken from Refs. [134, 192], which are tabulated in Table 4.3.

Here, $\bar{\sigma}_{NN}$ stands for the total reaction cross section of NN collisions, α_{NN} is the ratio of the real to the imaginary part of the forward NN scattering amplitude, and β_{NN} is the slope parameter. The β_{NN} value estimates the fall of the angular distribution of the NN elastic scattering. It is to be noted that these parameters, in general, depend on the isospin of the nucleons (pp, nn, pn), and hence appropriate average values are obtained by interpolating a given set. The nucleon-nucleon cross section $\bar{\sigma}_{NN}$, averaged over neutron and proton numbers, is calculated by the expression [134, 192].

$$\bar{\sigma}_{NN}(E) = \frac{N_p N_t \sigma_{nn} + Z_p Z_t \sigma_{pp} + N_p Z_t \sigma_{np} + N_t Z_p \sigma_{np}}{A_p A_t} \tag{4.1}$$

with A_p, A_t, Z_p, Z_t and N_p, N_t as the projectile and the target mass, charge and neutron numbers, respectively. It is worth mentioning that the value of the input parameter $\bar{\sigma}_{NN}$ does not effect much with the neutron or proton number of the target and projectile system. Thus, we have presented an average number in Table 4.3 for all the systems for a particular incident energy. However, it is the driving agent for the energy dependence of total reaction cross section.

4.2.3 Total nuclear reaction cross sections

Total nuclear reaction cross sections with known experimental data

In our present calculation, we follow the procedure of *CSC_GM* computer code [133]. In this method, the projectile nucleus is considered as a core plus a valence nucleon. For example, ^{11}Li nucleus is taken as the ^{10}Li+$0p_{1/2}$−nucleon system. The present technique is very much useful for loosely bound (exotic or drip-line) nuclei, the projectile systems. Although the entire calculation is in the centre-of-mass co-ordinate system, where there is no distinction between the projectile and the target, we use this terminology in order to distinguish them from one another. Throughout our calculation, in most of cases, the lighter nucleus is a projectile and the heavier one a target nucleus. After calculating the density profiles with RMF(NL3) and E-RMF(G2) methods, we estimate the coefficients of the Gaussian function, and use them in the *CSC_GM* computer code [133] for evaluating the total nuclear reaction cross sections for some light nuclei (as projectiles) on ^{12}C (as the target in each case), where experimental measurements are available [193]. This is shown in Fig. 4.3 and Table 4.6.

Table 4.4: The coefficients c_1, a_1 and c_2, a_2 of Gaussian functions, which are fitted to the density distributions generated from RMF (NL3) and E-RMF(G2) formalisms, for light nuclei (as projectiles).

Nucleus	RMF(NL3)				E-RMF(G2)			
	c_1	a_1	c_2	a_2	c_1	a_1	c_2	a_2
^{4}He	-1.0509	0.51495	1.2495	0.49740	-1.1713	0.50925	1.3524	0.49014
^{6}He	-1.198	0.34612	1.4179	0.34624	-1.1019	0.36487	1.2955	0.35688
^{8}He	-1.1984	0.28378	1.4166	0.28392	-1.0958	0.32531	1.2874	0.31328
^{6}Li	-1.2017	0.33840	1.4137	0.33839	-1.2093	0.39648	1.3988	0.38215
^{7}Li	-1.1050	0.36237	1.3188	0.352	-0.024616	0.87759	0.211	0.29915
^{8}Li	-1.18856	0.369719	1.4063	0.35237	-0.0483286	0.685948	0.235086	0.287981
^{9}Li	-0.029093	0.874689	0.245801	0.2808	-0.0788126	0.590314	0.266483	0.280958
^{11}Li	-0.0540616	0.628475	0.231925	0.231428	-0.0988483	0.51542	0.260122	0.237837
^{10}B	-0.145385	0.573468	0.379899	0.316861	-1.21283	0.394773	1.40704	0.353843
^{15}B	-0.299572	0.425976	0.480853	0.253374	-1.22064	0.3313	1.38249	0.284846
^{17}B	-0.224314	0.427336	0.396452	0.219516	-0.454951	0.344816	0.609667	0.236565
^{20}B	-0.180161	0.41492	0.339182	0.184949	-0.299283	0.341646	0.444999	0.197008
^{12}C	-0.232695	0.638683	0.517266	0.339919	-3.34808	0.379357	3.5471	0.359102
^{14}C	-3.77882	0.365346	3.96791	0.344481	-4.2207	0.347703	4.38557	0.330334
^{16}C	-1.32397	0.353965	1.50772	0.300361	-1.4157	0.336181	1.57637	0.289213
^{18}C	-0.610957	0.360143	0.785873	0.256258	-1.36173	0.312325	1.51661	0.266353
^{20}C	-0.522227	0.346399	0.687736	0.232099	-1.36876	0.291422	1.51713	0.247912

Table 4.5: Same as for Table 4.4, but for heavy nuclei (as targets).

Nucleus	RMF(NL3)				E-RMF(G2)			
	c_1	a_1	c_2	a_2	c_1	a_1	c_2	a_2
^{208}Pb	-2.64313	0.0532685	2.75724	0.0492428	-2.64946	0.0535256	2.766	0.0494824
^{210}Pb	-2.62315	0.0526782	2.73639	0.0486948	-2.65783	0.0531674	2.77348	0.0491542
^{218}Pb	-2.48912	0.0498046	2.59786	0.0460278	-2.79344	0.0515383	2.9102	0.0476675
^{228}Pb	-2.62604	0.0490159	2.73098	0.0453354	-2.66333	0.0494732	2.77043	0.0457665
^{248}Pb	-2.89059	0.0483861	2.99443	0.0447702	-2.59034	0.0458371	2.69484	0.0424171
^{260}Pb	-2.45222	0.0435363	2.56011	0.040285	-2.50225	0.0437805	2.6093	0.0405262
^{230}Th	-2.4835	0.047502	2.5857	0.043894	-2.54208	0.0479732	2.64437	0.0443404
^{240}Th	-2.67965	0.047258	2.77776	0.0437145	-2.6181	0.0468272	2.71599	0.0432986
^{250}Th	-2.74594	0.0464667	2.84506	0.0430046	-2.65942	0.0454064	2.75263	0.042005
^{270}Th	-2.74452	0.0462746	2.83967	0.0428277	-2.54056	0.042608	2.64133	0.0394314
^{235}U	-2.54853	0.0471019	2.64847	0.0435424	-2.54993	0.0471009	2.64931	0.0435372
^{238}U	-2.61151	0.0470922	2.71035	0.0435456	-2.58245	0.0467943	2.68049	0.0432664
^{250}U	-2.75588	0.046275	2.85145	0.0428272	-2.64917	0.0453065	2.74156	0.0419058
^{260}U	-2.456	0.0440042	2.56903	0.0407122	-2.694	0.0441555	2.78289	0.040853
^{270}U	-2.41462	0.0422599	2.52267	0.0390898	-2.62832	0.0429456	2.7238	0.039742
$^{292}X_{122}$	-3.30555	0.0435773	3.37668	0.0404026	-3.28593	0.043583	3.36194	0.0404295
$^{320}X_{122}$	-2.7657	0.0385546	2.85668	0.0357409	-2.69586	0.0383673	2.79456	0.0355931

Table 4.6: Total nuclear reaction cross sections, matter- and proton-distribution radii, obtained from RMF(NL3) and E-RMF(G2) formalisms and compared with experimental data [193] for various light projectiles on ^{12}C as target.

Projectile	σ_r (mb)			r_m (fm)			r_p (fm)		
	RMF	E-RMF	Expt.	RMF	E-RMF	Expt.	RMF	E-RMF	Expt.
^{20}Mg	1128.51	1198.65	1150(12)	2.86	2.88	2.86(3)	3.03	3.04	3.18(9)
^{20}Na	1125.77	1196.46	1094(11)	2.81	2.83	2.69(3)	2.91	2.93	3.14(5)
^{20}Ne	1148.29	1195.11	1144(10)	2.78	2.81	2.84(3)	2.80	2.83	3.10(7)
^{20}F	1124.30	1193.89	1113(11)	2.78	2.81	2.75(3)	2.70	2.74	2.98(4)
^{20}O	1125.73	1195.53	1078(10)	2.81	2.84	2.64(3)	2.60	2.64	2.72(5)
^{20}N	1132.36	1203.28	1121(17)	2.88	2.90	2.77(4)	2.54	2.59	2.39(20)

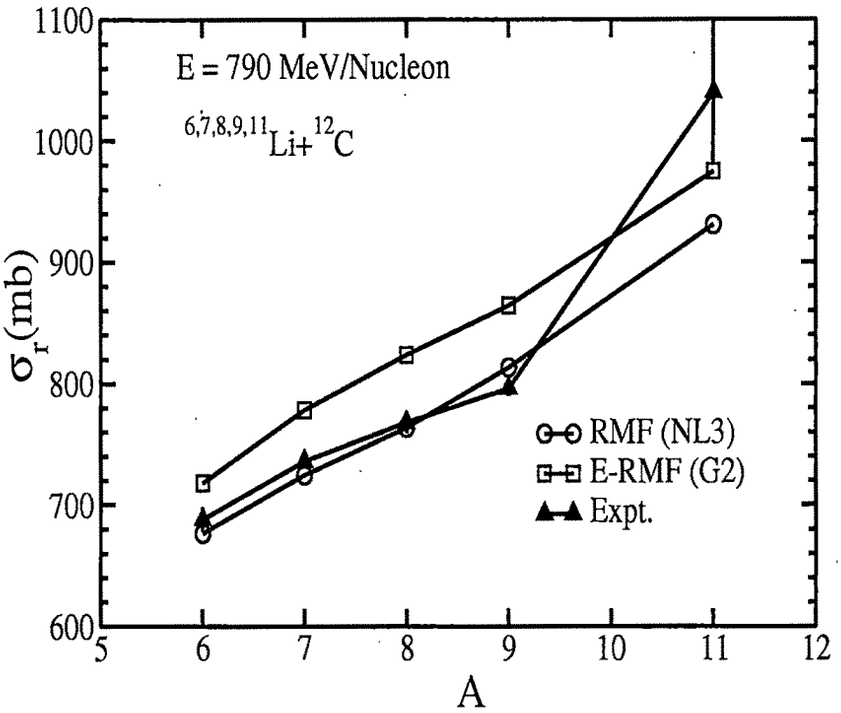

Figure 4.3: Calculated total nuclear reaction cross sections σ_r as a function of the projectile mass, compared with experimental data, for ^{6,7,8,9,11}Li+^{12}C reactions at 790 MeV/nucleon. The error bars in data are also shown.

From Fig. 4.3 for ^{6,7,8,9,11}Li+^{12}C at 790 MeV/nucleon, it is clear that the E-RMF(G2) model overestimates slightly the measured total nuclear reaction cross section σ_r data, whereas the results obtained from RMF(NL3) model agree well with the data. However, the halo nature of ^{11}Li is not reflected from Fig. 4.3, although an enhancement in total nuclear reaction cross section is evident for both the RMF(NL3) and E-RMF(G2) formalisms. In Table 4.6, we have compared our results of various other light projectiles on ^{12}C as the target, with the recently measured σ_r's of Bochkarev *et al.* [193]. We notice that the experimental data lie in between the RMF(NL3) and E-RMF(G2) predictions. The RMF slightly underestimates the data, whereas the E-RMF overestimates marginally. For example, in the case of ^{20}Mg, the RMF underestimates the experimental data by 1.7% and the E-RMF overestimates it

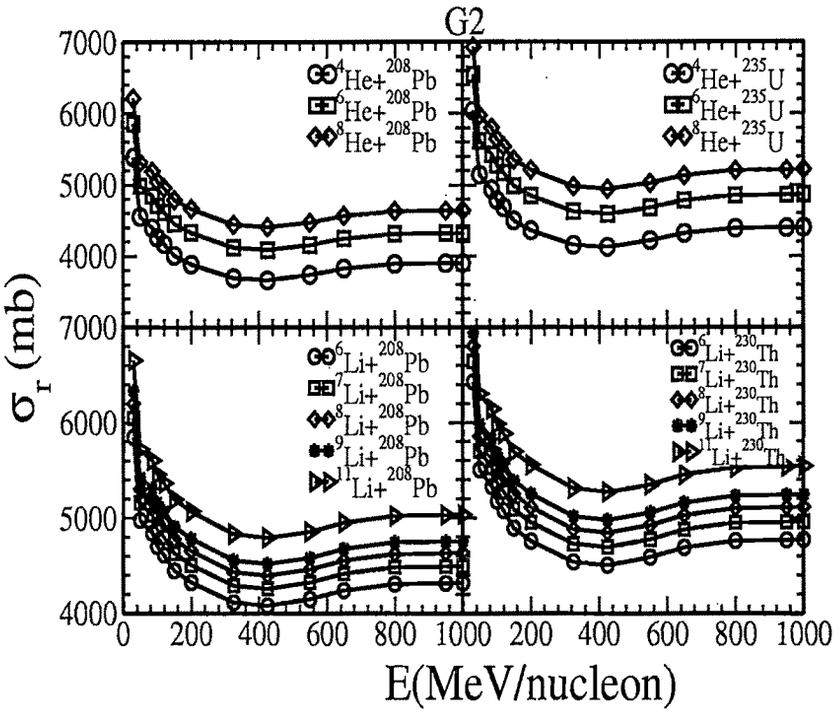

Figure 4.4: Calculated total nuclear reaction cross sections for E-RMF(G2) formalism, taking He and Li isotopes as projectiles with different isotopes of Pb, Th and U as targets.

by about 4%. In other words, our calculations with respect to experimental data are quite convincing, and can be extended to an unknown territory without the possibility of committing much error.

Total nuclear reaction cross sections for highly neutron-rich and superheavy nuclei

To measure the total reaction cross section for an unstable projectile with a stable target or an unstable target with a stable projectile or both as unstable nuclei is one of the challenging problems in experimental nuclear physics. As already mentioned in the Introduction, such measurements not only would provide a better understanding

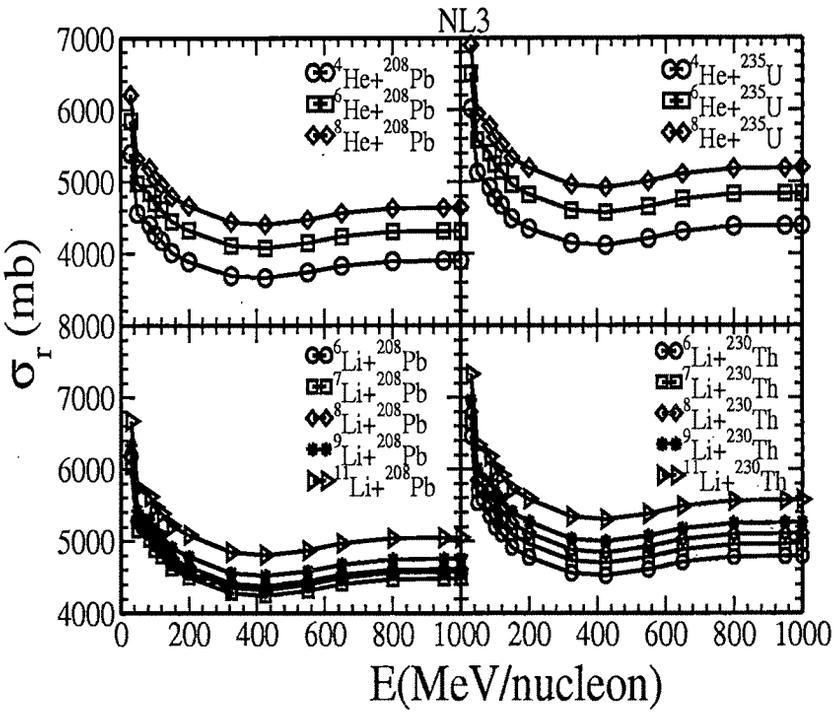

Figure 4.5: Same as for Fig. 4.4, but for RMF(NL3) formalism.

of the nuclear structure of such nuclei, but also are extremely useful for the formation of drip-line nuclei in many cosmological phenomena such as the X-Ray Bursts, GRBs, supernovae explosions and in relativistic jets of GRBs or supernovae jets near the nascent neutron star, and in the r-process nucleosynthesis. To study such processes, in recent decades, considerable efforts has been made underway to look for RIB+RIB cross sections at various laboratories [114, 147]. In this context, it is worth studying such reaction processes, because understanding the mechanism of the formation of neutron-rich nuclei and the creation of superheavy elements in important not only in the cosmological systems but also in various laboratories of the world [194, 195, 196, 197].

In some of our earlier works [184, 185], it was shown that the Glauber model works remarkably well for use of the RMF and E-RMF nuclear densities. The model

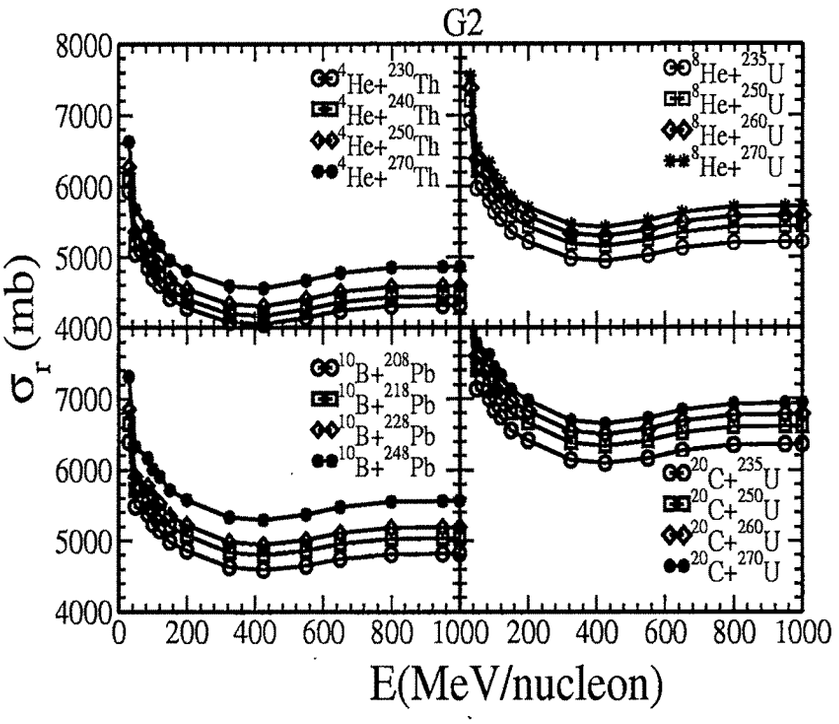

Figure 4.6: Same as for Fig. 4.4, but for He, B and C isotopes as projectiles with different isotopes of Pb, Th and U as targets.

reproduces experimental observables quite well for both the stable and unstable nuclei taken as targets and projectiles. In this chapter, we extend the work of Ref. [184, 185] to calculate the total nuclear reaction cross sections using light mass isotopes as projectiles and heavy nuclei as targets. For heavier nuclei, we also use the neutron-rich thermally fissile nuclei (neutron-rich U and Th isotopes) are more interesting from the point of view of energy production, not only in astrophysical systems but also in solving our future energy problems [198].

Figs. 4.4 to 4.9 present our calculated total nuclear reaction cross sections for some selective stable-stable, stable-unstable and unstable-unstable systems, such as He+Pb, He+U, He+Th, Li+Pb, Li+U, Li+Th, B+Pb, and C+U with different iso-

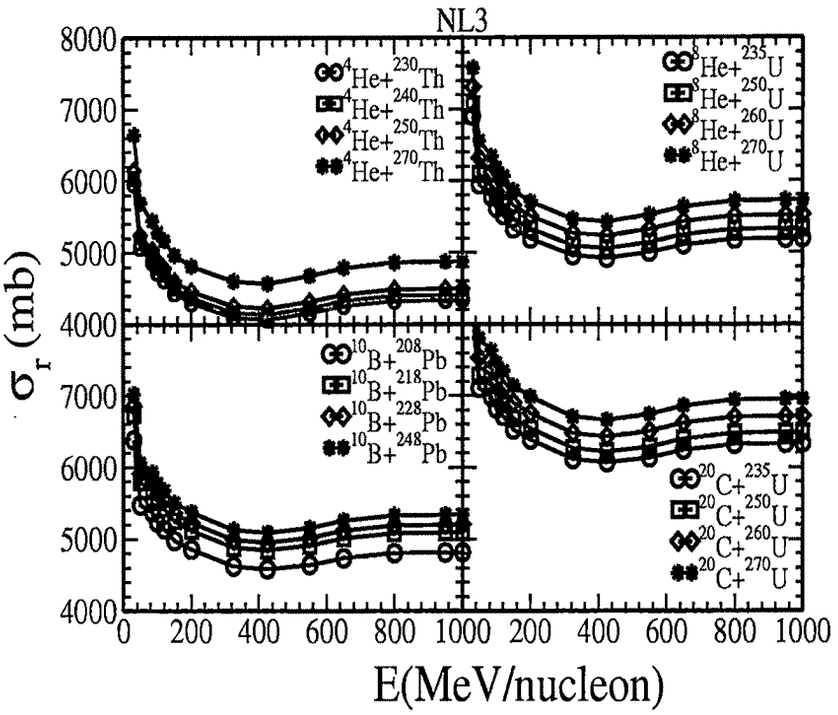

Figure 4.7: Same as Fig. 4.6, but for RMF(NL3) formalism.

topes. Figs. 4.4, 4.6 and 4.8 are for E-RMF (G2), and Figs. 4.5, 4.7 and 4.9 for RMF(NL3) formalism. First, we discuss the results with the E-RMF(G2) formalism.

Fig. 4.4 shows the results of our calculation for different He and Li projectile masses with fixed targets as ^{208}Pb, ^{235}U and ^{230}Th. In all of these cases, the total nuclear reaction cross section increases with the increase in mass of the projectile. At the relatively lower incident energy (30 to 200 MeV/nucleon) of the projectile nucleus, the nuclear total reaction cross section is maximum and it decreases rapidly with the increase of energy and, in all cases, a minimum in σ_r occurs at about 400 MeV/nucleon. As the incident energy is further increased, the nuclear total reaction cross section increases slightly and takes an almost constant value, which continues till the energy of the incident particle is 1000 MeV/nucleon. Note that, in our calculations

for heavier target masses, the medium modification is considered, which implies the probability of the formation of a heavier mass nucleus with the increase of mass number of the projectile as well as the target.

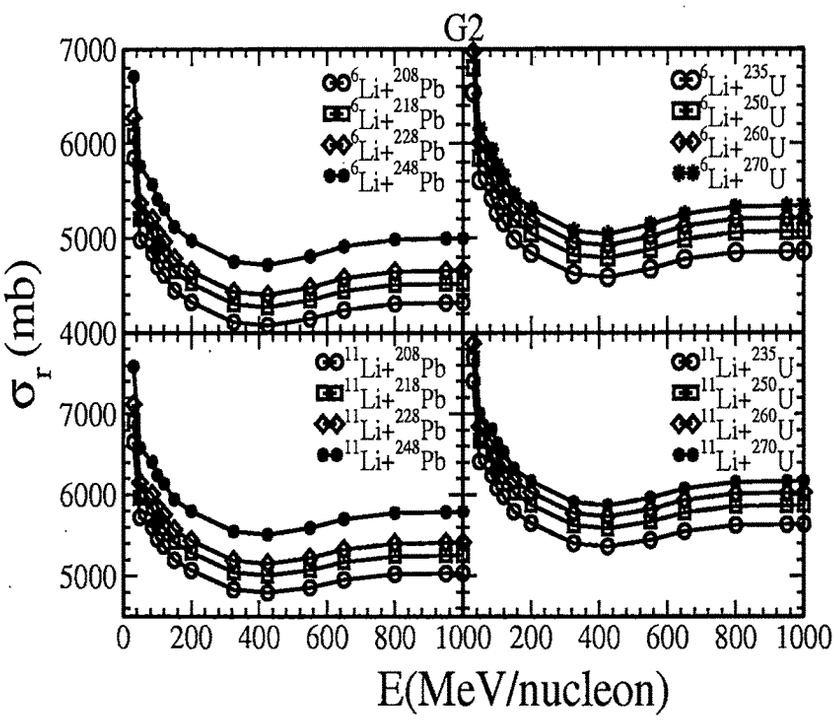

Figure 4.8: Same as Fig. 4.4, but for Li nuclei as projectiles with different isotopes of Pb and U as targets.

Fig.4.6 shows the total reaction cross sections for He, B and C as projectiles with Th, U, Pb as targets. Unlike Fig.4.4, here the projectile is fixed and the mass of the target changes. We find that here also the total nuclear reaction cross section increases with the increase of target mass. For example, σ_r for ^{270}Th is much more than the σ_r for ^{230}Th, with the same ^{4}He as projectile. Similarly, Fig. 4.8 demonstrates the results of our calculations for a fixed projectile with variable target masses in the cases of ^{6}Li+^{208,218,228,248}Pb, ^{6}Li+^{235,250,260,270}U, and ^{11}Li+^{208,218,228,248}Pb, ^{11}Li+^{235,250,260,270}U. Irrespective of a stable or unstable system, the total nuclear reaction cross section

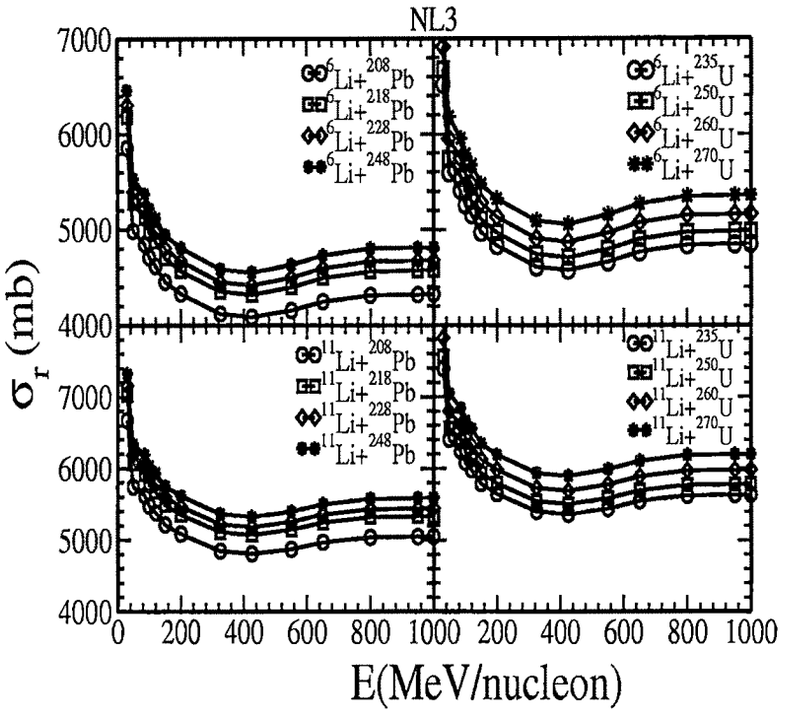

Figure 4.9: Same as Fig. 4.8, but for RMF(NL3) formalism.

increases with increase of either the target mass A_t or the projectile mass A_p or both. This increase in total nuclear reaction cross section can be related to the geometrical area of the nucleus πR^2, where R is the sum of the radii of the target and the projectile nuclei. The nuclear radius is connected with the mass number of the nucleus via the relation $R = r_0 A^{1/3}$, where $r_0 = 1.36$ fm, and hence one expects $\sigma_r \propto (A_t^{1/3} + A_p^{1/3})^2$. Bradt and Peters [199] modified this relation to take into account the deviations from the experimental systematics and expressed it as $\sigma_r = \pi r_0^2((A_t^{1/3} + A_p^{1/3} - b_0)^2$. This formula is further improved in Ref. [200, 201] and, later on, the Coulomb correction was also included [202, 203]. Recently, the semi-empirical formula for calculating the total nuclear reaction cross section [181, 182] and experimental measurements

[204, 205] also show the size dependence of σ_r via the masses of target and projectile nuclei [204, 205].

Summarizing the results of Figs. 4.4, 4.6 and 4.8 for some representative reactions, we find that the total nuclear reaction cross section increases with the increase of either the projectile or target mass or both. Also, the maximum value of σ_r occurs at a particular energy per nucleon, irrespective of the mass of the target or projectile. Interestingly, the same conclusions are presented by Figs. 4.5, 4.7 and 4.9 for RMF(NL3), showing the force independence of the above results. From the behavior of our calculated total nuclear reaction cross section σ_r, the most important inference for the formation of superheavy elements that can be drawn is the following: from the increase in σ_r that occurs at a particular incident energy, we can conclude that the formation of a superheavy element is possible in some astrophysical accreting objects, such as the relativistic jets of $\gamma - rays$ bursts (GRBs) or supernovae jets near the nascent neutron star [178, 206, 207, 208].

4.2.4 Differential elastic scattering cross sections

Evaluation of the differential elastic scattering cross section $\frac{d\sigma}{d\Omega}$ is crucial to the studying scattering phenomenon. The results of our calculations for C+U and Li+Pb systems at various incident energies are displayed in Figs. $4.10 - 4.14$, and the extension of this calculation to the newly claimed to be discovered $^{292}X_{122}$ nucleus with the halo nucleus ^{11}Li taken as the projectile, in Fig. 4.15 in next subsection. Figure 4.10 compares the calculated results with the experimental data [209] for the ^{12}C+^{208}Pb system at two incident energies of 120 and 200 MeV/nucleon. Our calculations are carried out using both the E-RMF(G2) and RMF(NL3) formalisms, and they match the data reasonably well near the zero scattering angle. However, the discrepancy with the data increases as the scattering angle increases beyond a zero value.

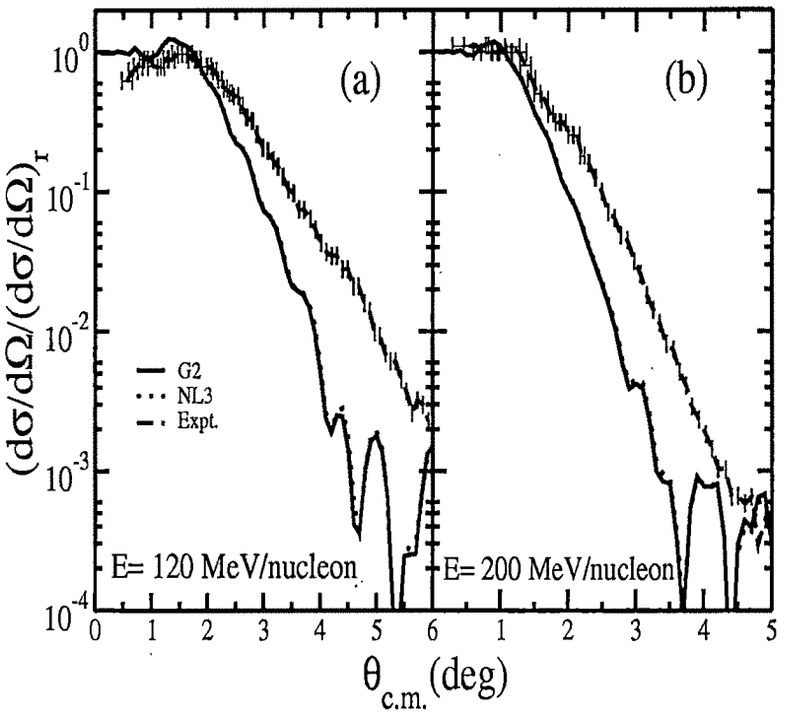

Figure 4.10: Comparison of the experimental differential elastic scattering cross section with results of E-RMF(G2) and RMF(NL3) formalisms for $^{12}C + ^{208}Pb$ reaction at incident energies of (a) 120 and (b) 200 MeV/nucleon. The experimental data, shown with error bars, are from Ref. [209].

In general, the calculated $\frac{d\sigma}{d\Omega}$ for the two formalisms are similar and show a qualitative agreement with the data. A further inspection of Figs. 4.10(a) and 4.10(b) shows that the calculated $\frac{d\sigma}{d\Omega}$ provide a better agreement with the data at higher incident energy. In other words, the calculated result is closer to the data for E = 200 than for E = 120 MeV/nucleon. Figures 4.11 and 4.12 show similar calculations for the ^{12}C+^{250}U system at the energies 30, 85, 120, 200, 325, 550, 800, and 1000 MeV/nucleon for, respectively, the E-RMF(G2) and RMF(NL3) densities. We notice in Figs. 4.11 and 4.12 that the $\frac{d\sigma}{d\Omega}$ for the system ^{12}C+^{250}U show a large variation with incident energy. Interestingly, the results obtained by using the two formalisms,

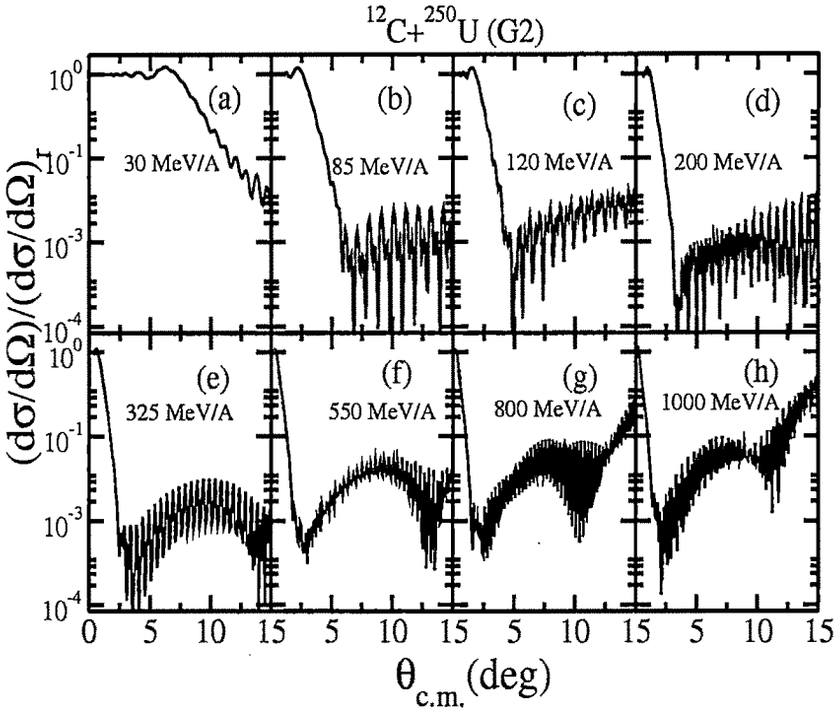

Figure 4.11: Differential elastic cross section for $^{12}C+^{250}U$ at different energies, using the E-RMF(G2) formalism.

E-RMF(G2) and RMF(NL3), are almost identical, and hence force-independent, for the entire energy range of 30-1000 MeV/nucleon over the large spectrum of angular distribution, starting from 0^0 up to 15^0. The typical, Fresnel type, diffraction effect appears in the small-angle region (5^0-10^0) for C+U system at 30 MeV/nucleon, which is due to the interference of Coulomb and nuclear amplitudes. On the other hand, the oscillatory behavior of the elastic scattering cross section at large scattering angles, as well as at higher incident energy per nucleon, could possibly be an artifact of some numerical instability of our calculations. However, we have thoroughly checked our calculations for the various inputs, such as the number of points in the Monte Carlo integration method, etc., and find that the observed oscillations are perhaps real.

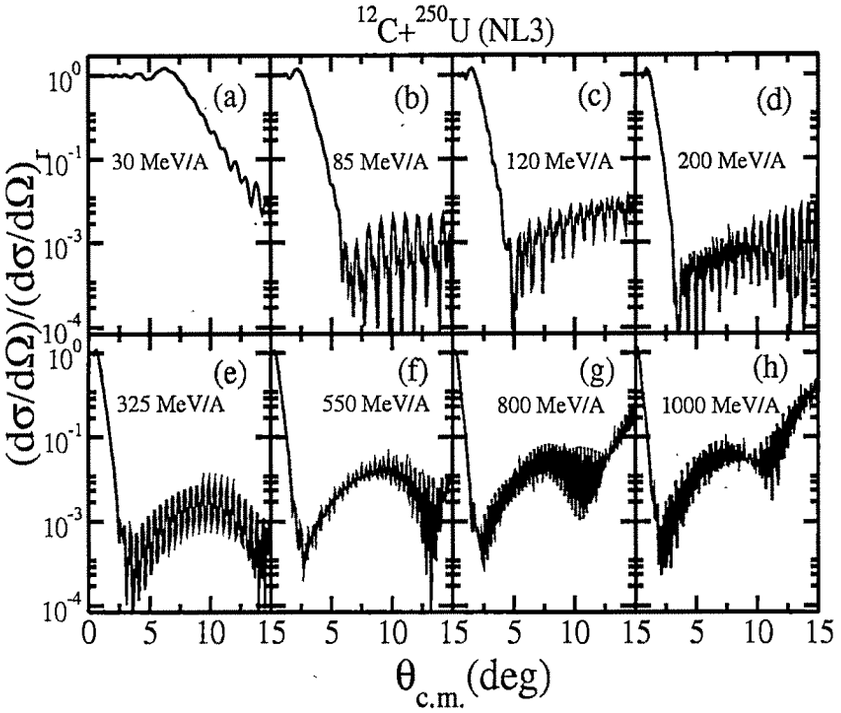

Figure 4.12: Same as Fig. 4.11, but for the RMF(NL3).

Figures 4.13 and 4.14 give our results for some selected cases at two incident energies of 30 and 1000 MeV/nucleon. The systems chosen at 30 MeV/nucleon are (^{12}C+^{235}U, ^{12}C+^{250}U), (^{12}C+^{235}U, ^{20}C+^{235}U) and (^{12}C+^{238}U, ^{20}C+^{250}U), and at 1000 MeV/nucleon are (^{6}Li+^{208}Pb, ^{6}Li+^{260}Pb), (^{6}Li+^{208}Pb, ^{11}Li+^{208}Pb), and (^{6}Li+^{210}Pb, ^{11}Li+^{260}Pb). Apparently, in Fig. 4.13, the differential elastic scattering cross section for C isotopes with different masses of U nuclei at 30 MeV/nucleon of the projectile energy constitute cases of stable+unstable unstable+stable, stable+stable and unstable+unstable projectile-target systems. The left panel of the figure is for E-RMF(G2) and right one for RMF(NL3). We notice in Fig. 4.13 that, for all cases, the $\frac{d\sigma}{d\Omega}$ is similar in magnitude for both stable and unstable systems at small scattering angles. However, a significant increase in the differential elastic scattering cross section ap-

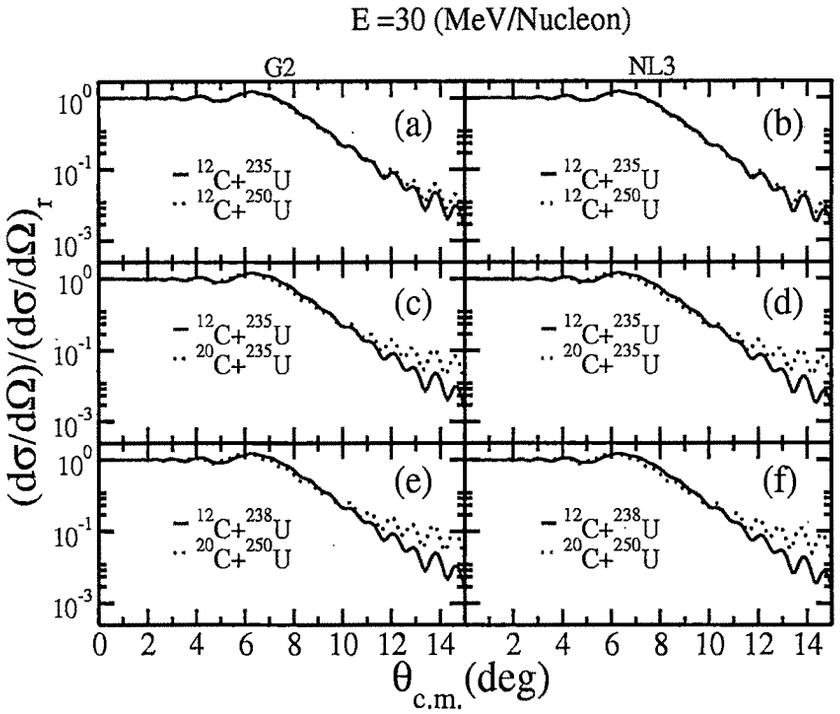

Figure 4.13: Differential elastic scattering cross sections, taking C isotopes as projectiles with different isotopes of U as targets, for E-RMF(G2)(left) and RMF(NL3)(right) formalisms.

pears for heavier isotopes with the increase of scattering angle θ. This phenomenon is more conspicuous for high-energy scattering, as shown in Fig. 4.14 for different combinations of Li and Pb nuclei.

4.2.5 Applications to recently discovered superheavy elements

Recently, the superheavy nucleus with Z=122 or 124 and mass number A= 292 is possibly discovered in natural Th, using inductively coupled plasma sector field mass spectroscopy [179]. The estimated half-life of this isotope is $T_{1/2} \geq 10^8$ years, which is in good agreement with the theoretical predictions [77, 210, 211, 212, 213]. Therefore, taking this newly discovered nucleus as a target, it is interesting to study the total

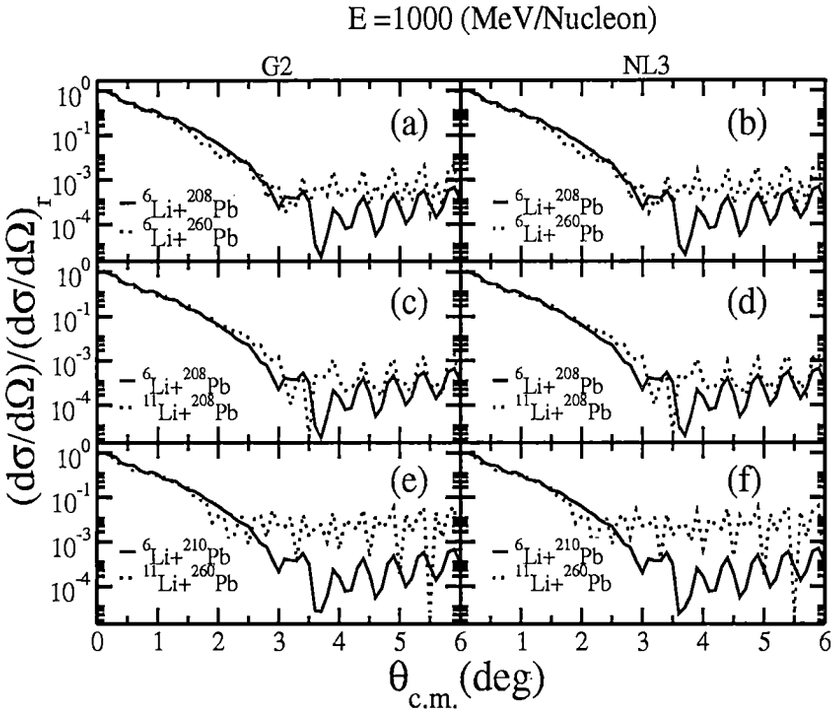

Figure 4.14: Same as Fig. 4.13, but taking Li isotopes as projectiles with different isotopes of Pb nuclei as targets.

nuclear reaction and elastic differential cross sections, with a highly neutron-rich nucleus like ^{11}Li as the projectile.

Fig. 4.15 shows σ_r and $\frac{d\sigma}{d\Omega}$ for the systems $^{11}Li+^{292}X_{122}$ and $^{11}Li+^{320}X_{122}$, using both E-RMF(G2) and RMF(NL3) methods. We notice from this figure that, just as before, σ_r increases with mass of the target and the magnitude of $\frac{d\sigma}{d\Omega}$ increases with scattering angle. The oscillations in elastic differential cross section increase with the increase of mass number of the target nucleus. This scenario resembles the phenomenon observed above for known heavy elements like Pb and U in Figs. 4.10 and 4.11.

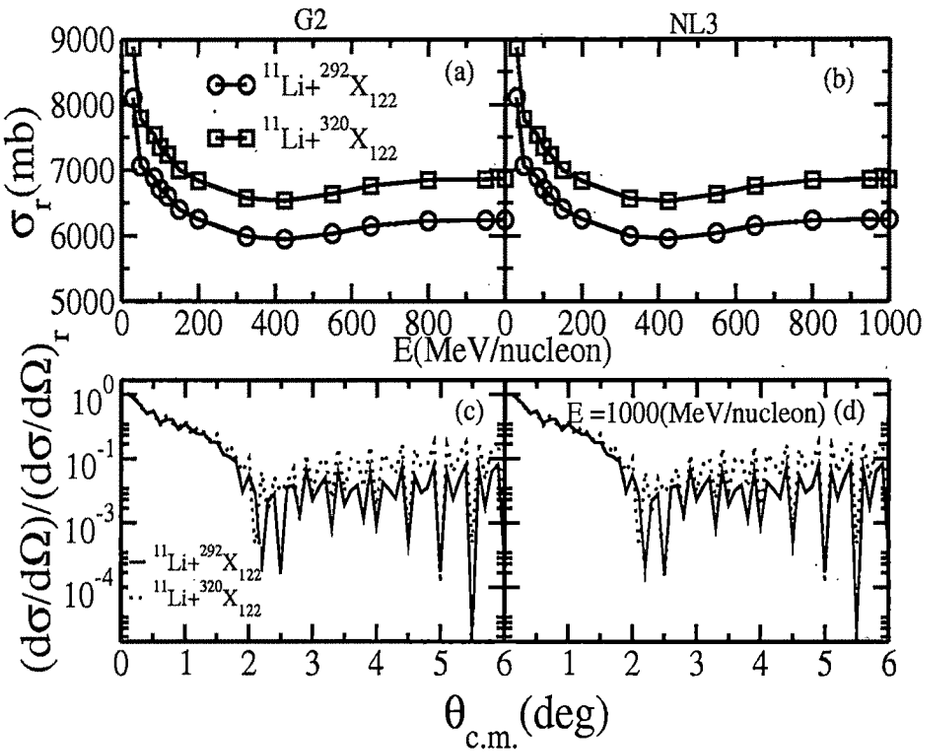

Figure 4.15: Total nuclear reaction cross sections and differential elastic scattering cross sections, for ^{11}Li taken as projectile with the isotopes $^{292,320}X_{122}$ as targets.

4.3 Conclusions

We have used the Glauber model for calculating the total nuclear reaction cross sections with densities obtained from RMF and E-RMF formalisms. After showing that the calculations of total nuclear reaction cross sections performed with the Glauber model, using RMF and E-RMF nuclear densities as the ingredients, match the measured data nicely, we have extended its applications to the recently predicted neutron-rich, thermally fissile Uranium and Thorium isotopes. We have shown that the total nuclear reaction cross sections decrease with the increase of incident energy of the projectile. In most of the cases, the neutron-rich light mass nuclei are used as projectile and heavy nuclei as targets. In order to see the effect of the neutron-

richness of the projectile in the exotic mass region, we repeated the calculations with various projectile masses without changing the target nucleus. We found that the total nuclear reaction cross section increases with increase of the projectile mass or with increase of neutron number of the target. Such a result is valid for both the normal and neutron-rich nuclei. Thus, our framework seems ideal for the simple analysis of the different ranges of data on total nuclear reaction cross sections of neutron-rich unstable nuclei. However, unlike the total nuclear reaction cross sections, the elastic differential scattering cross sections show marginal changes with the change of projectile mass.

Specifically, we have calculated the total nuclear reaction cross section σ_r and the elastic differential scattering cross section $\frac{d\sigma}{d\Omega}$ for both the increasing projectile and target masses. In all cases, we find that σ_r increases with target mass. Analysing the elastic differential scattering cross section, however, we find that the magnitude of $\frac{d\sigma}{d\Omega}$ increases with scattering angle and it is more prominent at high incident energy per nucleon of the projectile nucleus. Similar to total nuclear reaction cross section, elastic differential cross section also shows greater sensitiveness with increase of mass number of the target. Application of the model to the recently discovered superheavy element Z=122 or 124 is interesting because of the possibility of the formation of the highly neutron-rich superheavy element in earth crust.

Chapter 5

One nucleon removal reactions

5.1 Introduction

For more than two decades, the exploration of neutron-rich nuclei is an important branch in Nuclear Physics research. It is a source of observations of new phenomena and dynamics. This is possible due to the development of accelerator techniques for beams of radioactive nuclei in various laboratories around the globe. Experimental methods and theoretical analysis have been widely used to collect information about the structure, such as nuclear size, valence nucleon distribution and halo structure of these exotic nuclei. The measurement of various reaction observables like total reaction cross section σ_r, one- and two- nucleon removal cross section (σ_{-1n}, σ_{-2n}) and the longitudinal momentum distribution $P_{||}$ are some of the established quantities for such studies.

Unlike Chapter 3 and 4, the relativistic mean field (RMF) or the effective field theory motivated RMF (E-RMF) provides the internal structure or sub-structure information of the nuclei through density distributions, which are used as input while calculating the observables in conjunction with Glauber model [178, 185, 214, 215]. A systematic study of one- and two-neutron knockout data for $^{15-19}$C, explained beautifully while using shell model, which gives a consistent structure information not only for the stable nuclei but also for nuclei at the boundary [216]. It is well known

that narrow fragment momentum distribution reflects large spatial distribution of the valence nucleon and also there is a correlation between the magnitude of σ_{-1n} with the width of the $P_{||}$, as one approaches the nucleon (neutron or proton) drip-lines. However, one-neutron removal reaction cross sections provide important information on nuclear structure which is complementary to that obtained from $P_{||}$.

The formation of halo in a nucleus near the drip-line is due to the very small binding of the valence particles. The quadrupole deformation of the halo is determined by the structure of the weakly bound valence orbital and it does not depend on the shape of the core [217]. On the other hand existance of two nucleon halo is most unlikely in a deformed nucleus [218]. It is shown by Nunes [218] with a variety of 3-body NN tensor force which goes beyond the unusual pairing in Hartree-Fock-Bogoliubov (HFB) and the coupling due to core deformation/polarization significantly reduce the formation of 3-body Borromean systems. In a recent work [219] halo phenomena in deformed nuclei are analysed within deformed Relativistic Hartree Bogoliubov (RHB) theory and their finding in weakly bound ^{44}Mg nucleus indicates a decoupling of the halo orbitals from the deformed core agreeing with the conclusion of Ref. [217].

In the present chapter, our aim is to calculate the σ_r and σ_{-1n} in the Glauber model by using both spherical and deformed densities obtained from the RMF and E-RMF formalisms [178, 185, 214, 215]. The results obtained from our calculations are discussed in Section 5.2. In this Section we intend to study the applicability of Glauber model in the context of both stable and drip-line nuclei particularly those with halo structure. We would also like to estimate the difference in the total reaction cross sections of two neighboring nuclei with mass numbers A and A-1 in an isotopic chain to justify the applicability of Glauber model. Here, it will be shown for the drip-line nuclei with a halo-structure, the cross sections are not explained by the standard evaluation of σ_{-1n}. Rather to this estimation, the difference in total reaction cross

section between two consecutive neighboring nuclei in an isotopic chain better matches with the experimental data. Finally, a brief summary and concluding remarks are given in the last Section 5.3.

5.2 Details of the Calculations and Results

We obtain the field equations for nucleons and mesons from the RMF and E-RMF Lagrangian. For the deformed case (RMF only), these equations are solved by expanding the upper and lower components of the Dirac spinners and the boson fields in an axially deformed harmonic oscillator basis. The set of coupled equations are solved numerically by a self-consistent iteration method taking different inputs of the initial deformation β_0 [41, 47, 105, 220]. For spherical densities, we follow the numerical procedure of Refs. [123, 125] for both RMF and E-RMF models. The centre-of-mass motion (c.m.) energy correction is estimated by the usual harmonic oscillator formula $E_{c.m.} = \frac{3}{4}(41A^{-1/3})$.

Comparing the binding energy (BE) of the calculated solutions, the maximum BE and the corresponding densities [ρ_p (proton) and ρ_n (neutron)] are for the ground state. All other solutions are the excited intrinsic state including the spherical one. Since the main input in the Glauber model estimation is the RMF or E-RMF densities, it is important to have information about these quantities. We have plotted the spherical ρ_p and ρ_n for both proton and neutron of Carbon and Boron isotopes in Fig. 5.1 using RMF (NL3) parameter set [112]. As expected, we find an extended density distribution for proton compared to neutron in case of ^{9}C and ^{8}B due to the proton-rich nature of these two nuclei. The value of ρ_n and ρ_p are almost similar for ^{12}C which can be seen from Fig 5.1. Extension of ρ_n is much more than ρ_p for rest of the nuclei. It is maximum for ^{19}C and ^{15}B in Carbon and Boron isotopic chains, respectively, because of high neutron to proton ratio for these cases.

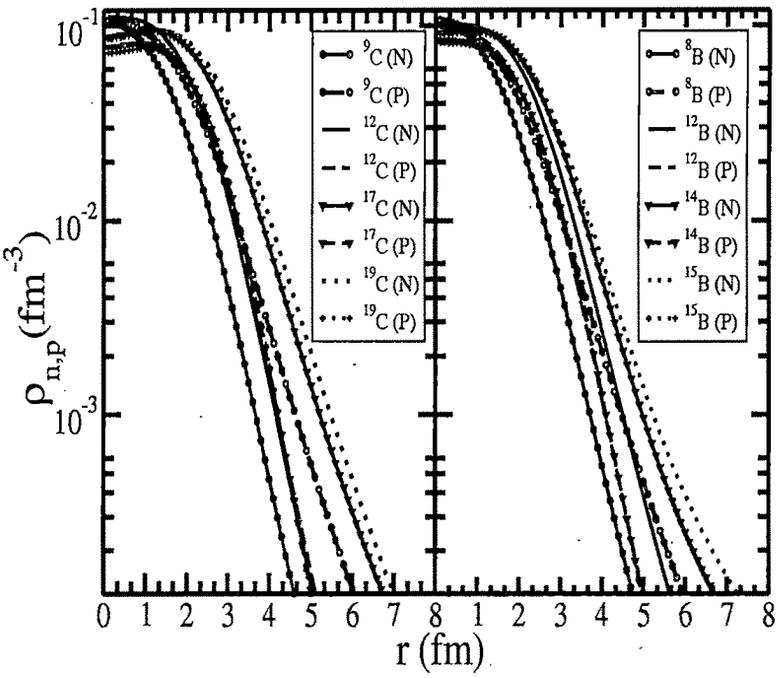

Figure 5.1: The spherical proton (ρ_p) and neutron (ρ_n) density obtained from RMF (NL3) parameter set for various isotopes of (a) Carbon and (b) Boron.

In the present study of σ_r and σ_{-1n}, we use first the spherical density obtained from RMF (NL3) [112] and E-RMF (G2) [113]. The results are presented in Table 1 for $^{9,12,13,15,17,19}C$ and $^{8,12,13,14,15}B$ isotopes with ^{12}C−target at various projectile energies. These results deviate considerably from the data [221, 222, 223, 224, 225] which are quoted in the table. For example, in case of ^{9}C+^{12}C, the observed value of σ_{-1n} is 48±8 mb as compared to the estimated results of 81 and 96 mb with NL3 and G2 parametrization, respectively. Note that the σ_{1n} for ^{8}B+^{12}C and ^{9}C+^{12}C systems are one-proton removal reaction cross section, which may be followed throughout the text and Tables. However, in rest of the systems, σ_{1n} will be referred as one-neutron removal reaction cross section Similar discrepancy is also seen for other cases.

Table 5.1: One-neutron- for $^{12,13,15,17,19}C$ and one-proton removal reaction cross sections σ_{-1n} (in mb) for ^{9}C and ^{8}B with ^{12}C–target using spherical RMF and E-RMF densities obtained from NL3 and G2 parameter sets, respectively. The available experimental data [221, 222, 224, 225] is given for the comparison. The last occupied proton and neutron single-particle energies are also given. The energy per nucleon E_{lab}/A and binding energy (BE) are in MeV. The experimental BE is taken from [166].

Projectile	Energy	σ_{-1n}	$\sigma_{-1n}(I)$		$\sigma_{-1n}(II)$		$\epsilon_p(MeV)$		$\epsilon_n(MeV)$	
		Exp.	RMF	E-RMF	RMF	E-RMF	RMF	E-RMF	RMF	E-RMF
^{9}C	285	48(8)	81	96	34	31	-4.07	-4.15	-13.81	-13.90
^{12}C	1050	44.7(3)	39	37	55	39	-15.66	-13.16	-18.97	-16.16
^{13}C	800		29	28	47	37	-16.81	-15.30	-17.77	-16.35
^{15}C	54	137(16)	95	88	37	38	-19.18	-20.47	-10.57	-10.39
^{17}C	904	129(22)	101	95	45	32	-23.93	-22.65	-11.53	-11.57
^{19}C	910	231(51)	134	128	35	37	-27.25	-25.89	-12.61	-12.50
^{8}B	285	89(2)	103	107	47	33	-23.16	-20.73	-31.50	-28.96
^{12}B	67	81(5)	54	49	47	44	-39.95	-34.18	-14.20	-13.49
^{13}B	57	59(4)	54	38	46	43	-39.88	-35.49	-7.81	-7.85
^{14}B	50	153(15)	70	64	48	38	-41.00	-36.85	-8.40	-8.41
^{15}B	43	108(13)	87	89	51	39	-42.16	-38.23	-8.77	-8.96

A further inspection of the table shows that the experimental one-neutron removal reaction cross sections for some selected cases agree well with the prediction. We have also used the method of Abu-Ibrahim et al. [133] to calculate the one-neutron removal reaction cross section $\sigma_{-1n}(II)$. These are obtained by the difference of total reaction cross section of two neighboring nuclei with mass number A and A-1 in an isotopic chain. This prescription is suitable only for halo projectiles and may not be applicable for general cases. The expression is given by [133]:

$$\sigma_{-1n}(II) = \sigma_r(^{A}Z) - \sigma_r(^{A-1}Z), \tag{5.1}$$

and the values are given in Table 5.1 for comparison. The $\sigma_{-1n}(II)$ differs significantly from the experimental data for all the cases. It is important to recall that the effect of deformation is nominal in the evaluation of σ_r which is reported in our earlier publications [178, 185, 214, 215]. In these papers, the Glauber model with RMF(NL3, NL-SH) and E-RMF(G2) densities show good agreement with experimental data for σ_r and differential elastic scattering cross sections $d\sigma/d\Omega$, which in general justify the model independency of the calculation with various relativistic parameterizations. Unlike the total reaction cross section, the σ_{-1n} obtained from the Glauber model depends very much on the structure information of the projectile and target nuclei, i.e., input densities of these systems.

The nuclear single-particle energy $\epsilon_{n,p}$ for the last occupied orbit is very important for a reaction process. Thus, it is worth while to analyse the $\epsilon_{n,p}$ of the valence nucleon of the projectile and target nuclei. For simplicity, the spherical single-particle energy for the last occupied orbit for proton ϵ_p and neutron ϵ_n with RMF (NL3) and E-RMF (G2) are compared. As expected, a small variation in ϵ_p or ϵ_n makes a remarkable change in $\sigma_{-1n}(II)$ [Eq. (5.1)] for many cases. For example, the one neutron removal reaction cross section $\sigma_{-1n}(II)$, for $^{12}C + ^{12}C$ are 55 and 39 mb for RMF (NL3)

and E-RMF (G2) with their single-particle energies $\epsilon_p = -15.66$, $\epsilon_n = -18.96$ and $\epsilon_p = -13.16$, $\epsilon_n = -16.16$ MeV, respectively. This discrepancy is minimum in the calculation of $\sigma_{-1n}(I)$ [Eq. (2.89) of Chapter 2] with a lone exception for $^{13}B + ^{12}C$ system. As the valence $\epsilon_{n,p}$ plays a major role to determine the reaction observables, one needs to reproduce these values with the experimental observation. This can be achieved by a small adjustment of the parameters in the relativistic mean field formalisms. However, the philosophy of RMF or E-RMF of single set of parametrization for the entire domain of nuclear landscape goes against this parameter fiddling. Keeping this in mind, the quality of the results is compromised slightly using the original values of NL3, NL-SH or G2 sets.

In general, the single-particle energy of neutron levels ϵ_n of a valence orbital increases (absolute value decreases) in an isotopic chain while approaching towards the drip-line. However, this normal trend does not satisfy exactly for extremely neutron-rich nuclei. To justify this statement, one can quote the experimental instability of ^{10}Li against the famous bound halo of ^{11}Li. Here the last occupied neutron of $(1p_{1/2})^1$ (^{10}Li unstable) has more ϵ_n than that of $(1p_{1/2})^2$ of ^{11}Li which is a loosely bound two neutron Borromean system. Similar situation occurs in the C and B isotopic chains which are supposed to be halo cases. The calculation of charge-changing cross section for C, N, O and F isotopes in the framework of continuum Hartree-Bogoliubov description clears this understanding [226]. This calculation gives binding energies of $1d_{5/2}$, $2s_{1/2}$ and $1d_{3/2}$ as -7.541, -4.087 and -0.8066 MeV in ^{24}O and -8.042, -4.795 and -1.874 MeV in ^{26}O. That means the valence neutron in ^{24}O is bound by 0.8066 MeV while the last neutron is 1.874 MeV bound in the heavier ^{26}O isotope.

Table 5.2: Same as Table 1, but using both spherical and deformed NL-SH densities for $^{9,12,15,17,19}C$ and $^{8,12,13,14,15}B$ projectiles taking ^{12}C as target. The available experimental data is also displayed for the comparison [221, 222, 224, 225]. The last occupied neutron and proton single-particle orbits are also given and it is denoted by the Nilsson index $[Nn_3\Lambda]\Omega^{\pi}$.

Projectile	Target	Energy	σ_{-1n}	$\sigma_{-1n}(I)$		$\sigma_{-1n}(II)$		β_2	neutron		proton	
			Exp.	Sph.	Def.	Sph.	Def.		$[Nn_3\Lambda]$	$\epsilon_n(MeV)$	$[Nn_3\Lambda]$	$\epsilon_p(MeV)$
^{9}C	^{12}C	285	48(8)	70	66	24	03	0.36	$[110]1^-$	-16.122	$[101]3^-$	-2.772
^{12}C	^{12}C	1050	44.7(3)	39	49	45	293	-0.21	$[101]1^-$	-16.952	$[101]1^-$	-13.752
^{15}C	^{12}C	54	137(16)	92	130	35	15	0.25	$[220]1^+$	-2.611	$[101]3^-$	-19.631
^{17}C	^{12}C	904	129(22)	122	120	31	32	0.45	$[211]3^+$	-2.705	$[101]3^-$	-21.906
^{19}C	^{12}C	910	233(51)	134	152	31	263	-0.43	$[202]3^+$	-3.316	$[101]1^-$	-27.048
^{8}B	^{12}C	285	89(2)	101	99	34	10	0.63	$[110]1^-$	-14.054	$[101]3^-$	-1.880
^{12}B	^{12}C	67	81(5)	41	65	45	70	0.18	$[101]1^-$	-6.212	$[101]3^-$	-15.585
^{13}B	^{12}C	57	59(4)	53	46	44	16	0.10	$[110]1^-$	-7.378	$[101]3^-$	-18.321
^{14}B	^{12}C	50	153(15)	67	97	32	15	0.38	$[220]1^+$	-1.992	$[101]3^-$	-18.686
^{15}B	^{12}C	43	108(13)	88	104	68	73	0.59	$[220]1^+$	-2.611	$[101]3^-$	-19.631

Again in the present calculation spherical cases (see Table 5.1) the valence neutron in ^{14}B is unbound by 0.42 MeV and it is very loosely bound ($\epsilon = -0.04$ MeV) for ^{15}B. This is because of the spherical excited intrinsic solution. Actually, ^{14,15}B are highly deformed in the ground state (see Table 5.2) and a real situation can be achieved only in the deformed calculations. Apart from the single-particle energy, the structure effect of the participating nuclei is crucial for a reaction study. In this context, it is interesting enough to see this effect (deformation effect) on σ_{-1n}. We repeat the calculations for $\sigma_{-1n}(I)$ and $\sigma_{-1n}(II)$ with the deformed densities (RMF only) as input in the Glauber model [185, 214]. We obtain spherical equivalent of the axially deformed densities following the prescription of Refs. [178, 185, 214, 215]. The NL-SH parameter set [50] for this purpose is used and the results are listed in Table 5.2. The binding energies (BE) obtained by NL-SH parameter set are compared with the experimental data [166]. The calculated BE slightly over-estimate the experimental values except ^{12}C. However, this theoretical over-binding is small and may be due to the application of mean field for light mass nuclei. To get a qualitative estimation of the binding energies, the deformed RMF with NL-SH set is trustworthy and can be used for further calculations in this mass region of the periodic table. The reason to change the NL3 to NL-SH is the unavailability of converged ground state deformed solution with NL3 for very light mass nuclei [106]. Also, the NL-SH parametrization is reasonably a good parameter set for these neutron-rich nuclei.

Due to similar reason as mentioned for the spherical nuclei, the deformed densities for some selected cases are imperative to analyse. Our earlier work on density study given us enough signature about the complicated sub-structure [158]. The clustering and sub-structure of these deformed neutron and proton density distributions are demonstrated in Fig. 5.2. The density contours presented are in boxes of width and height 6 fm each. A uniform contour spacing of 0.01 fm^{-3} is used for proton

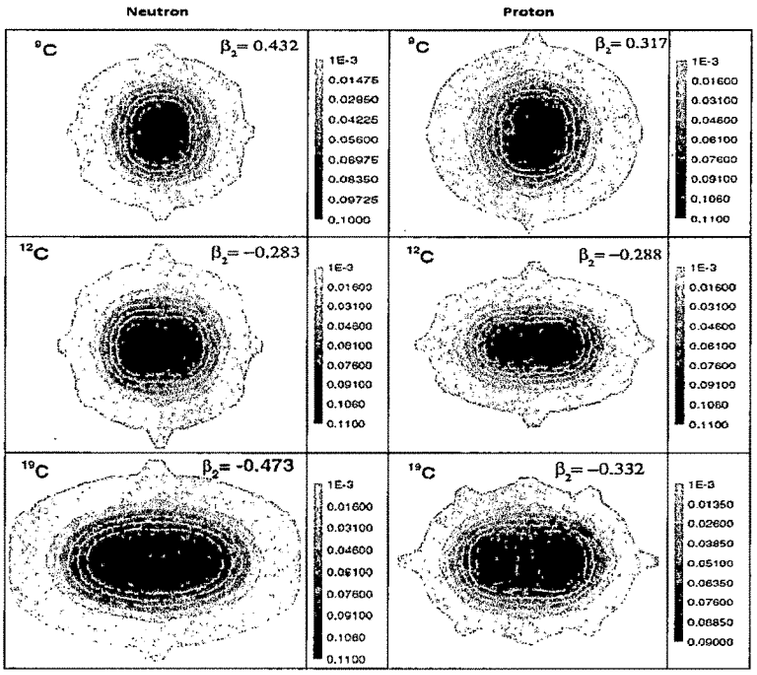

Figure 5.2: The axially deformed density distribution for ^{9,12,19}C with RMF (NL-SH) parameter set.

and neutron densities. The z-axis is chosen as the symmetry axis, the densities are evaluated in the $z\rho$ plane, where $\sqrt{x^2+y^2} = \rho$. In ref. [158], it is noticed that ^{12}C possesses a $3\alpha-$ cluster with a tetrahedral configuration. The same structure is reproduced in the present study with an oblate shape. The structure of the neutron deficient ^{9}C nucleus has a prolate ground state and that of the neutron-rich ^{19}C has an oblate ground state deformation. In all the three cases, the density plots show that the central part of the nucleus is a compact core, which is surrounded by a thin layer of nucleons. The structure of the internal core for both proton and neutron have different density distribution from ^{9}C to ^{19}C. The shape of ^{19}C proton density distribution looks like a dumb-bell. Thus, it has a maximum probability to have the structural effects on neutron removal reaction. On the other hand, the total

nuclear reaction cross section is less influenced by deformation, may be because of the averaging in input density in the Glauber model calculations.

The results obtained from the deformed densities are tabulated as Table 5.2. It shows that most of the $\sigma_{-1n}(I)$ [obtained from Eq. (2.89) of Chapter 2] matches quite well with the experimental data of [221, 222, 223, 224, 225] and only a few of them do not agree. On the other hand, σ_{-1n} evaluated from Eq. (5.1) coincide with only $^{19}C+^{12}C$ experimental data [221]. Among the nuclei investigated here, ^{14}B and ^{19}C with relatively weak binding of the valence neutrons are of particular interest. Measurements of one neutron removal cross sections have suggested these two nuclei to be one neutron halo systems [227]. The single-particle energies for proton ϵ_p and neutron ϵ_n for the last occupied orbit, are given in the 12th and 14th column of Table 5.2 respectively. The last proton for ^{8}B and ^{9}C and the outer most neutron for $^{14,15}B$ and $^{17,19}C$ are loosely bound which are possible candidates for proton-halo (skin) or neutron-halo (skin). Going back to the analysis of Fig. 5.2, we see enough indication for the absence of halo-like structure in ^{9,12}C. Contrary to the case of ^{9}C and ^{12}C a thin-layer of neutron distribution spreads spatially to a large extent in case of ^{19}C, which looks like a halo-nucleus. This behavior is also reflected in the one neutron removal reaction cross section. In this particular case of ^{19}C, the calculated result $\sigma_{-1n}(II) = 263$ mb is closer to the experimental value of $\sigma_{-1n} = 233 \pm 51$ mb than the σ_{-1n} obtained by using Eqn. (2.89) of Chapter 2 [221, 222, 223]. According to Abu-Ibrahim et al. neutron removal reaction cross section of ^{14}B is larger than its neighbors, suggesting a weak binding of the last neutron (Table 5.2, $\epsilon_n = -1.992$ MeV) and extended valence density distribution [227].

Summarising the whole discussion of Tables 5.1 and 5.2, in general, one can say that except for a few cases like ^{12,17}C+^{12}C and ^{8,13}B+^{12}C the spherical density used from RMF (NL3) and E-RMF (G2) fails to reproduce the data. When we use the

deformed densities to evaluate the one neutron cross section, the predicted $\sigma_{-1n}(I)$ matches reasonably well with the experimental measurement. In this case, only the result of the system ^{19}C+^{12}C deviate from the observation. However, the results predicted by Eq. (5.1) disagree largely with the experiments irrespective of the densities used. In contrast to Eq. (2.89) of Chapter 2, the $\sigma_{1n}(II)$ matches with the lone case of ^{19}C+^{12}C and this agrees with the prediction of Ref. [133].

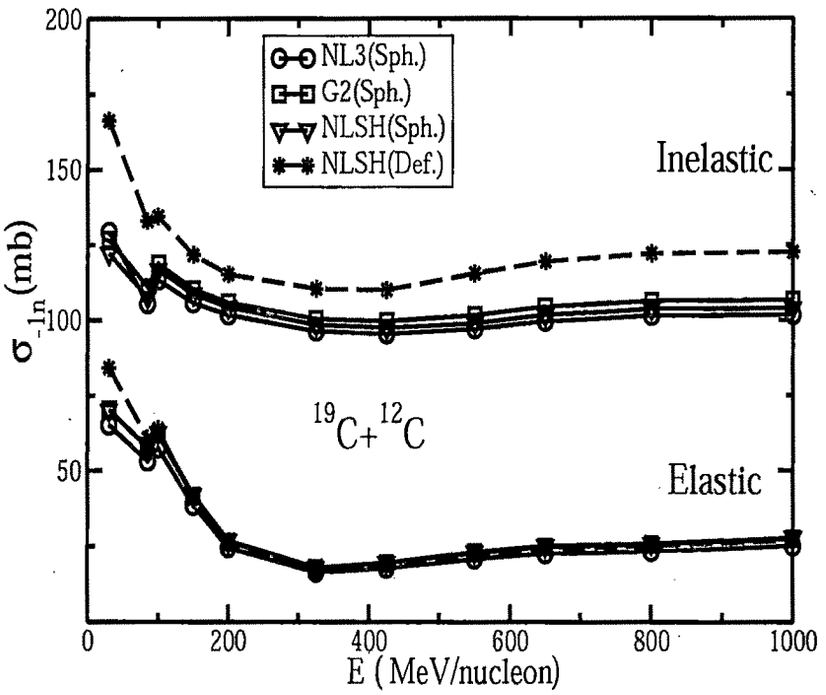

Figure 5.3: The energy dependence of the neutron removal cross section for ^{19}C+ ^{12}C system using spherical densities of RMF (NL3), RMF (NL-SH) and E-RMF (G2) parameter sets for both elastic and inelastic processes. The result obtained by deformed RMF (NL-SH) densities is also given for the comparison.

In Fig. 5.3, we have presented the $\sigma_{-1n}(I)$ with various incident energies for ^{19}C +^{12} C using the spherical NL3, NL-SH and G2 densities in the Glauber model calculation. We also compare our results with the deformed NL-SH densities obtained from the axially deformed RMF. All the spherical densities give similar elastic (σ^{el}_{-1n})

and inelastic (σ^{iel}_{-1n}) one neutron removal reaction cross sections. The deformed NL-SH densities have a large effect on the evaluation of σ_{-1n} unlike to the total nuclear reaction cross section σ_r. This is evident from Fig. 5.3 and consistent with $\sigma_{-1n}(I)$. The deformed σ^{iel}_{-1n} values are always larger than the spherical σ^{iel}_{-1n} starting from low to very high incident energy of the projectile.

5.3 Conclusions

In summary, one neutron removal reaction cross sections for the neutron-rich isotopes have been calculated in the Glauber model using the densities obtained from RMF (NL3) and E-RMF (G2) for spherical and NL-SH parameter set for deformed nuclei. The dependence of σ_{-1n} on single-particle energy of the last occupied nucleon is seen in our present calculations. Although the total nuclear reaction cross sections do not show a significant difference, the σ_{-1n} values differ from each other for NL3 and G2 parameter sets. The σ_{-1n} are in good agreement with the experiments, when we consider the deformation effect in the densities. The Glauber model fails for halo systems and in this case ^{19}C+^{12}C scattering is a typical example. However, the difference between the total reaction cross section from the consecutive nuclei is reasonably reproduced in $\sigma_{-1n}(II)$. It is also concluded in the present chapter that deformation effect for one neutron removal cross section is important unlike the total reaction cross section σ_r. In other words, the Glauber model reproduces the experimental data reasonably well while considering the deformed densities for stable nuclei as projectiles. On the other hand, when we estimate the difference of reaction cross sections of nuclei with mass numbers A and that of A-1 in an isotopic chain, we get good agreement with the experimental data for the halo cases also.

Chapter 6

Formation of Superheavy Elements and Multifragmentation Fission

6.1 Introduction

Till date, Uranium is the known heaviest element found in nature. So far more than 26 elements have been synthesized in various laboratories. New elements with atomic number upto 100 were synthesized by subjecting Uranium to high neutron flux in a reactor. However, this method was not useful to synthesize more heavier elements because the newly formed elements decay (β^--decay) before they could capture another neutron. Then it was suggested to fly over the sea of instability in order to reach the island of stability in the superheavy region. This work has started by heavy ion reactions in many laboratories like GSI in Germany, Lawrence Berkley Laboratory in USA, JINR in Dubna, RIKEN laboratory in Tokyo etc. This approach was not suitable as the compound nucleus undergoes fission immediately because it remains in a highly excited state after formation. Then elements with Z = 107 - 112 are synthesized by cold fusion reactions but here the probability of formation of new elements falls exponentially as a function of atomic number of the compound nucleus. Furthermore, the new elements formed in cold fusion reactions contains relatively less number of neutrons than that of magic number [228]. Nuclei

with higher neutron number can be produced by using the isotope $^{48}Ca_{20}$ as projectile and neutron-rich isotopes of Plutonium, Americium, Curium, Californium etc in the hot fusion reaction. In this way elements with Z = 114-118 with N lying between 172 and 177 are synthesized. Thus we have got some experimental evidence for an island of stability for superheavy nuclei. But we are still far from the region with superheavy nuclei having lifetime of thousand years. We do not know yet how to synthesize superheavy nuclei with magic number N = 184 [228].

Thus formation of superheavy elements (SHE) in the laboratory is one of the most challenging problem in Nuclear Physics. So far the synthesis of Z=118 element has been possible [194]. Efforts are on to synthesize still heavier elements in various laboratories all over the world. It is certain that if an element is created through human efforts then probably it could be present naturally somewhere in the Universe. Thus the mode of formation of superheavy or super-superheavy element in astrophysical object is a fundamental question in the field of Nuclear Astrophysics. In this context, it is mandatory that the superheavy element with Z=118 and higher atomic numbers are present in the object like relativistic jets of $\gamma - rays$ bursts (GRBs) or supernovae jets near the nascent neutron star. It has been reported in Ref. [229], and the stability of the most stable superheavy elements could be as high as 10^9 years in some of the calculations [77, 94, 210, 212, 213].

Thermally Fissile Elements

In a recent study, Satpathy et al. [16, 17] claimed the neutron-rich U and Th-isotopes are thermally fissile and could release orders of magnitude more energy than ^{233,235}U or ^{239}Pu in a new mode of fission decay called *multi-fragmentation fission*, which happened frequently in astrophysical objects. These newly predicted thermally fissile elements are $^{246-264}$U and $^{244-262}$Th centering the neutron magic number N=164 in the

superheavy region. This is because of the excess number of neutrons in the neutron-rich thermally fissile isotopes. The excess neutrons are responsible to produce extra neutron fragments at the time of scission and emits few additional prompt neutrons along with the normal fission neutron (similar to the 2.5 neutrons of ^{235}U). The extra neutrons prompt the chain reaction which are vulnerable to thermal neutron fission and produce much more energy compared to ^{233,235}U or ^{239}Pu.

The aim of this chapter is two-fold (I) Since the production of heavier nuclei is crucial, to have an understanding of its synthesis, we have studied mode of formation of superheavy or super-super heavy elements. (I) To study the structural properties, such as the ground and highly deformed (fission) configuration of predicted thermally fissile nuclei using the relativistic mean field (RMF) formalism.

(a) Formation of Superheavy Elements in Astrophysical Objects

Unstable nuclei play an influential, and in some cases dominant role, in phenomena of the cosmos such as Gamma Ray Bursts. The direct study of stellar properties in ground-based laboratories has become feasible, due to the availability of RIBs; for example the study of ^{18}Ne induced neutron pick-up reaction could reveal information about the exotic ^{15}O+^{19}Ne reaction occurring in the CNO cycle in stars. Study of the structure and the reactions of not only unstable light exotic but also of the superheavy and the super-superheavy nuclei is therefore required to improve our understanding of the astrophysical origin of atomic nuclei and the evolution of stars and their death [177].

The main objective of the present letter is to study the reaction (σ_r) and fusion (σ_f) cross-sections of neutron-rich U and some other interesting exotic isotopes, which are related to the formation of neutron-rich, SHE and super-SHE elements in the Universe. The value of σ_r is calculated by using relativistic mean field (RMF) and

the most recently developed effective field theory motivated relativistic mean field (E-RMF) nuclear densities [108], in conjunction with the Glauber model. However, σ_f is estimated in the non-relativistic coupled channel calculation. From the calculated reaction and fusion cross-sections, we look for the formation path of neutron-rich, SHE and super-SHE nuclei in the cosmos.

(b) Multi-fragmentation fission of thermally fissile nuclei

The world wide economic growth shows the requirement of a large amount of energy to fulfill the necessity of the people. In addition to this the limited amount of the bio-reservoir, such as coal and petroleum product force us to think seriously for a sustainable alternative. In this context, the nuclear or solar energy could be the possible potential substitution for the world's energy need. Also, the environmental impact related to nuclear energy is small relative to those associate with other methods of power generation [230]. The only dangerous aspect of environmental and health hazard is the nuclear accident. But this can be minimized by taking necessary precautions of its handling [231]. In this context, one can quote that the release of radiation on the environment by nuclear power plant within 80 Km is about 0.1 μSv per year compared to 260 μSv radiation from cosmic rays [232].

Although the nuclear fusion could be a vast energy source to face any kind of energy requirement, till date it has not been possible to use for civilian purpose. It is only so far tested for nuclear weapon as thermonuclear devices (hydrogen bomb). The other nuclear energy source is the nuclear fission. This is used in most of the advanced countries as a viable energy supply. Recently, country like India has also taken the program into account in a much more rigorous way.

To get fission energy from heavy elements one has to look for thermally fissile materials for nuclear fuel, which generate a lot of power in nuclear reactor. There are only three thermally fissile nuclei ^{233,235}U and ^{239}Pu known to the scientific com-

munity. Out of these, only ^{235}U is naturally available, whereas ^{233}U and ^{239}Pu are synthesized from ^{232}Th and ^{238}U respectively with a neutron bombarding in it followed by subsequent $\beta-$decay from the formed compound nucleus. In particular, ^{238}U is the major proportion of the fuel element material in a thermal reactor, capture of neutrons by ^{238}U and the creation of ^{239}U is an important process. ^{239}U quickly emits a $\beta-$particle to become ^{239}Np. Then ^{239}Np in turn emits a $\beta-$particle to become ^{239}Pu, which is relatively stable and a good candidate of thermally fissile element. Some ^{239}Pu nuclei may capture a neutron to become ^{240}Pu, which is less stable, by further neutron capture, some ^{240}Pu may in turn form ^{241}Pu. This ^{241}Pu also undergoes beta decay to form ^{241}Am. Similarly, the synthesis of ^{233}U using ^{232}Th which is a better abundance obtained through the process $n+^{232}Th \longrightarrow ^{233}Th \underrightarrow{\beta} ^{233}Pa \underrightarrow{\beta} ^{233}U$.

In case of ^{235}U the induced nuclear fission triggers chain reaction and the average number of neutrons produced by nuclear fission is two or three (average 2.5) and the nuclear fission cross section is relatively large. One of these neutrons is needed to sustain the chain reaction at a steady level of controlled criticality on average, the other 1.5 is leaked from the core region or absorbed in non-fission reactions. The captured neutron by non-fissile nuclei produces some energy by this mechanism in the form of gamma rays as the compound nucleus is de-excited. The resultant new nucleus may become more stable by emitting $\alpha-$ or $\beta-$ particles.

6.2 Calculations and results

It was shown in earlier chapters that the densities taken from relativistic mean field formalism, and used in the frame-work of Glauber model [10, 133] to evaluate the differential and total reaction cross section is quite successful for light systems [184]. Now we extend the model to calculate the total reaction cross section considering light exotic nuclei as projectile and heavy neutron-rich isotopes as target. Here, we

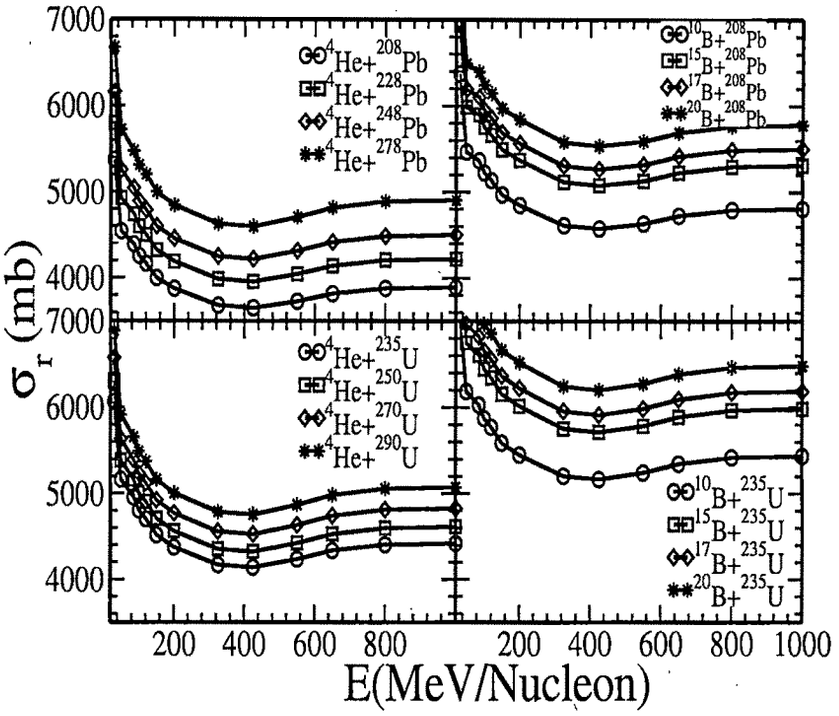

Figure 6.1: The nuclear reaction cross sections taking He and B isotopes as projectile with different isotopes of Pb and U.

calculate as the representative cases for the reaction cross section of neutron-rich Pb, Th and U isotopes taking exotic He, Li, B and O nuclei as incident projectile. The bulk properties, such as binding energy (BE), root mean square charge radius r_{ch}, matter radius(r_m), quadrupole deformation parameter β_2 for the various isotopes of He, Pb and U are listed in Table 6.1 with available experimental data. The Gaussian co-efficients required for cross section calculation are also given in this table.

In Fig. 6.1 the reaction cross section σ_r for ^{4}He+^{208,228,248,278}Pb, ^{10,15,17,20}B+^{208}Pb, ^{4}He+^{235,250,270,290}U and ^{10,15,17,20}B+^{235}U are presented. Fig. 6.2 and 6.3 represents σ_r for $^{244-260}$Th and $^{246-262}$U as targets with ^{6,11}Li and ^{16,24}O as projectiles. From the calculated results, the increase in σ_r is quite substantial with the target mass.

Table 6.1: Binding energy (BE), root mean square (rms) charge radius (r_c) and the coefficients c_1, a_1 and c_2, a_2 of Gaussian functions, which are fitted to the density distributions generated from E-RMF(G2) formalism. The BE is in MeV and rms radius in fm.

Nucleus	BE		r_c		Gaussian Co-efficients			
	E-RMF	Expt.	E-RMF	Expt.	c_1	a_1	c_2	a_2
^{4}He	29.39	28.30	2.076	1.676(8)	-1.0509	0.51495	1.2495	0.49740
^{10}B	61.42	64.75	2.492	2.45(12)	-0.145385	0.573468	0.379899	0.316861
^{15}B	88.20	88.19	2.479		-0.299572	0.425976	0.480853	0.253374
^{17}B	90.13	89.52	2.456		-0.224314	0.427336	0.396452	0.219516
^{20}B	92.13		2.510		-0.180161	0.41492	0.339182	0.184949
^{208}Pb	1631.80	1636.43	5.499	5.498(10)	-2.64313	0.0532685	2.75724	0.0492428
^{228}Pb	1704.48		5.665		-2.62604	0.0490159	2.73098	0.0453354
^{248}Pb	1764.75		5.792		-2.89059	0.0483861	2.99443	0.0447702
^{278}Pb	1800.71		5.938		-2.63895	0.0420423	2.7454	0.0390312
^{235}U	1778.65	1783.86	5.833	5.813	-2.54853	0.0471019	2.64847	0.0435424
^{250}U	1850.67		5.923		-2.75588	0.046275	2.85145	0.0428272
^{270}U	1930.71		6.025		-2.41462	0.0422599	2.52267	0.0390898
^{290}U	1953.41		6.14		-2.53234	0.0410558	2.63982	0.0379928

The same observation is also applicable, while increasing the mass of the projectile (keeping the target mass constant). In any of these cases, the reaction cross-section becomes favorable with either increase of projectile mass or the mass of the target or both. The enhancement can be understood by the simple classical expression of the cross-section πR^2 (R=radius of the nucleus) where the increase is due to the larger size of the nucleus. This implies the probability of formation of heavier masses in the reaction process with heavier isotope of the projectile as well as target. In Ref. [233], within the formalism of a Thomas-Fermi model, calculations are presented for nuclei beyond the nuclear drip-line at zero temperature. This is possible because of the presence of an external neutron gas which may be envisaged in the astrophysical scenario and is the situation of the present discussion for accreting cosmological objects.

In Fig. 6.4 the fusion cross-section σ_f for various neutron-rich light nuclei with heavier drip-line isotopes, like ^{4}He+^{208,228,248,278}Pb, ^{10,15,17,20}B+^{208}Pb, ^{4}He+^{235,250,270,290}U and ^{10,15,17,20}B+^{235}U are shown. Similar to the reaction cross-section, the increase in σ_f is quite clear with the increase of target, projectile or both the masses. This implies the probability of creation of heavier masses with the increase of mass number of the projectile as well as target and making the way for the evolution of neutron-rich heavy nuclei much beyond the drip-line [233] due to the presence of the external neutron gas or highly neutron-rich light as well as heavy nuclei generates in the astrophysical objects, in the relativistic jets of GRBs or supernovae jets near the nascent neutron star.

Analysis of figures 6.1 to 6.4 shows that, the magnitude of σ_r and σ_f are optimum at $\sim$ 30 to 200 MeV of the incident projectile energy. Beyond this range, the value of σ_r and σ_f decreases drastically. The variation of σ_r per two neutrons in the Th-isotopic chain are $\sim 28-30$ mb for ^{6}Li, $\sim 31-33$ mb for ^{11}Li, $\sim 32-36$ mb for ^{16}O and $\sim 35-37$ mb for ^{24}O. Similarly for Uranium target, this changes are $\sim 22-33$

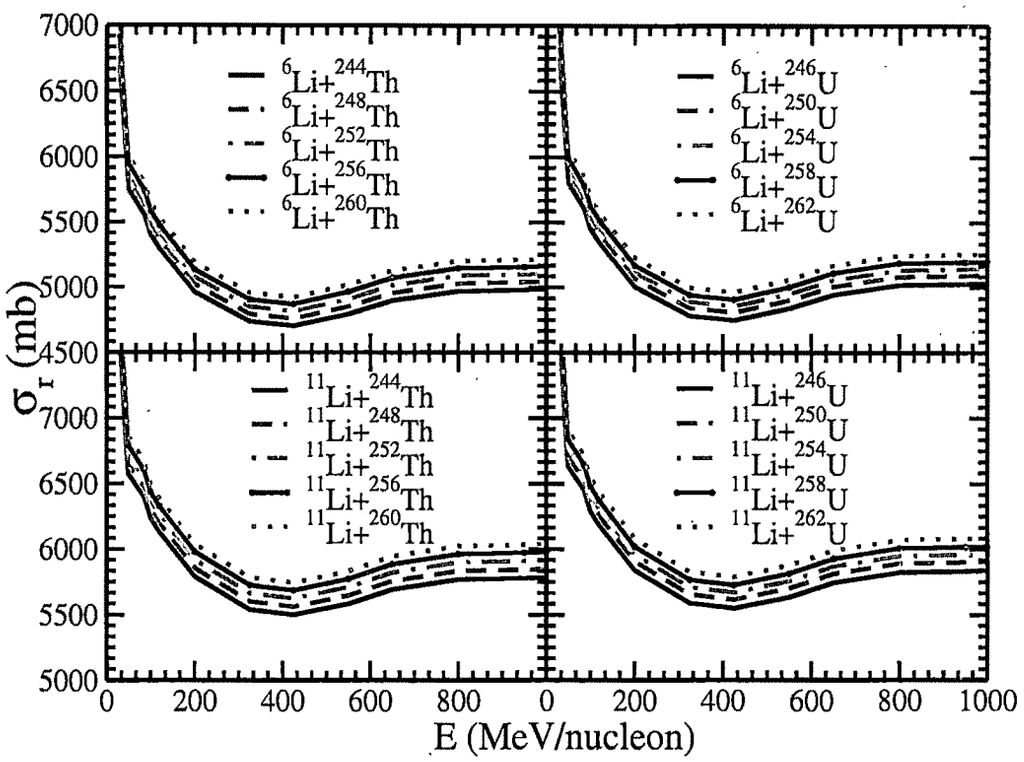

Figure 6.2: Same as Fig. 6.1 but for thermally fissile $^{244-262}$Th and $^{246-264}$U targets with ^{6,11}Li as projectiles at different incident energies.

mb for ^{6}Li, $\sim 25-34$ mb for ^{11}Li, $\sim 27-34$ mb for ^{16}O and $\sim 29-36$ mb for ^{24}O. Interestingly, increase of σ_r is least from ^{250}U to ^{252}U for these four projectiles. A further inspection of σ_r shows, the rate of increase is large for ^{6}Li to ^{11}Li than ^{16}O to ^{24}O. This results are depicted in Table 6.3. Both the cross sections indicate the suitability of the incident projectile energy for a favorable condition of the formation of the fused elements in the astrophysical system. Thus, the chance of the formation of heavier element is maximum, if a suitable energy range is created, which may be a source in the relativistic jets of GRBs or supernovae jets near the nascent neutron star [206, 207]. The high energy environment in such cosmological objects is because of the supernova shock [208] and it is quite common in the nascent neutron star or

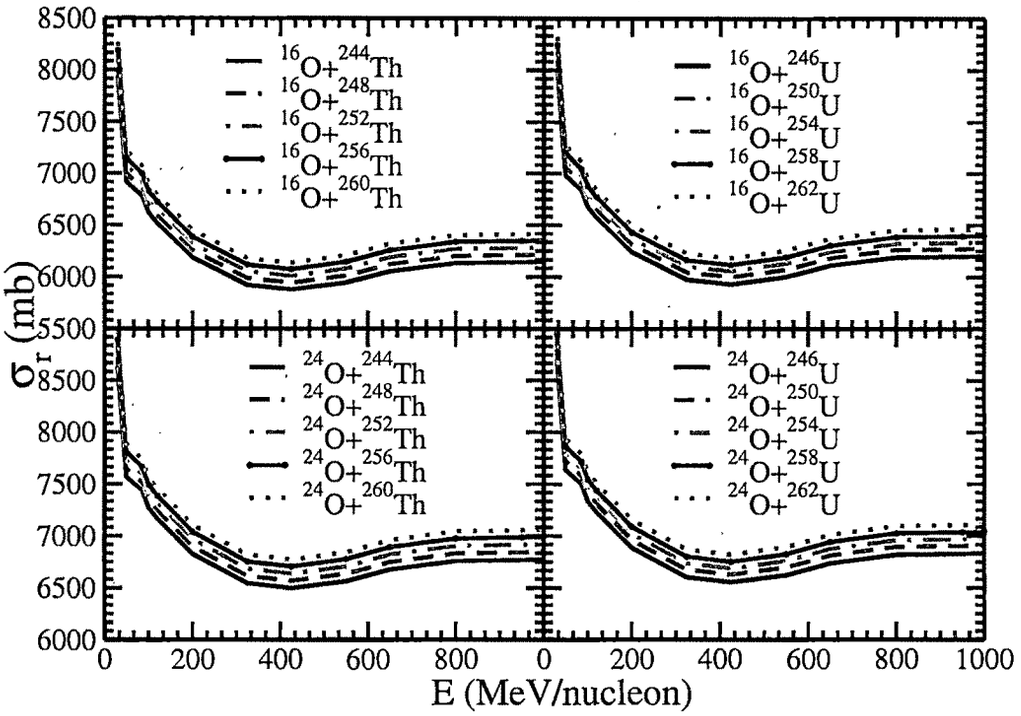

Figure 6.3: Same as Fig. 6.2 but with $^{16,24}O$ projectile.

relativistic jest of GRBs [206, 207]. In these objects a highly neutron-rich and high temperature scenario is made possible and which may be a probable platform for such reactions.

The increase in nuclear reaction cross section and fusion cross section with mass number could be a finite possibility for power generation in near future. Right now the formation of such neutron-rich heavy nuclei looks like hypothetical. However after the completion of Facility for Antiproton and Ion Research (FAIR) [234] at GSI, Germany, there is every possibility for an accelerator based reactor where these thermally fissile neutron-rich Thorium and Uranium nuclei could be a viable nuclear fuel for the power generation of the entire world. The life-time of the considered nuclei are expected to be small because of $\beta-$decay. But the production of these

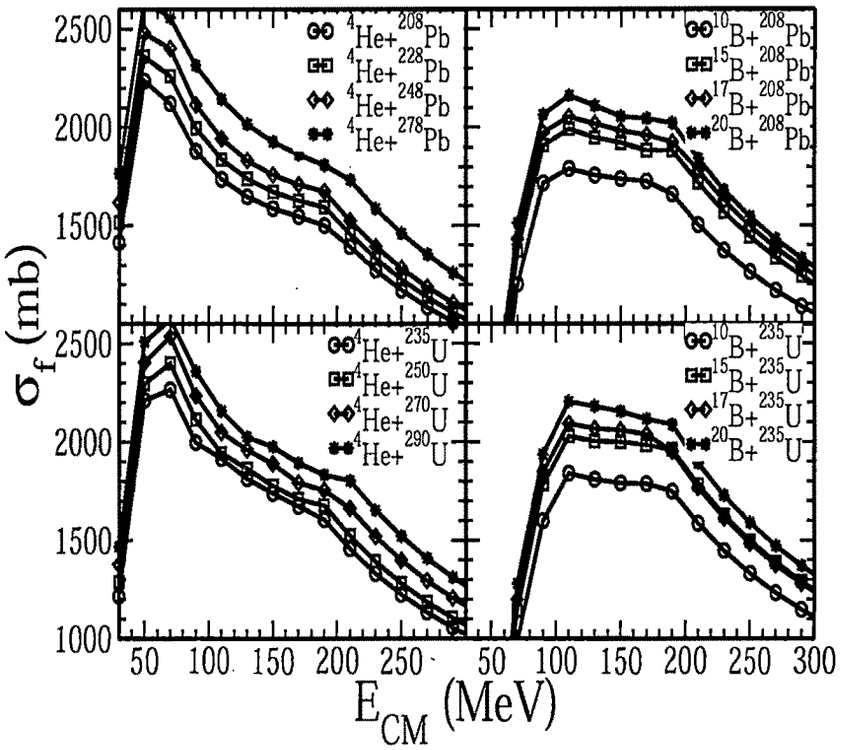

Figure 6.4: The nuclear fusion cross sections taking He and B isotopes as projectile with different isotopes of Pb and U.

nuclei via accelerator and their direct use in the reactor for power generation will be an ideal technical design.

In this context, it is worth citing the following example: A neutron star is burned when a star of mass $\sim$ 20 $M_\odot$ undergoes its core collapses after hyper-energetic explosions of Gamma ray bursts. A star with initially $\sim$ 20 $M_\odot$ would develop carbon-oxygen core of $\sim$ 3.3 $M_\odot$. It left behind a neutron star of $\sim$ 1.4 $M_\odot$, $\sim$ 1.3 $M_\odot$ of oxygen and $\sim$ 0.6 $M_\odot$ of heavier elements, Si and Fe group, which could be ejected in the supernova. Such a collapse gives rise to an explosion of kinetic energy K.E. $\sim 10^{51}$ ergs ($\sim 6.25 \times 10^{56} MeV$) [206, 207]. The interior and surface of young neutron stars are fluid and the crust is solid crystalline.

Table 6.2: The coefficients c_1, a_1 and c_2, a_2 of Gaussian functions, which are fitted to the density distributions generated from RMF(NL3) formalism for Th and U isotopes.

Target	RMF(NL3)			
	c_1	a_1	c_2	a_2
^{242}Th	-2.56295	0.046101	2.66072	0.0426229
^{244}Th	-2.57455	0.0458467	2.67157	0.0423937
^{246}Th	-2.58511	0.045586	2.68138	0.0421592
^{248}Th	-2.58381	0.0453282	2.67959	0.0419151
^{250}Th	-2.59781	0.0450663	2.69291	0.0416847
^{252}Th	-2.60123	0.0448158	2.69571	0.0414519
^{254}Th	-2.60059	0.0445618	2.69484	0.0412164
^{256}Th	-2.61142	0.0443161	2.7052	0.0409989
^{258}Th	-2.61164	0.0440842	2.70529	0.040783
^{260}Th	-2.60932	0.0438473	2.70302	0.040563
^{262}Th	-2.61241	0.0435959	2.70652	0.0403415
^{244}U	-2.54329	0.0455993	2.6396	0.0421534
^{246}U	-2.5595	0.0453629	2.655	0.0419438
^{248}U	-2.56618	0.0451347	2.66086	0.04173
^{250}U	-2.59612	0.0448921	2.6908	0.0415151
^{252}U	-2.58623	0.04466	2.67954	0.0412992
^{254}U	-2.59252	0.0444323	2.68509	0.0410873
^{256}U	-2.60491	0.0442003	2.6971	0.0408828
^{258}U	-2.6099	0.0439919	2.70157	0.0406878
^{260}U	-2.63638	0.0437825	2.72829	0.0404995
^{262}U	-2.64603	0.0435736	2.73785	0.0403142
^{264}U	-2.64126	0.0433618	2.73345	0.0401156

Table 6.3: Total nuclear reaction cross section σ_r for thermally fissile $^{244-262}$Th and $^{246-264}$U targets with $^{6,11}Li$ and $^{16,24}O$ projectiles at energy 800 MeV.

Target	σ_r (mb) for Projectile			
	^{6}Li	^{11}Li	^{16}O	^{24}O
^{242}Th	4942.09	5737.91	6099.93	6723.97
^{244}Th	4970.99	5769.79	6133.19	6759.56
^{246}Th	5000.51	5802.37	6167.53	6795.97
^{248}Th	5030.03	5835.32	6201.96	6832.49
^{250}Th	5059.62	5867.68	6236.42	6869.02
^{252}Th	5089.12	5900.26	6270.77	6905.42
^{254}Th	5118.17	5932.38	6304.70	6941.40
^{256}Th	5146.73	5963.91	6337.95	6976.64
^{258}Th	5174.45	5994.52	6370.29	7010.85
^{260}Th	5202.25	6025.25	6402.09	7045.25
^{262}Th	5230.00	6056.00	6435.22	7079.75
^{244}U	4990.78	5792.15	6157.39	6785.40
^{246}U	5018.75	5823.02	6189.85	6819.84
^{248}U	5046.81	5853.94	6222.37	6854.29
^{250}U	5081.38	5891.66	6261.66	6895.75
^{252}U	5103.77	5916.74	6288.48	6924.32
^{254}U	5132.12	5947.98	6321.36	6959.13
^{256}U	5159.70	5978.38	6353.39	6993.05
^{258}U	5186.43	6007.81	6384.34	7025.81
^{260}U	5218.94	6043.22	6421.15	7064.60
^{262}U	5244.57	6071.46	6450.88	7096.07
^{264}U	5270.15	6099.72	6480.70	7127.66

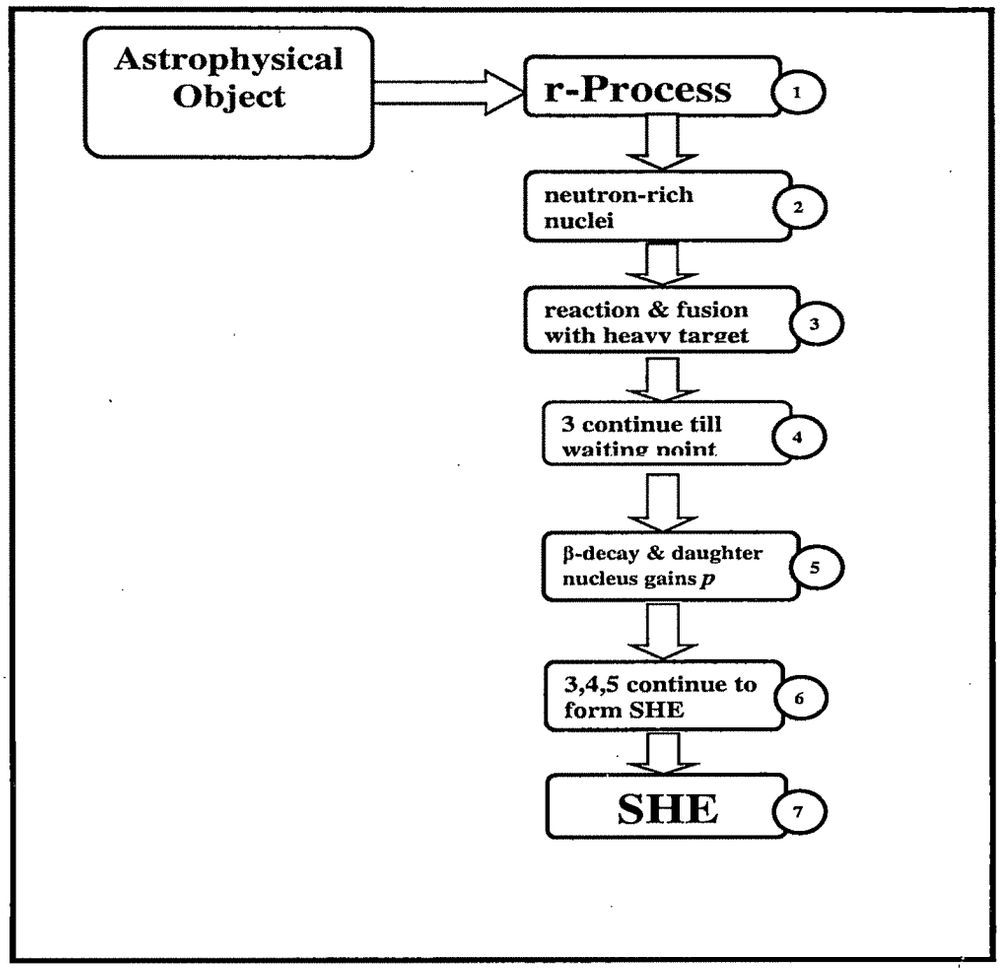

Figure 6.5: The schematic diagram for the formation of superheavy element (SHE) in the astrophysical object. The production of SHE is possible through reaction and fusion processes at a favorable energy condition in the cosmos.

The fluid regions of the star adjust themselves to its rotation which remaining always axi-symmetric. The radiated power comes directly from the rotational energy of the neutron star. The entropy in mass elements exhibiting the neutron star at later times will be larger than the earlier. This is because, most of the heating occurs near the surface of the neutron star. Slowly with time the radius of the neutron star shrinks from $100Km$ to $10Km$ [235, 236]. The decrease in the initial radius start from which the mass elements begin increasing the heat rate [206, 207].

It is worth mentioning of the burning process of H, He, Li, ... in the accreting astrophysical system. To maintain *hydrostatic equilibrium* [237], this continues upto formation of Iron. When this stage is reached, depending on its mass, the astrophysical object undergoes various phenomena like supernovae explosion, X-rays burst, GRBs, formation of neutron star, black hole, red giant or white dwarf etc. In some cases, it becomes highly neutron-rich environment (novae, supernovae or X-rays burst or neutron star) and is favorable for rn-process, which continue upto certain A or Z number. Slowly, this rn-capture process becomes less favorable and fusion of light nuclei (like He, Li, Be,...) become more important. In the mean time, the neutron-rich light element fused with these heavy nuclei and more heavier isotopes with a little increase of proton number is generated in the process; for example, ^{4}He+^{208}Pb gives ^{212}Po. Again ^{212}Po reacts with ^{4}He to form ^{216}Rn.

A schematic diagram for the process of SHE formation is shown in Figure 6.5. From the figure, it can be understood how this phenomenon goes on to create much heavier isotopes. Similarly other processes also continue to go on as shown in Figs. 6.1 to 6.4 and, such as ^{20}B+^{235}U$\rightarrow$ ^{255}Bk, ^{20}B+^{255}Bk $\rightarrow$^{275}No, ... and so on. A representative example is depicted in Figure 6.6. As mentioned earlier, after the supernovae explosion, in the rn-process, heavy normal/exotic nuclei including the ultra-neutron-rich light isotopes are formed. Exotic nuclei like ^{6}He, ^{11}Li, ^{14}Be, ^{20}B,

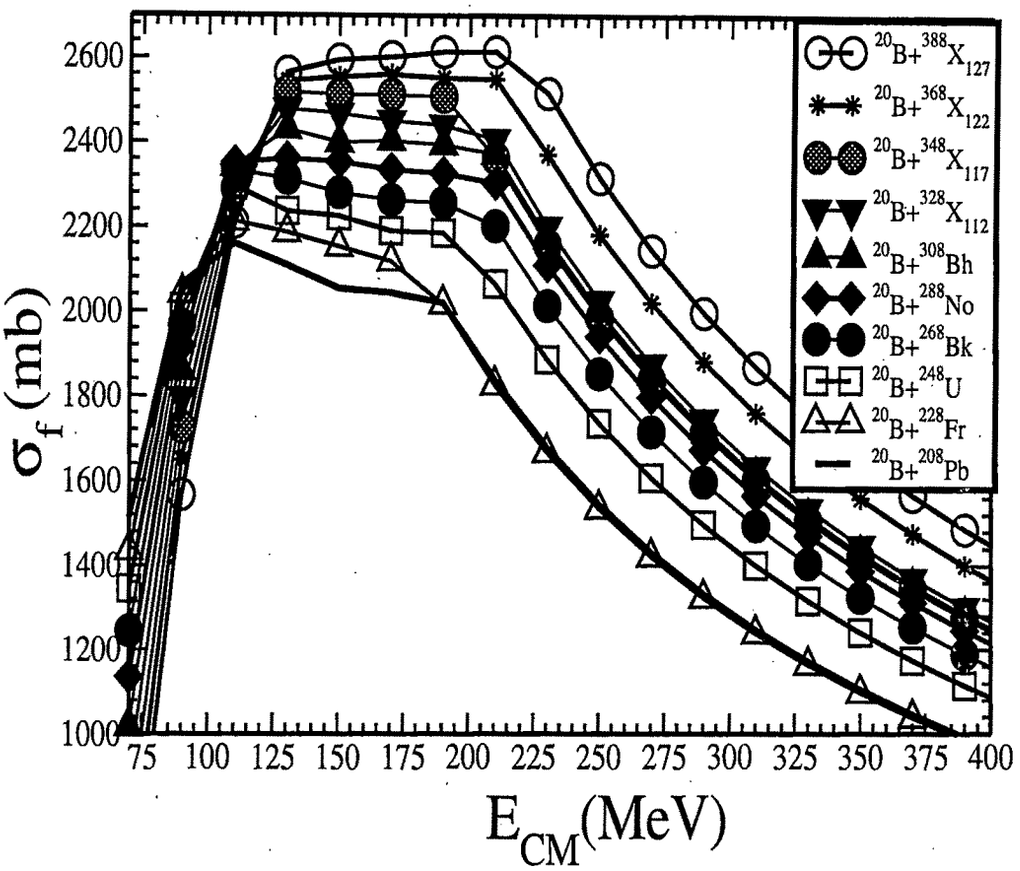

Figure 6.6: A representative path for the formation of $^{408}X_{132}$ superheavy element through ^{20}B capture process. The fusion cross-sections σ_f for various daughter nuclei with ^{20}B is shown.

normal actinides (e.g. ^{208}Pb, ^{235}U etc.) and neutron-rich drip-line isotopes, similar to ^{278}Pb etc. are generated. Thereafter, fusion process of the light isotopes with heavier nuclei becomes important. The increase of fusion cross-sections as shown in Fig. 6.4 confirmed the possibility of the formation of ultra-heavy isotopes as well as superheavy elements both with lower and higher atomic masses. The demonstration of a path for the formation of $^{408}X_{132}$ (A=408, Z=132, N=276) through complete fusion process is given below (whose cross-sections are shown in Fig. 6.4):

^{20}B+^{208}Pb $\rightarrow$ ^{228}Fr, ^{20}B+^{228}Fr $\rightarrow$ ^{248}U, ^{20}B+^{248}U $\rightarrow$ ^{268}Bk, ^{20}B+^{268}Bk $\rightarrow$ ^{288}No, ^{20}B+^{288}No $\rightarrow$ ^{308}Bh, ^{20}B+^{308}Bh $\rightarrow$ $^{328}X_{112}$, ^{20}B+$^{328}X_{112}$ $\rightarrow$ $^{348}X_{117}$, ^{20}B+$^{348}X_{117}$ $\rightarrow$ $^{368}X_{122}$, ^{20}B+$^{368}X_{122}$ $\rightarrow$ $^{388}X_{127}$, ^{20}B+$^{388}X_{127}$ $\rightarrow$ $^{408}X_{132}$ and so on.

Thus, each time the proton number Z increases by 5 units the mass number A goes up by 20 units in the case of ^{20}B capture. Slowly, it creates a highly neutron-rich heavy isotope, which is enabled to capture any more neutron n or neutron-rich nucleus. This is termed as *waiting point.* Here, the neutron-rich heavy element emits a β^-– particle, and the daughter nucleus gains a positive charge by converting a neutron (n) to a proton (p). Due to this enhancement in Z, the product (daughter nucleus) captures few more n or neutron-rich light nuclei by fusion process till it reaches the new waiting point. At this point, the nucleus gains another proton p, by emitting β^-–particle. This process continues and SHE or super-SHE are formed in the cosmological object. In this context, it is worth mentioning that, the dominant mode of decays are β^- and spontaneous fission for large N and large Z nuclei, respectively. In the β^-– decay, the daughter nucleus gains a proton, whereas for large N, the spontaneous fission reduces considerably due to excess number of neutrons [16] and the neutron-rich isotope becomes fission stable as the height of the fission barrier decreases and the width increases, thereby making the nucleus more stable against fission [16]. It is interesting to mention here that, recently it has been reported by A. Marinov et al. [179], that the evidence of a superheavy isotope with $Z = 122$ or 124 and a mass number A=292; has been found in natural Th using inductively coupled plasma-sector field mass spectrometry. The estimated half-life of this isotope is $t_{1/2} \geq 10^8$ years, comparable with the theoretical predictions [77, 94, 210, 212, 213].

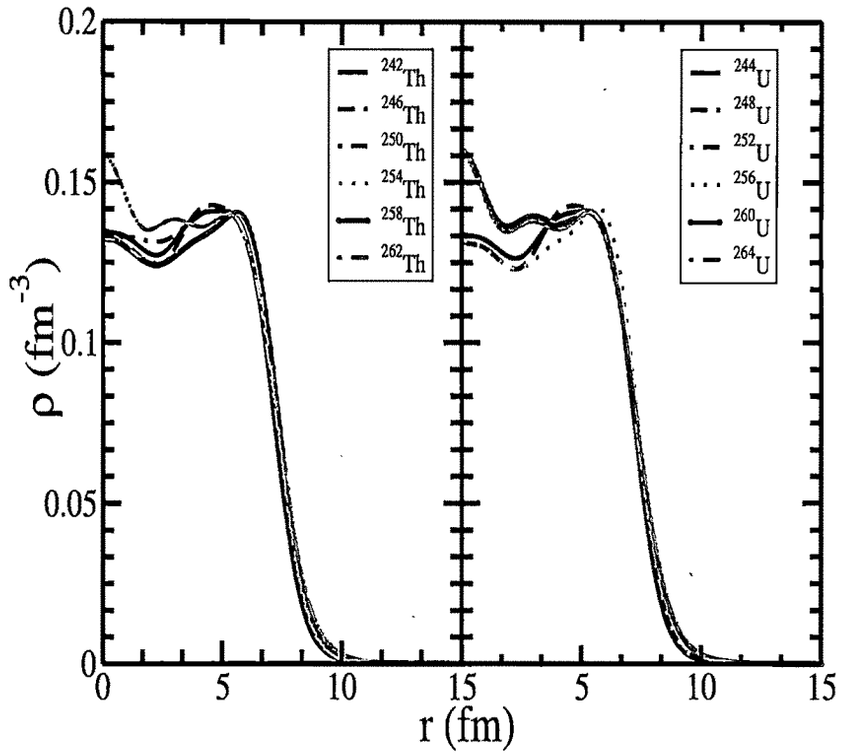

Figure 6.7: The total nuclear density obtained by NL3 parameter set [112] for some of the Thorium and Uranium isotopes.

Multifragmentation Fission in Neutron-rich U and Th Nuclei

The spherical densities ρ for Thorium and Uranium isotopes are given in the left and right panel of Fig. 6.7 respectively. The central part of the density distributions are slightly different from one isotopes to other. On the other hand the tail regions are almost identical. The bulk properties, such as binding energy (BE), root mean square charge radius r_{ch}, matter radius r_m and quadrupole deformation parameter β_2 for the thermally fissile nuclei $^{246-264}$U and $^{244-262}$Th in the RMF formalism are presented in Table 6.4. The calculated results are compared with the widely acceptable finite range droplet model (FRDM) and with the experimental data wherever available [80, 81].

In one of our earlier paper [17] it is shown that the calculated RMF results agree well with the experimental data. Here the investigation is done for highly neutron-rich nuclei where the data are yet to be known.

It is clear that our RMF results agree remarkably well with the FRDM values. For example, the RMF binding energy for ^{252}Th and ^{262}U are 1854.2 and 1899.2 MeV as compare 1853.6 and 1899.0 MeV of the FRDM. Similarly, the β_2 values for these two nuclei are 0.199 and 0.118 of RMF with 0.219 and 0.107 from FRDM calculations. In case of ^{264}U the ground state binding energy is 1906.7 MeV in RMF calculation and 1906.0 MeV in FRDM and the corresponding β_2 are -0.089 and -0.138. This means, the ground state is in oblate configuration and inhibit fission. Therefore, we have given the result for first excited prolate configuration in Table 6.4 which open the path for thermal fission.

It is well-known that 2.5 average number of neutrons emit from the ^{235}U in the thermal fission process. This number is more than twice for ^{250}U [16, 17], which integrate the thermal fission process and produce order of magnitude more energy. It is worth mentioning that in multifragmentation fission along with the usual two big fragments [which we are used to] a few (about 3 neutrons in case of ^{250}U) neutrons come out from the fission process [16, 17]. In case of ^{250}U on an average of 5.5 neutrons will evolve. That is 3 multifragmentation neutrons and 2.5 prompt neutrons will come out per fission process. For more clear, in case of ^{235}U, we get only 2.5 prompt neutrons and no multifragmentation neutrons. In these highly neutron rich compound nucleus, the fragments after fission have the same atomic number but highly neutron rich than that the fragments evolves from $^{233-235}$U and ^{239}Pu. As a result the nuclei (fragments) formed after fission crosses the boundary of nuclear chart (the drip line) and unable to accept these excess neutrons and evolves as multifragmentation fission neutrons.

Table 6.4: Calculated results for the binding energy (BE), charge and matter radius (r_{ch}, r_m) and deformation parameter(β_2) for various Thorium and Uranium isotopes. The values of finite range droplet model (FRDM) [80, 81] and experimental data [167, 168, 238] are also given for comparison. Energy is in MeV and radius is in fm.

Nucleus	BE		RMF		β_2	
	RMF	FRDM	r_{ch}	r_m	RMF	FRDM
^{242}Th	1813.3	1816.3	5.912	6.065	0.284	0.235
^{244}Th	1821.0	1824.1	5.921	6.082	0.269	0.225
^{246}Th	1828.6	1831.6	5.926	6.098	0.255	0.217
^{248}Th	1836.1	1839.1	5.926	6.111	0.235	0.209
^{250}Th	1843.5	1846.5	5.929	6.125	0.215	0.209
^{252}Th	1854.2	1853.6	5.938	6.156	0.199	0.219
^{254}Th	1861.9	1859.8	5.946	6.170	0.172	0.192
^{256}Th	1865.4	1864.7	5.955	6.175	0.155	0.088
^{258}Th	1876.0	1871.1	5.965	6.209	0.145	0.088
^{260}Th	1883.0	1877.2	5.973	6.228	0.131	0.098
^{262}Th	1890.1	1883.7	5.981	6.247	0.120	−0.129
^{244}U	1830.4	1832.3	5.937	6.074	0.290	0.235
^{246}U	1838.7	1840.9	5.948	6.093	0.282	0.225
^{248}U	1846.7	1849.1	5.956	6.111	0.271	0.217
^{250}U	1854.5	1857.3	5.960	6.126	0.257	0.218
^{252}U	1864.6	1865.4	5.958	6.147	0.227	0.218
^{254}U	1872.9	1873.1	5.965	6.163	0.207	0.219
^{256}U	1880.9	1880.0	5.973	6.177	0.179	0.201
^{258}U	1888.4	1886.3	5.982	6.196	0.164	0.162
^{260}U	1895.7	1892.7	5.990	6.213	0.147	0.116
^{262}U	1899.2	1899.0	5.996	6.214	0.118	0.107
^{264}U	1903.2	1906.0	5.996	6.230	0.124	−0.138
	1906.7		6.003	6.230	−0.089	
Nucleus	BE		RMF		β_2	
	RMF	Expt.[80, 81]	r_{ch}	r_m	RMF	FRDM
^{6}Li	44.5	31.99	$2.987(2.589 \pm 0.039)$	2.862	0.232	
^{11}Li	54.5	45.71	$2.366(2.482 \pm 0.043)$	2.708	0.012	
^{16}O	129.3	127.62	$2.877(2.72 \pm 0.02)$	2.741	0.026	0.021
^{24}O	171.6	168.95	2.747	3.054	0.008	0.003

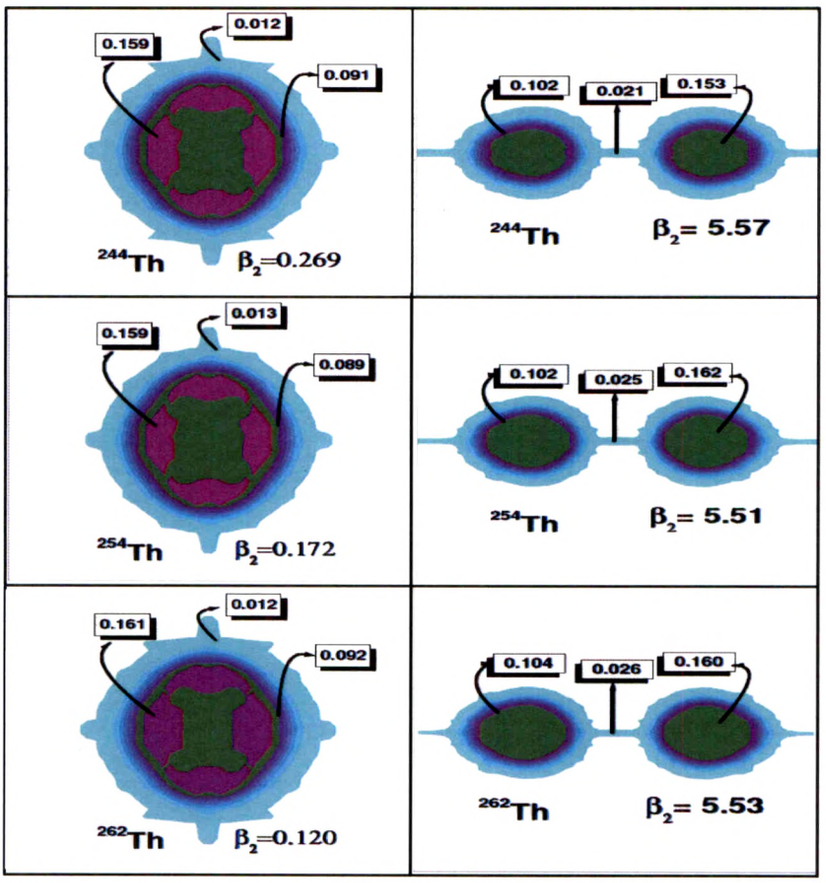

Figure 6.8: The evolution of neck configuration for ^{244,254,262}Th, i.e., the total density ρ at ground state and in the scission configuration.

Now it is obvious that 5.5 prompt neutrons participate in the chain reaction in case of ^{250}U compared to the 2.5 neutrons of ^{235}U. As a result, neutron-rich thermally fissile nuclei reaches to the critical stage much faster than the normal thermally fissile material like ^{233,235}U and ^{239}Pu. This phenomenon can be illustrated by counting the number of neutron emerges from the multifragmentation fission. For this, we

Table 6.5: Anatomy of neck at the fission configuration for ^{244,254,262}Th and ^{244,254,264}U. Here z and ρ are the range of the neck where we have counted the number of neutron N_n, proton N_p and their ratio. l_{neck} and r_{ch}^{neck} stand for length of the neck and charge radius of the nucleus in fm .

Nucleus	Range of Neck		Neck Nucleons		N_n/N_p	r_{ch}^{neck}	l_{neck}
	z	ρ	N_p	N_n			
^{244}Th	$\mp$1.039	$\mp$2.45	0.7	2.67	3.81	11.86	4.72
^{254}Th	$\mp$1.044	$\mp$2.43	0.7	3.4	4.86	11.77	4.63
^{262}Th	$\mp$1.043	$\mp$2.41	0.9	3.9	4.33	11.70	4.45
^{244}U	$\mp$1.018	$\mp$2.38	0.8	2.7	3.38	12.09	6.18
^{254}U	$\mp$1.018	$\mp$2.38	0.9	3.7	4.11	11.76	5.65
^{264}U	$\mp$1.02	$\mp$2.36	1.02	5.47	5.02	11.72	4.14

have shown the contour plot of density distribution for selective cases ^{244,254,262}Th and ^{244,254,264}U in Fig. 6.8 and Fig. 6.9.

We concentrate on the neck region of the contour curve at the fission (or near fission) state ($\beta_2 \sim 6.0$). By integrating the density of that portion, we get the number of nucleons present in the neck. Also, we have calculated the length of the neck l_{neck}, the number of neck nucleons (proton N_p and neutron N_n) and their ratio $\frac{N_n}{N_p}$ for ^{244,254,262}Th and ^{244,254,264}U, which are given in Table 6.5. The neck length l_{neck} (or area) almost remains same (or decreases slightly) with mass number of a nucleus, but the availability of nucleons and their ratio increases. For example, N_n =2.673 and 2.7 for ^{244}Th and ^{244}U and these numbers are 3.9 and 5.5 for ^{262}Th and ^{264}U. This says about the multiplicity of neutron number at the time of fission for neutron-rich nuclei. This will be responsible for the increase of chain reaction at the time of power production with such fuels. To have a better understanding about the neck

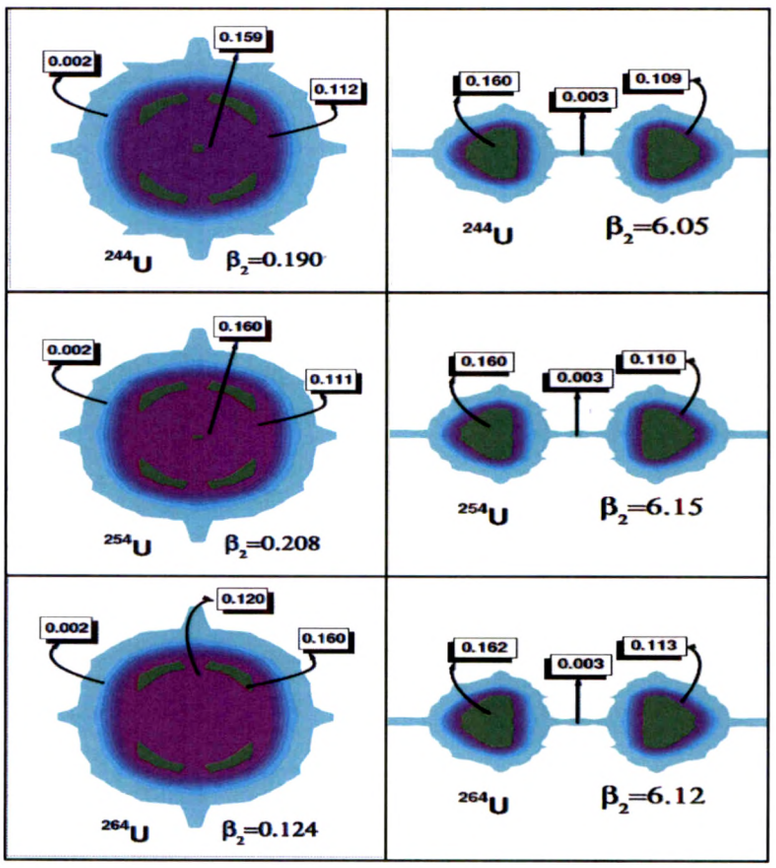

Figure 6.9: The evolution of neck configuration for ^{244,254,264}U, i.e., the total density ρ at ground state and in the scission configuration.

evolution, the analysis can be done from the density distribution at various quadrupole deformation parameter (see Figs. 6.8 and 6.9). At large deformation the nucleus is divided into two major fragments along with the emission of few more neutrons from the neck. Because of the large number of neutron emission (multifragmentation fission) at the time of fission, the critical mass of these nuclear fuel is expected to be small, which may be an extra mileage for collection of such materials.

Table 6.6: Comparison of RMF and FRDM [80, 81] results for β decay energy Q_β and half life-time T_β of ^{242262}Th and ^{244264}U.

N	Q_α		T_α		N	Q_α		T_α	
	RMF	FRDM	RMF	FRDM		RMF	FRDM	RMF	FRDM
^{242}Th	5.519	2.71	7.124	14.507	^{244}U	4.446	1.49	33.51	>100
^{244}Th	6.025	3.86	1.829	2.855	^{246}U	5.017	2.70	10.80	20.07
^{246}Th	6.46	4.09	1.443	2.279	^{248}U	5.508	3.14	5.623	9.363
^{248}Th	6.851	4.66	0.657	0.967	^{250}U	5.923	3.44	3.277	2.934
^{250}Th	7.172	4.98	0.452	0.65	^{252}U	6.395	3.81	1.748	2.934
^{252}Th	7.431	5.50	0.279	0.377	^{254}U	6.717	4.38	0.836	1.282
^{254}Th	7.544	6.32	0.167	0.20	^{256}U	6.944	5.24	0.499	0.661
^{256}Th	7.821	7.43	0.026	0.271	^{258}U	6.892	5.83	0.230	0.272
^{258}Th	8.309	6.68	0.056	0.07	^{260}U	6.656	6.04	0.120	0.133
^{260}Th	9.961	7.14	0.049	0.062	^{262}U	7.06	6.33	0.108	0.120
^{262}Th	9.501	6.73	0.087	0.123	^{264}U	6.594	5.83	0.233	0.264

6.3 Conclusions

In summary, we estimated the reaction and fusion cross section of various combination of light and heavy isotopes. We extended the calculations to exotic systems taking into consideration the possibility of availing the rn-process and the exotic nuclei capture processes in astrophysical objects. The enhanced cross sections with increase of mass number for both the projectile and target made it possible for the formation of the heavier neutron-rich nuclei way beyond the normal drip-lines predicted by the mass models. By the neutron or heavy ion (light neutron-rich nuclei) capture process the daughter nucleus becomes a superheavy element which may be available somewhere in the Universe in super-natural condition and can be possible to be synthesized in laboratories. Here the stability of the neutron-rich SHE or super-SHE against spontaneous fission arises due to widening of the fission barrier because of the excess number of neutrons.

We have also studied the structural properties of the recently predicted thermally fissile neutron-rich $^{244-262}$Th and $^{246-264}$U nuclei in the frame-work of RMF model.

The results are compared with the most popular FRDM calculations and found remarkably closure with its predictions. The obtained RMF densities are used to estimate the reaction cross section taking these fissile isotopes as target with ^{6,11}Li and ^{16,24}O as projectile. This results may be useful for experimentalists for the synthesis of neutron-rich thermally fissile Thorium and Uranium for the energy generation in future. The anatomy of the fission process is done with the help of the neck configurations. The maximum number of multifragmentation neutron at the time of fission is found to be more with larger neutron-rich nuclei. The excess neutrons are responsible to produce extra neutron fragments at the time of scission and emits few additional prompt neutrons along with the normal fission neutron (similar to the 2.5 neutrons of ^{235}U). The extra neutrons prompt the chain reaction which are vulnerable to thermal neutron fission and produce much more energy compared to ^{233,235}U or ^{239}Pu. This certainly increase the efficiency of the chain reaction during the fission process and will reduce the critical mass of the nuclear fuel, if neutron-rich thermally fissile nuclei will be used as nuclear fuel in an accelerator based nuclear reactor.

Chapter 7

Summary and Conclusions

In the present thesis, we have studied the nuclear reaction for both stable and unstable nuclei throughout the periodic table. We have applied the well known Glauber formalism for various nuclear cross section calculations, such as, the total nuclear reaction cross sections (σ_r), differential elastic scattering cross sections ($\frac{d\sigma}{d\Omega}$), one nucleon removal cross sections (σ_{-1n}, σ_{-1p}) etc. For the evaluation of reaction parameters like σ_r, $\frac{d\sigma}{d\Omega}$, σ_{-1n} and σ_{-1p} through Glauber model, one need the nuclear structure input, like the densities of the target and projectile nuclei. To get these inputs, some reliable models are required. Here we have taken these inputs from the most successful non-relativistic and relativistic mean field formalism. We have evaluated the bulk properties of such nuclei like binding energy (BE), root mean square charge radius r_{ch}, matter radius r_m and quadrupole deformation parameter β_2 for both light medium and heavy nuclei in the ground as well as in intrinsic excited (or isomeric) state. Study of these quantities enables us to know the nuclear structure of unstable nuclei in detail, particularly the structure near the drip-lines. This will also help in studying the formation of neutron-rich nuclei that are surrounded by a high pressure or temperature. During the calculations in non-relativistic model, the Skyrme interaction is used. For the relativistic one, we have used the RMF theory developed by Green and Miller [28] and later modified by Boguta and Bodmer [30]. The re-

cently developed field theory motivated Relativistic Mean Field Effective Lagrangian approach (E-RMF) is also used at various places of the calculations.

The thesis is summarized as follows: First of all **Chapter-1** deals with an introduction where definitions of various type of nuclear reactions like direct reaction, fission, fusion etc are outlined. We have also discussed the importance of different nuclear models both non-relativistic and relativistic, which are required for our calculations and analysis of different observables like density, binding energy, charge radius, matter radius, deformation, reaction cross section, differential elastic scattering cross section, nucleon removal cross section etc. In this chapter we have also introduced exotic and halo nuclei in the subsection drip-line nuclei. Super-heavy nuclei and their formation by r-process are also mentioned.

In **Chapter 2**, we have presented both non-relativistic and relativistic models in detail. The Skyrme Hartee-Fock (SHF) model is discussed including the SHF Hamiltonian. This model reproduces the experimental data for ground as well as intrinsic excited state for finite nuclei. The Lagrangian density and field equations for nucleons and bosons are described in the RMF and E-RMF models. The calculations leading to the solutions of the RMF equations have been described in this Chapter. BCS-pairing prescription and other pairing correlations are also presented. To study heavy-ion elastic scattering, reaction cross section, nucleon removal cross section for both stable and unstable nuclei we have applied the Glauber approach. The transparency and profile functions required for the cross section calculation are also discussed. Coupled Channel Formalism (CCF), which is used for fusion cross section calculation is also included in this Chapter. The parameter sets, used in the calculations, are also presented.

In **Chapter 3**, we have discussed nuclear structure for ground and intrinsic excited (or isomeric) states in the frame work RMF and E-RMF formalism. The total density ρ, proton density ρ_p and neutron density ρ_n distribution for some light, medium

and heavy nuclei are shown graphically and discussed. Taking into account NL3 and G2 parameter sets, We have studied the similarities and differences on density distributions in different nuclei. The relative isotopic proton and neutron density differences $\Delta\rho_p(r)$ and $\Delta\rho_n(r)$ for Ca isotopes are also given. The comparison of $\Delta\rho_n(r)$ with the data indicates the superiority of G2 over NL3. The small difference in density at the central region significantly affect the results of scattering observables including the optical potential. The predicting capability of scattering observables of RMF (NL3) over E-RMF (G2) is also observed. The path for the formation of exotic nuclei by the spin rotation parameter from positive to negative direction is predicted. Thus the reaction dynamics are highly dependent on the input density and the choice of parametrization. We employ three types of density distributions: SHF, RMF and E-RMF theory. Several set of parameters like SKI4, SLy6, NL-SH, NL3, NL3*, G2 are used for this purpose.

Then we calculate the bulk properties, such as binding energy (BE), root mean square charge radius r_{ch}, matter radius r_m and quadrupole deformation parameter β_2 for light, medium and heavy nuclei in the RMF and E-RMF formalisms in both ground and excited states. We also employ the axially deformed RMF and non-relativistic mean field techniques to investigate the bulk properties for intrinsic excited states of ^{53}Co and ^{53}Fe. The results of extensive calculations for nuclei over a large range of atomic mass and charge are compared with the experimental data.

We have also calculated the single-particle energy levels of ^{53}Co and ^{53}Fe and the potential energy surfaces are also evaluated within the RMF and SHF techniques, which coincide remarkably well. From the single-particle energy spectra for ^{53}Co, the ground state spin and parity (J^π) were found to be $7/2^-$ and a highly admixed state of $1/2^-$ and $3/2^-$ spin-parity states was found to be the first excited state, which agree well with the prediction of shell model calculations. Similar results are

obtained in case of ^{53}Fe, i.e., the last neutron occupies the level $[303]7/2^-$ in the ground state solution and it is a mixture of $[310]1/2^-$ and $[321]3/2^-$ levels in the oblate excited state. The overall general trend is observed to be the same in both RMF and SHF formalism. It is worth mentioning that shell model is quite successful in its traditional low mass region, whereas the mean field formalisms are, in general, more appropriate for heavier nuclei. However, in one of our earlier study based on RMF formalism, it is shown that at least an α−particle is needed to get a reasonable binding energy and mass number should be more than $\sim$9 for the rms radii and other physical properties. The mass number A=53 in the present investigation, is rather large to get a satisfactory result for both the RMF and SHF theories.

The analysis of the single-particle energy spectra of these nuclei show a competition of spins $1/2^-$ and $3/2^-$ in a low-lying excited state, which agree well with the recent experimental observation [D. Rudolph, *et al.*, Eur. Phys. J. **A 36**, 131 (2008)] of spin and parity $J^\pi = 3/2^-$ for the isomeric configuration in ^{53}Co. Though the barrier in the PES does not suggest a clearly separated excited isomeric state but the "free solutions" and the large plateau at the bottom, explicitly in the oblate region, is the cause for the oblate band which gives a long lived isomeric state in the low-lying excited state of ^{53}Co and ^{53}Fe nuclei. Apparently, the change in internal structure, in going from ground prolate to excited oblate, makes the life-time of the isomeric state finite.

In **Chapter 4**, we have used the Glauber model for calculating the total nuclear reaction cross sections with densities obtained from RMF and E-RMF formalisms. The nuclear densities from the RMF and E-RMF models for the projectile and target nuclei, which are the main ingredients of the calculation of total nuclear reaction cross sections, have been fitted to a sum of two Gaussians, and the coefficients c_1, c_2 and ranges a_1, a_2 are calculated. This fitting procedure simplifies the numerical calculations considerably and makes it possible to obtain analytic expressions for the

transparency functions. In other words, using these coefficients, we got the equivalent density for calculating the transparency functions, which are further used to estimate the total nuclear reaction and differential elastic scattering cross sections.

Here we have compared the results with the experimental data for some selective cases and found nice matching. We have shown that the total nuclear reaction cross sections decrease with the increase of incident energy of the projectile. In most of the cases, the neutron-rich light mass nuclei are used as projectile and heavy nuclei as targets. In order to see the effect of the neutron-richness of the projectile in the exotic mass region, we repeated the calculations with various projectile masses without changing the target nucleus. We found that the total nuclear reaction cross section increases with increase of the projectile mass or with increase of neutron number of the target. Such a result is valid for both the normal and neutron-rich nuclei. Thus, our framework seems ideal for the simple analysis of the different ranges of data on total nuclear reaction cross sections of neutron-rich unstable nuclei. However, unlike the total nuclear reaction cross sections, the differential elastic scattering cross sections show marginal changes with the change of projectile mass. Specifically, we have calculated the total nuclear reaction cross section σ_r and the elastic differential scattering cross section $\frac{d\sigma}{d\Omega}$ for both the increasing projectile and target masses. In all cases, we find that σ_r increases with target mass. Analysing the elastic differential scattering cross section, however, we find that the magnitude of $\frac{d\sigma}{d\Omega}$ increases with scattering angle and it is more prominent at high incident energy per nucleon of the projectile nucleus. Similar to total nuclear reaction cross section, elastic differential cross section also shows greater sensitiveness with increase of mass number of the target. Recently it has been reported by A. Marinov et al. [179], that the evidence of a superheavy isotope with $Z = 122$ or 124 and a mass number A=292; has been found in natural Th using inductively coupled plasma-sector field mass spectrometry. The estimated half-life of this isotope is $t_{1/2} \geq 10^8$ years. Thus the application of

the model to the recently discovered superheavy element Z=122 or 124 is interesting because of the possibility of the formation of the highly neutron-rich superheavy element in earth crust.

In **Chapter 5**, we have calculated the one nucleon removal reaction cross section (σ_{-1n}) for a few stable and neutron-rich Boron and Carbon halo nuclei with ^{12}C as target, using relativistic mean field (RMF) densities, in the frame work of Glauber model. The results are compared with the experimental data. Study of the stable nuclei with the deformed densities have shown a good agreement with the data. However, it differs significantly for the halo nuclei. We observe that while estimating the σ_{-1n} value from the difference of reaction cross sections of two neighboring nuclei with mass number A and that of A-1 in an isotopic chain, we get good agreement with the known experimental data for the halo cases. Thus the Glauber model fails for halo systems and deformation effect for one neutron removal cross section is important unlike the total reaction cross section σ_r.

In **Chapter 6**, we extend the idea of the preceding chapter and discuss the possibility of existence of superheavy nuclei. We also estimated the reaction and fusion cross section of various combination of light and heavy isotopes. We extended the calculations to exotic systems taking into consideration the possibility of availing the rn-process and the exotic nuclei capture processes in astrophysical objects. The enhanced cross sections with increase of mass number for both the projectile and target made it possible for the formation of the heavier neutron-rich nuclei way beyond the normal drip-lines predicted by the mass models. By the neutron or heavy ion (light neutron-rich nuclei) capture process the daughter nucleus becomes a superheavy element which may be available somewhere in the Universe in super-natural condition and can be possible to be synthesized in laboratories. Here the stability of the neutron-rich SHE or super-SHE against spontaneous fission arises due to widening of the fission barrier because of the excess number of neutrons.

The demonstration of a path for the formation of $^{408}X_{132}$ (A=408, Z=132, N=276) through complete fusion process is given by ^{20}B+^{208}Pb $\rightarrow$ ^{228}Fr, ^{20}B+^{228}Fr $\rightarrow$ ^{248}U, ^{20}B+^{248}U $\rightarrow$ ^{268}Bk, ^{20}B+^{268}Bk $\rightarrow$ ^{288}No, ^{20}B+^{288}No $\rightarrow$ ^{308}Bh, ^{20}B+^{308}Bh $\rightarrow$ $^{328}X_{112}$, ^{20}B+$^{328}X_{112}$ $\rightarrow$ $^{348}X_{117}$, ^{20}B+$^{348}X_{117}$ $\rightarrow$ $^{368}X_{122}$, ^{20}B+$^{368}X_{122}$ $\rightarrow$ $^{388}X_{127}$, ^{20}B+$^{388}X_{127}$ $\rightarrow$ $^{408}X_{132}$ and so on.

We have also studied the structural properties of the recently predicted thermally fissile neutron-rich $^{244-262}$Th and $^{246-264}$U nuclei in the frame-work of RMF model. The results are compared with the most popular FRDM calculations and found remarkably closure with its predictions. The obtained RMF densities are used to estimate the σ_r taking these fissile isotopes as target with ^{6,11}Li and ^{16,24}O as projectile. This results may be useful for experimentalists for the synthesis of neutron-rich thermally fissile Thorium and Uranium for the energy generation in future. The anatomy of the fission process is done with the help of the neck configurations. The maximum number of multifragmentation neutron at the time of fission is found to be more with larger neutron-rich nuclei. The excess neutrons are responsible to produce extra neutron fragments at the time of scission and emits few additional prompt neutrons along with the normal fission neutron (similar to the 2.5 neutrons of ^{235}U). The extra neutrons prompt the chain reaction which are vulnerable to thermal neutron fission and produce much more energy compared to ^{233,235}U or ^{239}Pu. This will certainly increase the efficiency of the chain reaction during the fission process and will reduce the critical mass of the nuclear fuel, if neutron-rich thermally fissile nuclei will be used as nuclear fuel in an accelerator based nuclear reactor.

In concluding this thesis we would like to say that, the main aim behind the present work has been to see how far the density dependent RMF interaction can account the diverse properties of nuclei in normal as well as exotic situations. The reasons behind the choice of the RMF theory for the study of nuclear properties are manifold. One of the important reasons, is the simplicity of the involved calculations

with this interaction. This RMF calculations become feasible for both light and superheavy nuclei. It has been possible to describe successfully many diverse quantities like binding energy, charge radius, rms radius, quadrupole deformation parameter, single particle energy spectra, total reaction cross section, differential scattering cross section, nucleon removal cross section and other related properties with a common set of parameters like NL-SH, NL3, NL3* and G2.

7.1 Future Prospects

The studies of nuclei far from the valley of stability offer new opportunities for research in the area of both nuclear structure and reaction physics, atomic physics as well as in astrophysics and material science. In nuclear physics there are a number of exciting topics to be addressed. Some of the topics which I am intending to pursue in immediate future are as follow: (i) The nuclear structure near the drip-line is one of the important research area in present day nuclear physics. A lot of exotic phenomena like halo and skin structure exhibit due to the large isospin in such nuclei. A detail analysis is needed within the availability of nuclear models taking into account the necessity of the problem. This can also be extended to superheavy nuclei, which is again an important area. The formation of SHE is very much interesting and needed immediate attention. (ii) Having a better understanding of the structure of nuclei, the improved results can be used to calculate the σ_r, $\frac{d\sigma}{d\Omega}$ and σ_{-1n} which we have done in the present thesis. (iii) In the present thesis, we have converted the deformed densities to spherical equivalent using two Gaussian fitting. This conversion may not be sufficient in may of the cases. Thus the fitting procedure have to be improved by extending the number of Gaussian. (iv) It is also very much in our mind to use the SHF or RMF deformed density directly in the calculations instead of converting it to its spherical equivalent. For this we have to modify the computer code accordingly.

Bibliography

[1] E. Rutherford, *Phil. Mag.* **24**, 669 (1911).

[2] J. Chadwick, *Nature*, **192**, 312 (1932).

[3] H. Yukawa, *Proc. Phys.-Math. Soc. Jpn.*, **17**, 48 (1935).

[4] M. G. Mayer, *Phys. Rev. C* **74**, 235 (1948).

[5] J. Dobaczewski, H. Flocard and J. Treiner, *Nucl. Phys. A* **422**, 103 (1984).

[6] P. Möller and J. R. Nix, *At. Data Nucl. Data Tables* **39**, 213 (1988).

[7] A. C. Muller and B. M. Sherrill, *Annu. Rev. Part. Sci.* **43**, 529 (1993).

[8] *Contemporary Physics Education Project (CPEP)*, Chap. **7** (2003).

[9] R. Bass, *Nuclear Reaction with Heavy Ion: Texts and Monographs in Physics* (Springer-Verlag, Berlin) (1980).

[10] R. J. Glauber, *Lectures on Theoretical Physics*, edited: W. E. Brittin and L. C. Dunham (Interscience, New York), **Vol. 1**, p.315 (1959).

[11] Oppenheimer and Phillips, *Phys. Rev.* **48**, 500 (1935).

[12] P. Egelhof et. al, *SIS/ESR experimental program*, GSI, Darmstadt (1988).

[13] G. D. Alkhazov et. al, *SIS/ESR experimental program*, GSI, Darmstadt (1991).

[14] G. D. Alkhazov, S. L. Belostotsky, A. A. Vorobyov, *Phys. Reports* **42c**, 89 (1978).

[15] N. D. Cook, *Models of the Atomic Nucleus*, Chap. 10 (2006).

[16] L. Satpathy, S. K. Patra and R. K. Choudhury, *PRAMANA - J. Phys.* **70**, 87 (2008).

[17] S. K. Patra, R. K. Choudhury and L. Satpathy, *J. Phys. G* **37**, 085103 (2010).

[18] M. Beckerman, *Phys. Rep.* **129**, 145 (1985).

[19] N. Bohr and F. Kalckar, *Dan. Mat. Fys. Medd.* **14**, No. 10 (1937).

[20] O. Haxel, J. H. D. Jensen and H. E. Suess, *Phys. Rev.* **75**, 1766 (1949).

[21] R. D. Woods, D. S. Saxon, *Phys. Rev.* **95**, 577 (1954).

[22] S. G. Nilsson, *Dan. Mat. Fys. Medd.* **29**, No. 16 (1955).

[23] A. Bohr and B. R. Mottelson, *Dan. Mat. Fys. Medd.* **27**, No. 16 (1953).

[24] L. S. Kisslinger, and R. A. Sorensen, *Rev. Mod. Phys.* **35**, 853 (1963).

[25] D. Vautherin and D. M. Brink, *Phys. Rev. C* **5**, 626 (1972).

[26] M. Beiner, H. Flocard, Nguyen Van Giai and P. Quentin, *Nucl. Phys. A* **238**, 29 (1975).

[27] H. Krivine, J. Treiner and O. Bohigas, *Nucl. Phys. A* **336**, 155 (1980).

[28] L. D. Miller, A. E. S. Green, *Phys. Rev. C* **5** 241 (1972).

[29] J. D. Walecka, *Ann. of Phys.* **83**, 491 (1974).

[30] J. Boguta, A. R. Bodmer, *Nucl. Phys. A* **292**, 413 (1977).

[31] J. Bartel, P. Quentin, M. Brack, C. Guet, H.-B. Hakansson, *Nucl. Phys. A* **386**, 79 (1982).

[32] R. Machliedt, *Advances in Nuclear Physics*, edited by J. W. Negele and E. Vogt (Plenum Press, New York), **Vol. 19**, 189 (1989).

[33] F. Coester, S. Cohen, B. D. Day, and C. M. Vincent, *Phys. Rev. C* **1**, 769 (1970).

[34] M. H. Johnson and E. Teller, *Phys. Rev.* **98**, 783 (1955).

[35] H. P. Dürr and E. Teller, *Phys. Rev.* **101**, 494 (1956).

[36] B. D. Serot and J. D. Walecka, The Relativistic Nuclear Many–Body Problem, *Advances in Nucl. Phys.*, J. W. Negele and Erich Vogt eds., **Vol. 16**, Plenum Press, NY (1986).

[37] R. Brockmann, *Phys. Rev. C* **18**, 1510 (1978).

[38] R. Brockmann and W. Weise, *Nucl. Phys. A* **355**, 365 (1981).

[39] K. Kratz, J. Bitouzet, F. Thelemann, P. Moller, and B. Pfeifer, *Astrophys. J.* **403**, 216 (1993).

[40] B. Chen, J. Dobaczewski, K. Kratz, K. Langake, B. Feifer, F. Thelemann, and P. Vogel, *Phys. Lett. B* **355**, 37 (1995).

[41] Y. K. Gambhir, P. Ring and A. Thimet, *Ann. Phys. (N.Y.)* **198**, 132 (1990).

[42] E. Wigner, *Phys. Rev.* **43**, 252 (1933).

[43] R. Machleidt, *Relativistic Dynamics and Quark-Nuclear Phys.*, Johnson and Picklesimer eds, p. 71 (1986).

[44] R. Machleidt, *Adv. Nucl. Phys.* **19**, 189 (1989).

[45] S. K. Patra, R. K. Gupta and W. Greiner, *Int. J. Mod. Phys. E* **6**, 641 (1997).

[46] P. K. Panda, S. K. Patra, J. Reinhardt, J. A. Maruhn, H. Stöcker and W. Greiner, *Int. J. Mod. Phys. E* **6**, 307 (1997).

[47] S. K. Patra and C. R. Praharaj, *Phys. Rev. C* **44**, 2552 (1991).

[48] M. Rufa, P. -G. Reinhard, W. Greiner and M. R. Stranger, *Phys. Rev. C* **38**, 390 (1988).

[49] P.-G. Reinhard, *Z. Phys. A* **329**, 257 (1993).

[50] M. M. Sharma, M. A. Nagrajan and P. Ring, *Phys. Lett. B* **312**, 377 (1993).

[51] C. J. Horowitz and B. D. Serot, *Nucl. Phys. A* **368**, 503 (1981).

[52] R. Brockmann and R. Machleidt, *Phys. Rev. C* **42**, 1965 (1990).

[53] H. F. Boersma and R. Machleidt, *Phys. Rev. C* **49**, 233 (1994).

[54] W. Mittig, P. Rousse-Chomaz and A. C. C. Villari, M *Europhysics News*, **35**, No 4. (2004).

[55] W. Nazarewicz, Nucl. Structure 98, *AIP Conference Proceedings* 481, Woodbury, New York, p. 381 (1998).

[56] M. V. Stoitsov, J. Dobaczewski, P. Ring, and S. Pittel, *Phys. Rev. C* **61**, 034311 (2000).

[57] J. Dobaczewski et al., *Phys. Rev. Lett.* **72**, 981 (1994).

[58] T. R. Werner, J. A. Sheikh, W. Nazarewicz, M. R. Strayer, A.S. Umar and M. Misu, *Phys. Lett. B* **335**, 259 (1994).

[59] W. -T Chou, R. F. Casten, N. V. Zamfir, *Phys. Rev. C* **51**, 2444 (1995).

[60] Z. Ren, Y. Zhu, Y. H. Cai and G. Xu, *Phys. Lett. B* **380**, 241 (1994).

[61] S. K. Patra, R. K. Gupta and W. Greiner, *Mod. Phys. Lett. A* **12**, 1727 (1997).

[62] R. K. Gupta, G. Münzenberg and W. Greiner, *J. Phys. G: Nucl. Part. Phys.* **23**, L13 (1997).

[63] D. Guillemaud-Mueller et al., *Nucl. Phys. A* **426**, 37 (1984).

[64] T. Motobayashi et al., *Phys. Lett. B* **346**, 9 (1995).

[65] T. Glasmacher et al., *Phys. Lett. B* **395**, 163 (1997).

[66] A. Ozawa, T. Kobayashi, T. Suzuki, K. Yoshida and I. Tanihata, *Phys. Rev. Lett.* **84**, 5493 (2000).

[67] R. K. Gupta, S. Kumar, M. Balasubramaniam, G. Münzenberg and W. Scheid, *J. Phys. G: Nucl. Part. Phys.* **28**, 699 (2002).

[68] I. Tanihata et al., *Phys. Rev. Lett.* **55**, 2676 (1985).

[69] I. Tanihata et al., Phys. Lett. B **206**, 592 (1988).

[70] T. Kobayashi, et al., *Phys. Rev. Lett.* **60**, 2599 (1988).

[71] S. K. Patra and C. R. Praharaj, *Europhys. Lett.* **20**, 87 (1992).

[72] I. Tanihata, et al., *Phys. Lett. B* **289**, 261 (1992).

[73] R. Morlock, et al., *Phys. Rev. Lett.* **79**, 3837 (1997).

[74] V. M. Strutinsky, *Nucl. Phys. A* **95**, 420 (1967); **122**, 1 (1968).

[75] W. D. Myers and W. J. Swiatecki, Nucl. Phys. **81**, 1 (1966).

[76] A. Sobiczewski, F. A. Gareev and B. N. Kalinkin, Phys. Lett. **22**, 500 (1966).

[77] S. G. Nilsson, J. R. Nix, A. Sobiczewski, Z. Szymanski, S. Wycech, C. Gustafson, and P. Möller, *Nucl. Phys. A* **115**, 545 (1968).

[78] U. Mosel and W. Greiner, Z. Phys. **222**, 261 (1969).

[79] E. O. Fizet and J. R. Nix, *Nucl. Phys. A* **193**, 647 (1972).

[80] P. Möller, J. R. Nix, W. D. Myers and W. J. Swiatecki, *At. Data Nucl. Data Tables* **59**, 185 (1995).

[81] P. Möller, J. R. Nix and K. -L. Kratz, *At. Data Nucl. Data Tables* **66**, 131 (1997).

[82] Yu. Ts. Oganessian et al., *Nature (London)* **400**, 242 (1999).

[83] Yu. Ts. Oganessian et al., *Phys. Rev. Lett.* **83**, 3154 (1999).

[84] S. K. Patra, C. -L. Wu, C. R. Praharaj and R. K. Gupta, *Nucl. Phys. A* **651**, 117 (1999).

[85] K. Rutz, M. Bender, T. Bürvenich, T. Schilling, P. -G. Reinhard, J. A. Maruhn and W. Greiner, *Phys. Rev. C* **56**, 238 (1997).

[86] A. T. Kruppa, M. Bender, W. Nazarewicz, P. -G. Reinhard, T. Vertse and S. Cwiok, *Phys. Rev. C* **61**, 034313 (2000).

[87] S. Cwiok, W. Nazarewicz and P. H. Heenen, *Phys. Rev. Lett.* **83**, 1108 (1999).

[88] S. Cwiok, J. Dobaczewski, P. -H. Heenen, P. Magierski and W. Nazarewicz, *Nucl. Phys. A* **611**, 211 (1996).

[89] R. K. Gupta, S. K. Patra and W. Greiner, *Mod. Phys. Lett. A* **12**, 1317 (1997).

[90] S. Yoshida, S. K. Patra, N. Takigawa, and C. R. Praharaj, *Phys. Rev. C* **50**, 1398 (1994).

[91] K. Sumiyoshi, *Nucl. Phys. A* **721**, 1036c (2003).

[92] R. Baruah, K. Duorah and H. L. Duorah, *J. Astrophys. Astro.* **30**, 165 (2009).

[93] W. H. Dickhoff, H. Müther, *Rep. Prog. Phys.* **55**, 1947 (1992).

[94] M. Brack, J. Damgard, A. S. Jensen, H. C. Pauli, V. M. Strutinsky and C. Y. Wong, *Rev. Mod. Phys.* **44**, 320 (1972).

[95] E. Chabanat, P. Bonche, P. Hansel, J. Meyer, and R. Schaeffer, *Nucl. Phys. A* **627**, 710 (1997).

[96] J. R. Stone and P. -G. Reinhard, *Prog. Part. Nucl. Phys.* **58**, 587 (2007).

[97] J. R. Stone, J. C. Miller, R. Koncewicz, P.D. Stevenson, and M. R. Strayer, *Phys. Rev. C* **68**, 034324 (2003).

[98] P. -G. Reinhard, *Ann. Phys. (Leipzig)* **1**, 632 (1992).

[99] P. -G. Reinhard and H. Flocard, *Nucl. Phys. A* **584**, 467 (1995).

[100] E. Chabanat, P. Bonche, P. Haensel, J. Meyer, and R. Schaeffer, *Nucl. Phys. A* **635**, 231 (1998).

[101] B. A. Brown, *Phys. Rev. C* **58**, 220 (1998).

[102] L. I. Schiff, *Phys. Rev.* **84**, 10 (1951).

[103] R. J. Rurnstahl, C. E. Price and G. E. Walker, *Phys. Rev. C* **36**, 2590 (1987).

[104] R. J. Rurnstahl and C. E. Price, *Phys. Rev. C* **40**, 1398 (1989).

[105] P. Ring, *Prog. Part. Nucl. Phys.* **37**, 193 (1996).

[106] P. -G. Reinhard, *Rep. Prog. Phys.* **52**, 439 (1989).

[107] Y. Sugahara and H. Toki, *Nucl. Phys. A* **579**, 557 (1994).

[108] R. J. Furnstahl, B. D. Serot, and H. B. Tang, *Nucl. Phys. A* **598**, 539 (1996).

[109] R. J. Furnstahl, H. B. Tang, and B. D. Serot, *Phys. Rev. C* **52**, 1368 (1995).

[110] A. R. Bodmer, *Nucl. Phys. A* **526**, 703 (1991).

[111] C. J. Horowitz and B. D. Serot, *Nucl. Phys. A* **368**, 503, (1981).

[112] A. G. Lalazissis, J. König and P. Ring, *Phys. Rev. C* **55**, 540 (1997).

[113] R. J. Furnstahl, B. D. Serot, and H. B. Tang, *Nucl. Phys. A* **615**, 441 (1997).

[114] R. J. Furnstahl, and B. D. Serot, *Nucl. Phys. A* **671**, 447 (2000).

[115] B. D. Serot and J. D. Walecka, *Int. J. Mod. Phys. E* **6**, 515 (1997).

[116] B. ter Haar and R. Malfliet, *Phys. Rep.* **149**, 207 (1987).

[117] A. Bohr and B. R. Mottelson, *Nuclear Structure*, **Vol. I**, W. A. Benjamin, New York, **Vol. 1**, Chap. 2 (1969).

[118] P. Ring, P. Schuck, *The Nuclear Many-Body Problem* (Springer-Verlag, New York) (1980).

[119] J. M. Eisenberg and W. Greiner, *Microscopic Theory of the Nucleus* (North Holland, Amserdam) (1972).

[120] E. Chabanat, P. Bonche, P. Haensel, J. Meyer and R. Schaeffer, *Nucl. phys. A* **635**, 231 (1998).

[121] N. Sandulescu, N. V. Giai and R. J. Liotta, *Phys. Rev. C* **61**, 061301(R) (2000).

[122] M. Del Estal, M. Centelles, X. Viñas, and S. K. Patra, *Phys. Rev. C* **63**, 024314 (2001).

[123] M. Del Estal, M. Centelles, X. Viñas, and S. K. Patra, *Phys. Rev. C* **63**, 044321 (2001).

[124] D. G. Madland and J. R. Nix, *Nucl. Phys. A* **476**, 1 (1988).

[125] S. K. Patra, M. Del Etal, M. Centelles, and X. Vinas, *Phy. Rev. C* **63**, 024311 (2001).

[126] T. R. Werner, J. A. Sheikh, W. Nazarewicz, M. R. Strayer, A. S. Umar, and M. Mish, *Phys. Lett. B* **335**, 259 (1994).

[127] G. A. Lalazissis, D. Vretenar, P. Ring, M. Stoitsov and L. M. Robledo, *Phys. Rev. C* **60**, 014310 (1999).

[128] F. Tondeur, S. Goriely, J. M. Pearson, and M. Onsi, *Phys. Rev. C* **62**, 024308 (2000).

[129] U. Hofmann and P. Ring, *Phys. Lett. B* **214**, 307 (1988).

[130] G. A. Lalzissis, D. Vretenar, and P. Ring, *Nucl. Phys. A* **650**, 133 (1999).

[131] M. L. Miller, K. Reygers, S. J. Sanders and P. Steinberg, *Annu. Rev. of Nucl. and Part. Sci.* **57**, 205 (2007).

[132] Hussein M. A. Ahmed and E. H. Esmael, *Int. J. Mod. Phys. E* **12**, 845 (2003).

[133] B. Abu-Ibrahim, Y. Ogawa, Y. Suzuki and I. Tanihata, *Comp. Phys. Comm.* **151**, 369 (2003).

[134] P. J. Karol, *Phys. Rev. C* **11**, 1203 (1975).

[135] J. Chauvin, D. Lubrun, A. Lounis and M. Buenerd, *Phys. Rev. C* **28**, 1970 (1983).

[136] M. Buenerd, A. Lounis, J. Chauvin, D. Lebrun, P. Martin, G. Duhamel, J. C. Gondrand and P. D. Saintignon, *Nucl. Phys. A* **424**, 313 (1984).

[137] P. Shukla, *Phys. Rev. C* **67**, 054607 (2003).

[138] A. Bhagwat and Y. K. Gambhir, *Phys. Rev. C* **77**, 027602 (2008); **73**, 054601 (2006); **73**, 024604 (2006); **69**, 014315 (2004); **68**, 044301 (2003).

[139] S. K. Charagi and S. K. Gupta, *Phys. Rev. C* **41**, 1610 (1990).

[140] S. K. Charagi and S. K. Gupta, *Phys. Rev. C* **46**, 1982 (1992).

[141] S. K. Charagi, *Phys. Rev. C* **48**, 452 (1993).

[142] S. K. Charagi and S. K. Gupta, *Phys. Rev. C* **56**, 1171 (1997).

[143] M. S. Hussein, R. A. Rego and C. A. Bertulani, *Phys. Rep.* **201**, 279 (1991).

[144] K. Hagino, N. Rowley and A.T. Kruppa, *Comp. Phys. Comm.* **123**, 143 (1999).

[145] K. Hagino, N. Takigawa, A. B. Balantekin and J. R. Bennett, *Phys. Rev. C* **52**, 286 (1995).

[146] S. Landowne and S. C. Pieper, *Phys. Rev. C* **29**, 1352 (1984).

[147] I. Tanihata, *J. Phys. G* **22**, 157 (1996).

[148] P. G. Hansen and B. Jonson, *Europhys. Lett.* **4**, 409 (1989).

[149] P. Arumugam, B. K. Sharma, P. K. Sahu, S. K. Patra, T. Sil, M. Centelles, and X. Viñas, *Phys. Lett. B* **601**, 51 (2004).

[150] C. Chandler, et al., *Phys. Rev. C* **61**, 044309 (2000).

[151] D. Gogny, in *"Proceedings, Int. Conf. on Nuclear selfconsistent Fields, Trieste, 1975"* (G. Ripka and M. Porneuf,eds.), North-Holland, Amsterdam (1975).

[152] J. P. Blaizot, *Phys. Rep.* **64**, 171 (1980).

[153] R. Kumar, et al., *Phys. Rev. C* **76**, 034301 (2007).

[154] D. Rudolph, et al., *Phys. Rev. Lett.* **82**, 3763 (1999).

[155] T. Mizusak, T. Otsuka, M. Honma, and B. A. Brown, *Phys. Rev. C* **63**, 044306 (2001).

[156] D. Rudolph, et al., *Eur. Phys. J. A* **36**, 131 (2008).

[157] S. K. Patra, F. H. Bhat, R. N. Panda, P. Arumugam, and Raj. K. Gupta, *Phys. Rev. C* **79**, 044303 (2009).

[158] P. Arumugam, B. K. Sharma, S.K. Patra, and R.K. Gupta, *Phys. Rev. C* **71**, 064308 (2005).

[159] S. K. Patra, C. -L. Wu, C. R. Praharaj, and R. K. Gupta, *Nucl. Phys. A* **651**, 117 (1999).

[160] S. K. Patra, R. K. Gupta, B. K. Sharma, P. D. Stevenson, and W. Greiner, *J. Phys. G* **34**, 2073 (2007).

[161] L. Ray, G. W. Hoffmann, M. Barlett, J. McGill, J. Amann, G. Adams, G. Pauletta, M. Gazzaly and G. S. Blanpied, *Phys. Rev. C* **23**, 828 (1981).

[162] I. Sick, J. B. Bellicard, J. M. Cavedon, B. Frous, M. Heut, P. Leconte, P. X. Ho and S. Platchkov, *Phy. Lett. B* **88**, 245 (1979).

[163] L. Ray, *Phys. Rev. C* **19**, 1855 (1979).

[164] G. A. Lalazisis and S. E. Massen, *Phys. Rev. C* **55**, 2427 (1997).

[165] J. W. Negele and D. Vautherin, *Phys. Rev. C* **5**, 1472 (1972).

[166] G. Audi, A. H. Wapstra, and C. Thibault, *Nucl. Phys. A* **729**, 337 (2003).

[167] G. Audi and Meng Wang, *Private communication*, April (2011).

[168] W. Nortershauser, T. Neff, R. Sanchez and I. Sick, *Phys. Rev. C* **84**, 024307 (2011).

[169] I. Angeli, *At. Data Nucl. Data Tables* **87**, 185 (2004).

[170] H. Flocard, P. Quentin, and D. Vautherin, *Phys. Lett. B* **46**, 304 (1973).

[171] W. Koepf and P. Ring, *Phys. Lett. B* **212**, 397 (1988).

[172] J. Fink, V. Blum, P. -G. Reinhard, J. A. Maruhn, and W. Greiner, *Phys. Lett. B* **218**, 277 (1989).

[173] D. Hirata, H. Toki, I. Tanihata, and P. Ring, *Phys. Lett. B* **314**, 168 (1993).

[174] A. Poves, J. Sanchez-Solano, E. Caurier, and F. Nowacki, *Nucl. Phys. A* **694**, 157 (2001).

[175] E. Caurier, G. Martinez-Pinedo, F. Nowacki, A. Poves, and A. P. Zuker, *Rev. Mod. Phys.* **77**, 427 (2005).

[176] S. K. Patra, *Int. J. Mod. Phys. E* **2**, 471 (1993).

[177] A. Ozawa, T. Suzuki, and I. Tanihata, *Nucl. Phys. A* **693**, 32 (2001).

[178] R. N. Panda and S. K. Patra, *J. Mod. Phys.* **Vol. 1**, 312 (2010).

[179] A. Marinov, I. Rodushkin, D. Kolb, A. Pape, Y. Kashiv, R. Brandt, R. V. Gentry, and H. W. Miller, *Int. J. Mod. Phys. E* **19**, 131 (2010).

[180] S. Kox et al., *Phys. Rev. C* **35**, 1678 (1987).

[181] H. P. Wellisch and D. Axen, *Phys. Rev. C* **54**, 1329 (1996).

[182] Chun-Tian Liang, Yan-An Luo, Xiao-Hua Li and Chong-Hai Cai, *J. Phys. G: Nucl. Part. Phys.* **36**, 015102 (2009).

[183] L. Sihver et al., *Phys. Rev. C* **47**, 1225 (1993).

[184] A. Shukla, B. K. Sharma, R. Chandra, P. Arumugam, and S. K. Patra, *Phys. Rev. C* **76**, 034601 (2007).

[185] B. K. Sharma, S. K. Patra, R. K. Gupta, A. Shukla, P. Arumugam, P. D. Stevenson, and W. Greiner, *J. Phys. G* **32**, 2089 (2006).

[186] P. Möller et al., *Phys. Rev. Lett.* **99**, 252501 (2007).

[187] G. Ewald et al., *Phys. Rev. Lett.* **93**, 113002 (2004).

[188] R. Sanchez et al., *Phys. Rev. Lett.* **96**, 033002 (2006).

[189] C. W. De Jager, H. De Vries, and C. De Vries, *At. Data and Nucl. Data Tables* **14**, 479 (1974).

[190] Y. Ogawa, K. Yabana, and Y. Suzuki, *Nucl. Phys. A* **543**, 722 (1992).

[191] Y. Ogawa, K. Yabana, and Y. Suzuki, *Phys. Rev. C* **64**, 057306 (2001).

[192] M. Y. H. Farag, *Eur. Phys. J. A* **12**, 405 (2001).

[193] O. V. Bochkarev et al., *Eur. Phys. J. A* **1**, 15 (1998).

[194] Yu. Ts. Oganessian et al., *Phys. Rev. C* **74**, 044602 (2006).

[195] Yu. Ts. Oganessian et al., *Phys. Rev. C* **76**, 011601 (2007).

[196] Yu. Ts. Oganessian et al., *Phys. Rev. C* **79**, 024603 (2009).

[197] Yu. Ts. Oganessian et al., *Phys. Rev. C* **79**, 024608 (2009).

[198] See, e.g., http://www.nature.com/nindia/2008/080520/full/nindia.2008.204.html, as highlited by Nature India, 20 May (2008).

[199] H. L. Bradt and B. Peters, *Phys. Rev.* **77**, 54 (1950).

[200] S. Barshay, C.B. Dover and J. P. Vary, *Phys. Lett. B* **51**, 5 (1974).

[201] S. Barshay, C. B. Dover and J. P. Vary, *Phys. Rev. C* **11**, 360 (1975).

[202] A. Ingemarsson and M. Lantz, *Phys. Rev. C* **61**, 064605 (2003).

[203] A. Ingemarsson and M. Lantz, *Phys. Rev. C* **72**, 064615 (2005).

[204] J. Y. Hostachy et al, *Nucl. Phys. A* **490**, 441 (1988).

[205] V. Bernard et al, *Nucl. Phys. A* **423**, 511 (1984).

[206] P. A. Mazzali, J. Deng, K. Nomoto, D. N. Sauer, E. Pian, N. Tominaga, M. Tanaka, K. Maeda and A. V. Filippenko, *Nature* **442**, 1018 (2006).

[207] T. A. Thompson, P. Chang and E. Quataert, *Astrophys. Jour.* **611**, 380 (2004).

[208] P. O. Lagage and C. J. Cesarsky, *Astron. Astrophys.* **125**, 249 (1983).

[209] B. Bonin, *J. Physique* **48**, 1479 (1987).

[210] S. G. Nilsson, C. F. Tsang, A. Sobiczewski, Z. Szymanski, S. Wycech, C. Gustafson, I. -L. Lamm, P. Mö11er, and B. Nilsson, *Nucl. Phys. A* **131**, 1 (1969).

[211] M. Brack, J. Damgaaid, A. S. Jensen, H. C. Pauli, V. M. Strutinsky, and C. Y. Wong, *Rev. Mod. Phys.* **44**, 185 (1972).

[212] E. O. Fiset and J. R. Nix, *Nucl. Phys. A* **193**, 647 (1972).

[213] J. R. Nix, *Ann. Rev. Nucl. Sci.* **22**, 65 (1972).

[214] A. Shukla, B. K. Sharma, R. Chandra, P. Arumugam and S. K. Patra, *Phys. Rev. C* **76**, 034601 (2007).

[215] S. K. Patra, R. N. Panda, P. Arumugam and Raj K. Gupta, *Phys. Rev. C* **80**, 064602 (2009).

[216] E. C. Simpson and J. A. Tostevin, *Phys. Rev. C* **79**, 024616 (2009).

[217] T. Misu, W. Nazarewicz and S. Aberg, *Nucl. Phys. A* **614**, 44 (1997).

[218] F. M. Nunes, *Nucl. Phys. A* **757**, 349 (2005).

[219] Shan-Gui Zhou, J. Meng, P. Ring and En-Guang Zhao, *Phys. Rev. C* **82**, 011301R (2010).

[220] B. D. Serot and J. D. Walecka, *Adv. Nucl. Phys.* **16**, 1 (1986).

[221] D. Cortina-Gil D et al., *Eur. Phys. J. A* **10**, 49 (2001).

[222] E. Sauvan et al., *Phys. Rev. C* **69**, 044603 (2004).

[223] E. Sauvan et al., *Phys. Lett. B* **1**, 491 (2000).

[224] Wu Cuie et al., *J. Phys. G* **31**, 47 (2005).

[225] D. L. Olson et al., *Phys. Rev. C* **28**, 1602 (1983).

[226] J. Meng, S. -G. Zhou and I. Tanihata, *Phys. Lett. B* **532**, 209 (2002).

[227] D. Bazin et al., *Phys. Rev. C* **57**, 2156 (1998).

[228] V. Devanathan, Nuclear Physics, Chap. 13, Page 298 Narosa (2011).

[229] P. Möller and J. R. Nix, *Nucl. Phys. A* **549**, 84 (1992).

[230] *Nuclear Power and Sustainable Development*, IAEA, April (2006).

[231] *DAE-2004 and Planning Commission-2006*, Govt. of India.

[232] http://www.ans.org/resourses/dosechart/.

[233] J. N. De, X. Viñas, S. K. Patra, and M. Centelles, *Phys. Rev. C* **64**, 057306 (2001).

[234] V. Friese, and C. Sturm CBM Progress report ISBN 978-3-9811298-8-5 2010 (www.gsi.de); www.fair-center.eu.

[235] J. R. Wilson and R. W. Mayle, *Phys. Rep.* **227**, 97 (1993).

[236] B. S. Meyer, *Annu. Rev. Astron. Astrophys.* **32**, 153 (1994).

[237] J. M. Pearson *Nuclear Physics: Energy and Matter*, Ch. II, Adam Hilger Ltd, p. 87 (1986).

[238] T. Dubler et al., *Nucl. Phys. A* **219**, 29 (1974).